A Study of Catalytic Pt Nanoparticles inside a Nano-porous Functionalized UiO MOF-matrix for CO_2-Hydrogenation

Bjørn Gading Solemsli

Thesis for the degree of
Master of Science

Department of chemistry
The Faculty of Mathematics and Natural Sciences

UNIVERSITY OF OSLO

June 2020

2020

A Study on Catalytic Pt Nanoparticles inside a Nano-porous Functionalized UiO MOF-matrix for CO_2-Hydrogenation

Bjørn Gading Solemsli

http://www.duo.uio.no/

Print: Reprosentralen, Universitetet i Oslo

Abstract

Hydrogenation of carbon dioxide has received increasing attention in catalytic research the last decade as a sustainable alternative for producing high value chemicals that today are produced from fossil fuels. The aim of this thesis has been two-fold: First, to study Pt nanoparticles formed in various UiO-66 and -67 metal-organic frameworks (MOFs) by Transmission Electron Microscopy (TEM), and second, to study the Pt-containing MOFs as catalysts for the CO_2 hydrogenation reaction.

Three Zr-based UiO-66 MOF and nine UiO-67 MOF samples containing different amounts of functionalized linkers were impregnated with different amounts of K_2PtCl_4 and reduced in H_2 at 350 °C for 4 hours to form Pt nanoparticles embedded in the MOF matrix. The samples were then tested in a H_2/CO_2 feed at 8 bar and 170 °C for the hydrogenation reaction. After testing, TEM was used to investigate the formation of Pt nanoparticles and their relationship with the surrounding MOF structure.

The study revealed that, despite variable the linkers in the MOF, the conversion of CO_2 is dominated by the reverse water-gas shift reaction, suggesting that the linkers do not partake the reactions mechanisms. Analysis using TEM revealed that the Pt nanoparticles grow independently of its surroundings inside the MOFs with no observable growth relationship with the MOF. The nanoparticles are seen to grow into octahedral crystals that are larger than the pores in the framework. Samples with different amounts of missing linker type defects show that the presence of open Zr-node sites enhances the selectivity towards methanol.

A sample of Pt-functionalized UiO-67 with 10% [2,2'-bipyridine]5,5'-dicaboxylic acid linker was oxidised to induce missing linker defects post synthetically. After reduction in H_2 at 350 °C for 4 hours, the sample was oxidized *in situ* in synthetic air for three different time spans. Careful analysis with N_2-adsroption and TEM revealed that the structure of the MOF deteriorates and loses accessible surface area with increasing time on steam, while keeping the dispersion of the Pt nanoparticles. PXRD analysis revealed the formation of tetragonal ZrO_2. Extensive tests from 1-30 bar and 170-375 °C reveal a lower conversion and higher selectivity towards methanol for a fully calcined sample, indicating that the Zr-nodes behave similarly to non-MOF ZrO_2 supports. Transient kinetic studies of the parent UiO-67 sample revealed that the sample behaves similarly to previously studied systems by Gutterød *et al.*, and showed the presence of an inverse kinetic isotope effect for methane and methanol formation upon H_2/D_2 exchange.[1]

Over all, this study further confirms the role of the Pt nanoparticles and the role of the MOF for the CO_2 hydrogenation reaction and can contributes to the design of better catalytic systems for CO_2 hydrogenation.

Preface

This thesis finalizes the degree in Master of Science in Inorganic Chemistry and Material Chemistry, at the Department of Chemistry, University of Oslo. The experimental work has been done in the group of Catalysis and Structure Physics, at the Centre for Material Science and Nanotechnology (SMN) in the period from August 2018 to June 2020.

First, I would like to express my deepest gratitude to my supervisors, Professor Unni Olsbye, Associated Professor Anette Eleonora Gunnæs and Dr. Emil Sebastian Gutterød for their guidance and support. I am also thankful for the inspiring discussions and good times, social and scientific, during my visits to the University of Turin and Utrecht University.

Moreover, I would like to thank all the member of the Catalysis section and the Structure Physics section for interesting discussions and pleasant office environments. I would especially like to thank Evgeniy Redekop and Christopher William Affolter for their inspiration and help with burning MOFs and Phuong Dan Nguyen for helping with TEM.

Lastly, I would like to thank my parents for supporting and believing in me, and showing a great deal of interest all these years.

University of Oslo, June 2020

Bjørn Gading Solemsli

Table of contents

Molecules and abbreviations

Molecules

Biphenyl-4,4'-dicarboxylic acid

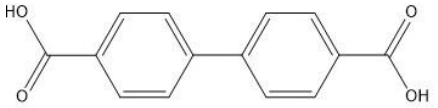

[1,1'-binaphthalene]-4,4'-dicaboxylic acid

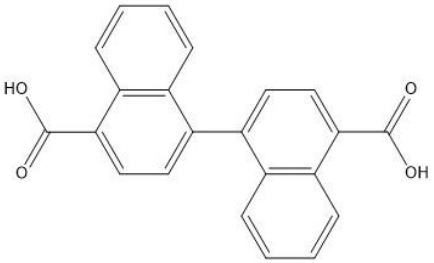

[2,2'-bipyridine]5,5'-dicaboxylic acid

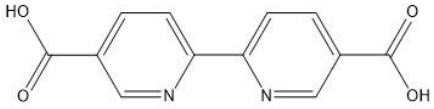

1,4-benzodicarboxylic acid

[3-X]1,4-benzodicarboxylic acid*

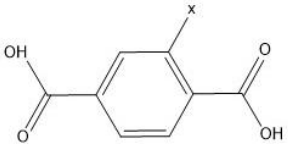

Dimethylformamide

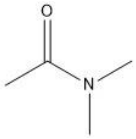

Acetone

Potassium tetrachloroplatinate(II)

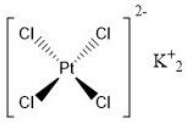

**where the X is either COOH or NH_2*

Abbreviations

ABF STEM	Annular bright-field scanning transmission electron microscopy
bcc	Body-centered cubic
BDC	1,4-benzodicarboxylic acid
BET	Burnauer-Emmet-Teller theory
BF STEM	Bright-field scanning transmission electron microscopy
bipy	[2,2'-bipyridine]5,5'-dicaboxylic acid
BN	[1,1'-binaphthalene]-4,4'-dicaboxylic acid
bpdc	Biphenyl-4,4'-dicarboxylic acid
CCD	Charged-coupled device
CCS	Carbon capture and storage
CCU	Carbon capture and usage
DF STEM	Dark-field scanning transmission electron microscopy
DMF	Dimethylformamide
EDS	Energy-dispersive X-ray spectroscopy
EELS	Electron energy loss spectroscopy
fcc	Face-centered cubic
FEG	Field-emission gun
FT-IR	Fourier-transform infrared spectroscopy
GC	Gas chromatograph
HAADF STEM	High-angle annular dark-field scanning transmission electron microscopy
hcp	Hexagonal closed packed
HR TEM	High resolution transmission electron microscopy
MeOH	Methanol, CH_3OH
MFC	Mass flow controller
MOF	Metal-organic framework
MS	Mass spectrometer
PXRD	Powder X-ray diffraction
QMS	Quadrupole mass spectrometer
RWGS	Reverse water-gas shift
SA	Selected area diffraction
SBU	Secondary building unit
SEM	Scanning electron microscope
SSITKA	Steady-state isotopic transient kinetic analysis

SSA	Specific surface area
STEM	Scanning transmission electron microscopy
TAP	Temporal analysis of products
TEM	Transmission electron microscopy
TGA	Thermogravimetric analysis
TOF	Turnover frequency
TON	Turnover number
UiO	University of Oslo (Universitetet i Oslo)
σ	Standard deviation

1 Introduction and background

1.1 CO_2 in today's society

As the world's population has grown throughout the last 100 years, the need for energy to sustain the population has grown in tandem. At the turn of the 20th century, about 99.9% of the energy sources used released carbon dioxide as a byproduct (***Figure 1.1***). The total energy produced was then 12 100 TWh. The fraction of CO_2-releasing fuels has decreased to 86.9% a hundred years later, but the total amount of energy produced has risen to 157 063 TWh.[2-10] These numbers have caused many scientists to be alarmed as the energy demand is only expected to increase, and the topic of "climate"-politics and policies have become a central item on the geopolitical agenda.

Although CO_2 release is mainly associated with energy production, a substantial fraction also comes from other parts of industry. One source is the production and usage of fuels. Traditionally, both diesel and gasoline are used as fuels for transport. They are mainly produced from refined crude oil and the production emit CO_2 as a byproduct.

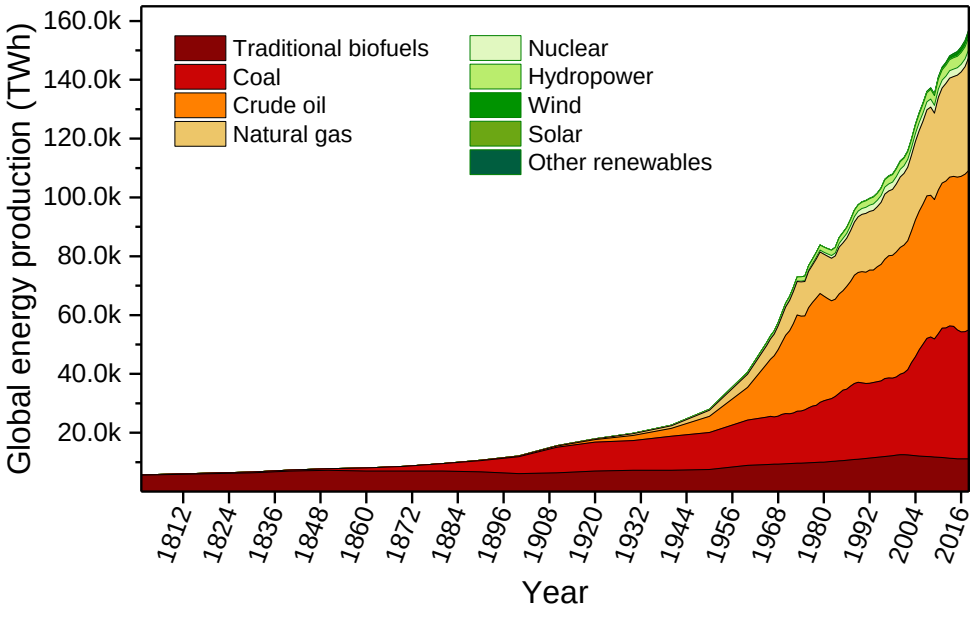

Figure 1.1: *A plot showing the global energy production from 1800 to 2018. Energy sources that directly produce CO_2 as a byproduct are all shades of red, and the ones that do not directly produce CO_2 are all shades of green. By the term "direct" is meant energy sources that produce CO_2 when being utilized for energy production, although some CO_2 were produced by making of the facilities etc. for all the sources listed above. Traditional biofuels are typically wood and biomass. Source: Energy Transitions: Global and National Perspectives. & BP Statistical Review of World Energy.*[2-10]

A suggestion for combating the ever-increasing production of CO_2 is by capturing the CO_2. This is very difficult due to the low concentration of the gas in the atmosphere. However new and modern technologies are making it increasingly feasible to collect CO_2 at source, and also directly from the air. The captured CO_2 can be stored (CCS) or utilized (CCU). [11]

The fuels produced from CCU can potentially be used as a way of storing energy for later use from less polluting energy sources, giving less reliable energy sources like wind and solar power, a way to meet demands independently of weather. This fuel could be considered a carbon neutral resource since no "new" carbon is being introduced to the cycle. CCS and CCU are only some of the solutions to combat the coming energy crisis the globe is facing, but together with other technologies, it will help towards a less polluted and more sustainable future.

1.2 CO_2 hydrogenation, RWGS, methanation and methanol formation

Hydrogenation is an addition reaction between hydrogen and other compounds/elements. In this thesis, reactions between carbon dioxide and hydrogen are studied to test the activity of several different catalytic systems. A combination of the reverse water gas shift reaction (RWGS), the carbon dioxide to methanol reaction and the methanation reaction takes place in the hydrogenation of carbon dioxide (see **Eq. 1.6-1.8**). As seen from the Frost-Ebsworth diagram (***Figure 1.2***) of the lower carbons depicted below, carbon dioxide is one of the more stable forms of carbon. Due to its stability, a high energy-density agent is needed in order to reduce it. Hydrogen, that can be produced through electrolysis using renewable energy, is a good candidate for an energetically favoured chemical reduction of carbon dioxide.[12] An activation energy barrier must still be overcome to initiate the reaction.

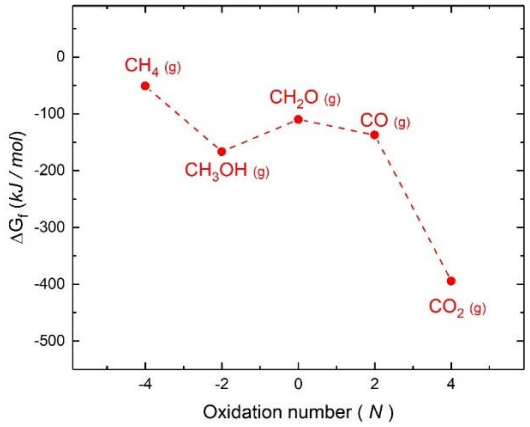

Figure 1.2: *A Frost-Ebsworth plot showing Gibbs free energy of formation as a function of the oxidation number for carbon. This figure only comprises species containing one carbon, often called "the lower carbons".*[13]

1.2.1 Methanol synthesis

Methanol was traditionally produced by distilling wood, but in the 1920s a new method was developed using a Zn/Cr_2O_3 catalyst.[14, 15] This catalyst used a water-gas mixture to produce methanol.[16] This reaction operates at high pressures and high temperatures, 300 bar and 300-400 °C, needed to overcome the energy barrier required to form methanol. Today, methanol is mainly synthesized from a gas mixture of hydrogen, carbon monoxide and carbon dioxide:

$$CO + 2H_2 \rightleftarrows CH_3OH \qquad \Delta H°_{298} = -91 \text{ kJ mol}^{-1} \qquad \textbf{(1.1)}$$

$$CO_2 + 3H_2 \rightleftarrows CH_3OH + H_2O \qquad \Delta H°_{298} = -49{,}5 \text{ kJ mol}^{-1} \qquad \textbf{(1.2)}$$

Some catalysts that are used today are $Cu/Zn/Al_2O_3$ and $Cu/ZnO/Al_2O_3$.[17] Methanol can also be synthesized directly from methane by reaction with O_2, but it has to compete with other, more exothermic reactions to carbon monoxide and carbon dioxide.[18]

1.2.2 Steam reforming

Methane is usually a natural resource by itself and is not synthesized. It is a natural gas that can be found in porous sediments in the ground. One of its uses is in the steam reforming reaction, where methane and water is used to produce hydrogen. Steam reforming was developed in Germany in the early nineteenth century to obtain hydrogen for ammonia synthesis.[19] The reforming process occurs with the following reactions along with the water-gas shift reaction (see below):

$$CH_4 + 2H_2O \rightleftarrows CO_2 + 4H_2 \qquad \Delta H°_{298} = 252{,}9 \text{ kJ mol}^{-1} \qquad \textbf{(1.3)}$$

$$C_nH_m + nH_2O \rightleftarrows nCO + \left(n + \frac{m}{2}\right) H_2 \qquad \Delta H°_{298} = -91 \text{ kJ mol}^{-1} \qquad \textbf{(1.4)}$$

1.2.3 Water-gas shift reaction

The water-gas shift reaction is used to modify the composition of the gas coming from the steam reforming process. It is done with the purpose to obtain a final product that contains less carbon monoxide and more hydrogen. This is important when the hydrogen is used for ammonia synthesis, since any CO- or oxygen-containing compounds poisons the catalyst used.[19]

$$CO + H_2O \rightleftarrows CO_2 + H_2 \qquad \Delta H°_{298} = -41 \text{ kJ mol}^{-1} \qquad \textbf{(1.5)}$$

1.2.4 The combined CO_2 Hydrogenation reaction

In the systems that are investigated in this thesis a possible combination of reactions take place (***Eq. 1.1-1.5***), although some of them are reversed. In the reaction, a mixture of carbon dioxide and hydrogen produces four main products: carbon monoxide, methane, methanol and water. There may be other reactions occurring, where longer chained hydrocarbons can be formed through polymerization. Methane and methanol may also be formed from carbon monoxide.

Reverse water-gas shift reaction

$$CO_2 + H_2 \rightleftarrows CO + H_2O \qquad \Delta H°_{298} = 41 \text{ kJ mol}^{-1} \qquad \textbf{(1.6)}$$

Methanol formation

$$CO_2 + 3H_2 \rightleftarrows CH_3OH + H_2O \qquad \Delta H°_{298} = -49{,}5 \text{ kJ mol}^{-1} \qquad \textbf{(1.7)}$$

CO_2 methanation

$$CO_2 + 4H_2 \rightleftarrows CH_4 + 2H_2O \qquad \Delta H°_{298} = -252{,}9 \text{ kJ mol}^{-1} \qquad \textbf{(1.8)}$$

Methanol is the only one of the lower carbon products that is liquid at room temperature, making it easy to separate from the rest. It can be separated with water by cooling the products and later distilling the methanol from water. Once separated, it can be used to make other, more complex chemicals, or be used as fuel. The rest of the products, mainly CO, CH_4 and CO_2, can be used in further reactions as well, but are harder to separate.

Research into catalytic systems for carbon dioxide hydrogenation is an increasingly hot topic.[20-23] Transition metals have been the main catalytic systems investigated, with Ru, Pd and Pt being the most stable for the methanation reaction.

1.3 Metal-organic frameworks and the UiO-series

Metal-organic frameworks (MOFs), a subgroup of coordination polymers, are synthetically engineered large organometallic ligands condensed into complex porous networks.[24] They are a field of research that has garnered tremendous interest since they appeared in late twentieth century as 2D networks, later being developed into 3D networks.[25] The frameworks started as a thought experiment among polymer chemists, but has become one of the forefronts in modern coordination chemistry and material science. MOFs are nanoporous structures that consist of

an organic component (the linker, linking the structure together) and an inorganic component (the Secondary Building Units (SBUs), binding the linkers together). By varying the type of cluster and linker that are used, the network can have different pore volumes and crystal structures. Due to their complex structures, the materials can have uses within the fields of gas storage and catalysis.[26]

1.3.1 UiO series and functionalized MOF.

The UiO (University of Oslo) MOF series has a 12-coordinated Zr cluster in a $Zr_6O_4(OH)_4$ configuration, acting as the Secondary Building Units (SBUs.) 1,4- (or 4,4'-) dicarboxylated phenyl (diphenyl, triphenyl) linkers interconnect these Zr-nodes, giving the structure a face-centred cubic structure. They were first published in 2008 when Cavka *et al.* reported a new type of MOF with exceptional stability.[27] The three main MOFs in this series are the UiO-66, UiO-67 and the UiO-68, with longer linkers from UiO-66 to UiO-68: Phenyl, biphenyl or triphenyl linkers, respectively) (***Figure 1.3 & 1.4***). In this work, the UiO-66 and the UiO-67 MOFs were investigated.

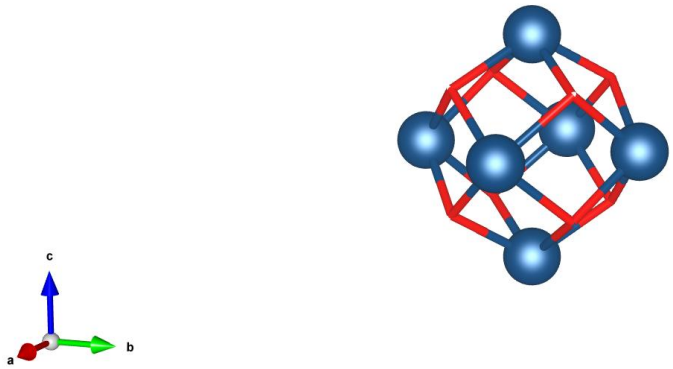

Figure 1.3: *Models of the $Zr_6O_4(OH)_4$ cluster. The linkers are connected to the twelve metal-carboxyl sites situated around the SBU. The blue spheres represent zirconium, the red lines represent oxygen. Hydrogens are not included in this model for better visualisation.*

The two types of pores that are present in the UiO MOFs are the tetrahedral cage and the octahedral cage. For the UiO-66 the tetrahedral cage is 8 Å and the octahedral cage is 11 Å in diameter, compared to the UiO-67 which has a 12 Å tetrahedral cage and a 16 Å octahedral cage.

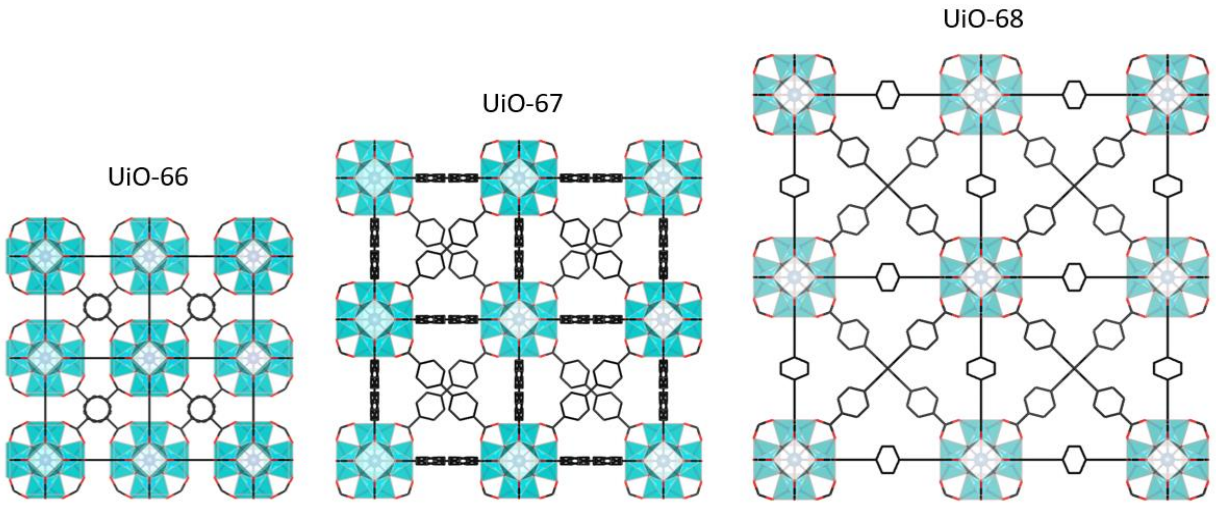

Figure 1.4: *Models of the UiO MOFs UiO-66, UiO-67 and UiO-68 with the linkers phenyl-4,4'-dicarboxylic acid, biphelyl-4,4'-dicarboxylic acid and triphenyl-4,4'-dicarboxylic acid respectively. The cyan Maltese crosses are the polyhedral of the zirconium clusters. Red represents oxygen and the black represents carbon. Hydrogens are not included in this model for better visualisation.*

What distinguished these MOFs from others at the time they were published, was their impressive stability and exceptionally large surface area. This makes them potentially useful for gas storage and heterogeneous catalysis.

MOF stability is directly correlated to the full coordination of inorganic nodes and organic linkers. Therefore, defects in MOFs are a topic that has gained a lot of attention in the last few years.[28-31] Many different types of defects may occur due to the complexity of the structures, but there are two main types. These are "missing linker" types and "missing cluster" types. As the names suggest, they are formed by either having an under-coordinated cluster or a nest of uncoordinated linkers. The defects can both be formed during the synthesis and after, post-synthetically. There have also been reports on forming them by heat-treating the materials.[28] During synthesis modulator-molecules that aid and slow down the formation of the frameworks can be used to control the amount of defects in the final product. Modulators used are often lower mono-carbon acids like formic acid and benzoic acid, which imitate a "half" linker.[32]

The UiO-MOFs can be post-synthetically modified to change some of the linkers into functionalized organic ligands. By grafting salt to functionalized organic linkers, transition metals can be incorporated into the MOF pores. By subjecting the functionalized MOFs to reducing conditions, nanoparticles of the metal can be formed inside the MOF-matrix, and can be used for catalytic purposes.[33, 34] The framework itself can also be used as a catalyst, by either

having open sites caused by missing linker type defects, or by having functionalized linkers.[35] By having reactions take place at the catalytic sites inside the MOF, only molecules that are small enough to fit inside the pores can be formed. This trait is the same as for zeolites used for catalysis; a so-called "shape selectivity".

In 2017 Gutterød *et al.* investigated Pt supported in a UiO-67 type metal-organic framework for CO_2 hydrogenation reactions.[34] Gutterød *et al.* found that although the system showed lower catalytic activity than other systems, it was an ideal system to further investigate the specific mechanisms that facilitated the formation of different products due to its exceptional stability.

Gutterød *et al.* found that when a UiO-67 MOF with 10% [2,2'-bipyridine]5,5'-dicaboxylic-linker was impregnation with Pt(II)Cl_4-salt, the salt was grafted to the nitrogen's in the [2,2'-bipyridine]5,5'-dicaboxylic-linker. By subjecting the catalyst to 1:9 H_2:inert flow at 350 °C, nanoparticles of Pt(0) was formed inside the MOF. XANES- and EXAFS-studies of the Pt revealed that after metalation the presence of Pt-Cl bonds, while after reduction the Pt-Pt bond became more dominant in the spectra, indicating the formation of mantellic platinum species.[34] These Pt nanoparticles proved to be able to facilitate the hydrogenation of carbon dioxide into CO, methane and methanol. Some discoveries later made by Gutterød *et al.* suggests that the methanol formation and the methane formation are not linked, but rather follow two separate reaction pathways, and that the framework itself takes part in the conversion of the carbon dioxide.[1] Computational studies together with both FT-IR and transient experiments indicated that the zirconium nodes are contributing to the reaction and formation of methanol together with the platinum particles.[1] Gutterød *et al.* postulated that the role of the Pt particles was to dissociate hydrogen and carbon dioxide to form CO and water. The dissociated hydrogen could then immigrate to the node together with adsorbed CO_2 and form methanol. This could only occur on open node sites, where the linkers were not taking up sites the node. The amount of exposed nodes (missing linker phenomena) will therefore affect the catalytic activity of the system. A schematic of the reaction mechanisms can be seen in ***Figure 1.5***.

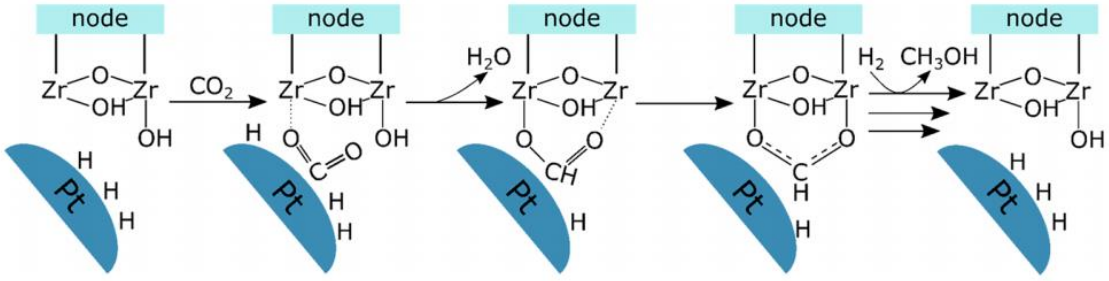

Figure 1.5: *Schematic presentation of the reacting mechanism in the Zr-node:Pt nanoparticle interface where methanol is formed through the formate intermediate. Copied from* ***Ref. 34****.*

H_2/D_2 and C^{12}/C^{13} transient experiments were also performed. They revealed that both hydrogen and deuterium could be changed out with the hydrogens from the hydroxyl groups on the Zr-node, and the FT-IR investigations revealed the formation of formate species on the Zr-node (the Zr-O-Zr sites). The H_2/D_2-transient reviled an inverse kinetic isotope effect which suggested that the rate limiting step involved hydrogen addition to an sp- or sp^2-hybridized carbon. Methanol formation through the formate intermediate involves two such steps. The C^{12}/C^{13} transient revealed that the formation of methanol came from a single pool of intermediates. It was also discovered that the catalyst may be poisoned by CO, limiting the adsorption of hydrogen on the platinum nanoparticle.

1.4 Aim of the thesis

The aim of this thesis has been two-fold: First, to study Pt nanoparticles formed in various UiO-66 and -67 metal-organic frameworks (MOFs) by Transmission Electron Microscopy (TEM), and second, to study the Pt-containing MOFs as catalysts for the CO_2 hydrogenation reaction, further building on the studies published by Professor Unni Olsbye's group at the University of Oslo.

Catalytic activity, material characteristics and kinetic studies of different UiO MOFs impregnated with platinum have been investigated. A series of different materials with slight alterations, ranging from platinum content to defect amounts, were investigated to further understand the mechanism of the CO_2-hydrogenation reactions taking place inside the UiO-66/Pt and UiO-67/Pt MOFs.

UiO-66 and UiO-67 with different functional linkers were first investigated. The purpose was to investigate if the chemical environment around the Pt nanoparticles influenced the catalytic activity of the systems. Three different synthesis batches of the same systems were also tested. Different batches of the same systems were also tested in order to put the results in context with published work.

The growth of the Pt nanoparticles and the active sites on the nanoparticles were then investigated. Three samples of the same parent MOF were loaded with different amounts of platinum. The samples were tested and characterized.

The importance of linker molecules for CO_2 hydrogenation was also investigated. In an attempt to induce defects and expose the Zr-nodes, controlled oxidation of reduced UiO-67/Pt MOFs was performed, and the resulting materials were tested and characterized.

2 Theory

In this section, the theories of heterogeneous catalysis, electron microscopy and catalytic kinetics are presented. The two main sources for this sections are the books "Concepts of Modern Catalysis and Kinetics" [15] and "Transmission Electron Microscope and Diffractometry of Materials, Graduate Text in Physics" [33].

2.1 The unit cell and packing of solids

The unit cell is the smallest repeatable part of a pattern and is used to describe symmetry. This is also the case for a crystal. There are eight crystal systems, each with their own cell parameters. For a cubic crystal system, the unit cell can be viewed as a box with vectors a, b and c going in the direction of x, y and z and with the angles α, β and γ, respectively.

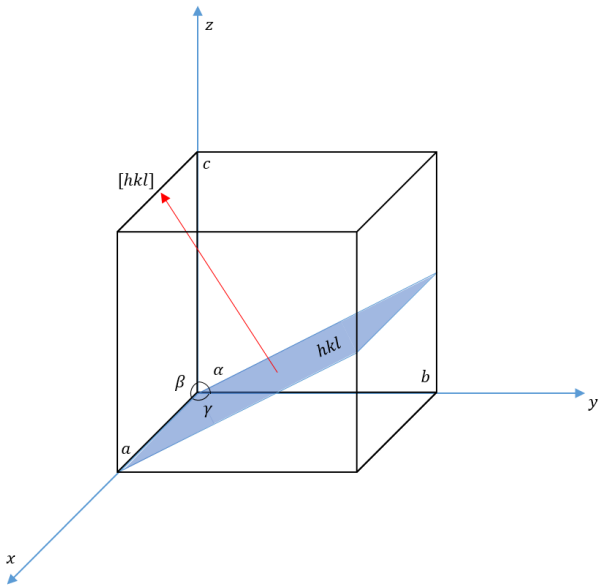

Figure 2.1: *A cubic unit cell with the sides a=b=c and the angles α=β=γ. The hkl plane and the [hkl] direction is shown. The plane in this case is 012 and the direction is [012].*

Within a crystal there can be a number of different directions and planes. The notation of these are called *Miller notations* and are *[hkl]* for the lattice direction, *hkl* for a set of equidistant planes and *(hkl)* for a single plane. The *[hkl]* direction is always perpendicular to the plane with the same *hkl* values. For example, a set of equidistant planes 012 divides each:

- *a* into 0 segments
- *b* into 1 segment

- *c* into 2 segments

Within the unit cell, the direction [012] is the direction that is normal to the plane 012. These indices, *hkl* are called the *Miller indices*.

For each of the systems there are different ways of packing the atoms/molecules. What decides which system a solid follows, is the electronic structure of its atoms/molecules. The cubic system has three different ways of packing; simple cubic, body-centered cubic (bcc) and face-centered cubic (fcc). The fcc packing is the densest packing a cubic structure can have. The densest packing regardless of crystal system is the hexagonal closed-packing (hcp). For this reason, most transition metals have either fcc or hcp packing. Platinum and the UiO MOFs which are studied in this work have fcc packing.

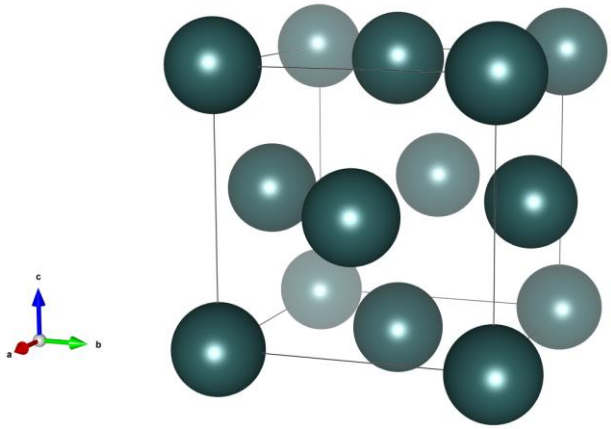

Figure 2.2: *An example a unit cell of a face centered cubic packing system. In this cell, there are 14 atoms. This is the unit cell of platinum.*

2.2 Adsorption and heterogeneous catalysis

Heterogeneous catalysis is a chemical process where the catalyst and reactants reside in different phases. Most often, when chemists talk about heterogeneous catalysis, they refer to a system where the catalyst is in the solid state and the reactants are in either gaseous or liquid state. When two or more atoms/molecules (often called adsorbates) approach the surface of a solid, the ways they interacts with it can be divided into two types; physisorption and chemisorption. The relative adsorption strength for physisorption is ΔH_{ads}=10 to 100 meV, while chemisorption usually have an adsorption strength of ΔH_{ads}=500 meV and above.[18]

2.2.1 Physisorption

Physisorption is an interaction characterized by the lack of a chemical bond between the adsorbate and the surface of the solid, in other words; no electrons are shared. These interactions can further be divided into a strongly repulsive part at close distances and Van der Waals interactions at longer distances (a few Å).

Van der Waals interactions come from a dipole interaction between the adsorbate and the solid surface. The electrons in the adsorbate particle create a dipole due to quantum fluctuations. This dipole induces an image in the solid. These two dipoles have opposite signs, so they attract one other. The Van der Waals potential can be described as the following proportion:

$$E_{p,W}(d) \propto -\frac{C_W}{d^3} \qquad \textbf{(2.1)}$$

where C_W is the Van der Waals constant for the system and d is the distance between the adsorbate and the solid surface.[18] This constant depends on the ability of an atom to polarize and the response of the solid. At small distances, the electrons from the adsorbate and the solid surface start to interact and repulse each other. This is the repulsive part of physisorption. If the adsorbate is a rare gas these will repel each other, but if the electrons can be shared and start to be attracted by the protons, a chemical bond can occur. The repelling potential can be described as the following proportion:

$$E_{p,R} \propto C_R e^{\frac{-d}{\alpha}} \quad \textbf{(2.2)}$$

where C_R is a constant. By plotting the two energies as a function of distance, and the sum of them, a "potential well" can be observed. This potential well describes at what distance the adsorbate will be physisorbed to the solid surface.

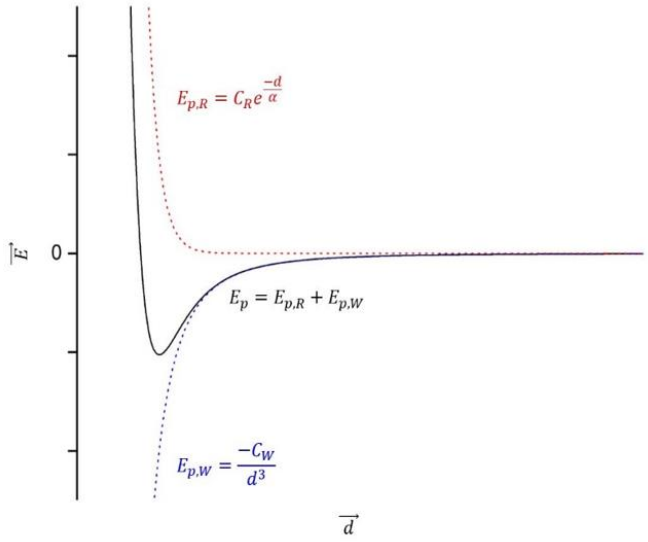

Figure 2.3: *The attractive and the repulsive physical forces that are felt by the incoming adsorbate with the distance d from a surface.*

Multi-layered physisorption is possible. The molecules/atoms in the first monolayer have high 2 dimensional freedom, but prefer certain sites such as capillaries and hollows on the solid surface.[18]

2.2.2 Chemisorption

Chemisorption is when an adsorbate is bonded to the surface of the solid when adsorbed. It is characterized by sharing of electrons between the two. In order to understand how this happens, orbital theory is briefly explained.

Consider two atoms with electron wave functions Ψ_A and Ψ_B that are well-separated. If these two atoms are brought closer together, their wave functions will overlap and form a combined wave function that describes the chemical bonding between them for a single electron.[18]

$$\Psi_{molecule} = c_1\Psi_A + c_2\Psi_B \qquad \textbf{(2.3)}$$

From the Hamiltonian of the system, the quadratic formula can be used to find out that there are two energy levels the electron can reside in; one bonding (σ) and one antibonding (σ^*) orbital.[18]

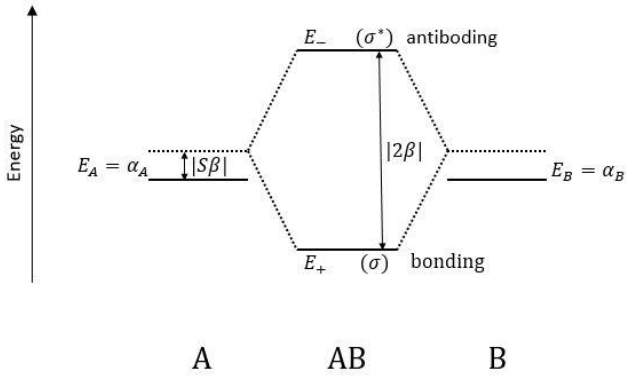

Figure 2.4: *Splitting of the electrons when a chemical bond is formed into bonding and antibonding orbitals. Adapted from Concepts of Modern Catalysis and Kinetics[18].*

This model is an energy diagram that shows the energy levels of the bonding and the antibonding orbitals when atom A and B form an overlapping wave function, AB, where the antibonding orbital reside at a higher energy level than the bonding. This model assumes that A and B are the same type of element, forming a homonuclear diatomic molecule. When a heteronuclear diatomic molecule is formed, the starting energy levels for A and B (when they are separate wave functions) will be different from each other.

When more than one atom is bonded together, like in a metal solid, other energy levels are added together, creating more bonding and antibonding orbitals.

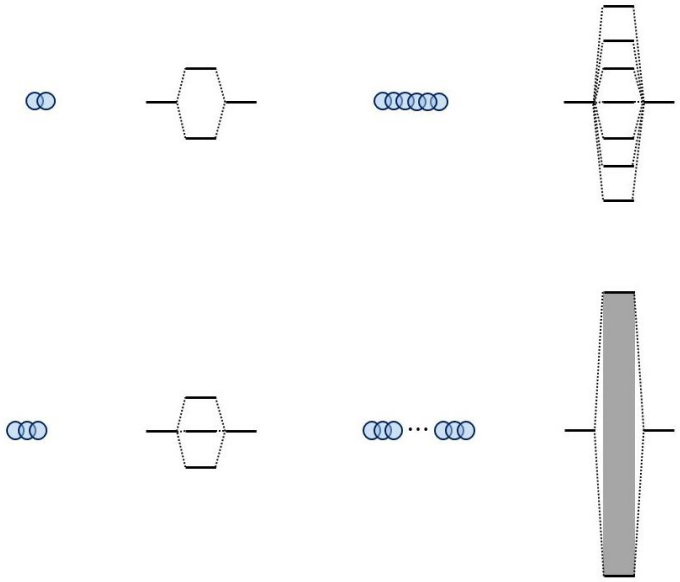

Figure 2.5: *A schematic of what happens when more and more atoms bond together, eventually forming a continuous energy band from the highest antibonding to the lowest the lowest bonding. This explains the behaviors of bulk metals. Adapted from Concepts of Modern Catalysis and Kinetics*[18].

When the number of atoms bonded together approaches an infinite amount, like in bulk metal solids, there are so many energy levels that it can be considered as a large continuous level, going from the lowest to the highest energy level. It is this phenomenon that give bulk metals some of their features, like a shared electron cloud.

Chemisorption can be defined as two types; associative and dissociative chemisorption. Associative chemisorption is when a molecule, for instance X_2, chemically bonds to the surface. Dissociative chemisorption is when the electronic structure of the molecule is changed to better conform to the surface. Usually it splits off the molecule into smaller fragments that can form stronger bonds to the surface. In the case for molecule X_2 it will turn into 2X. Only monolayer

chemisorption is possible. Once the surface is completely covered, no more chemisorption will occur.

2.2.3 Physisorption and chemisorption combined

A combination of physisorption and chemisorption occurs when an atom or a molecule approaches the surface of a solid.

As a molecule (for simplicity let's again use X_2) adsorbs to the surface of a solid, it will interact due to Van der Waals forces. If the molecule loses energy doing this, it will get trapped in the potential well, in other words, physisorbed on to the surface. If the molecule can rearrange its electronic structure, for instance interacting with the *sp*- and the *d*-bands of the metal surface, it may become chemisorbed. If the now chemisorbed molecule moves even closer to the surface, it will feel a strong repulsion from the surface. If the molecule manages to respond by again changing its electronic structure, it may dissociate into two separate chemisorbed atoms X.[18]

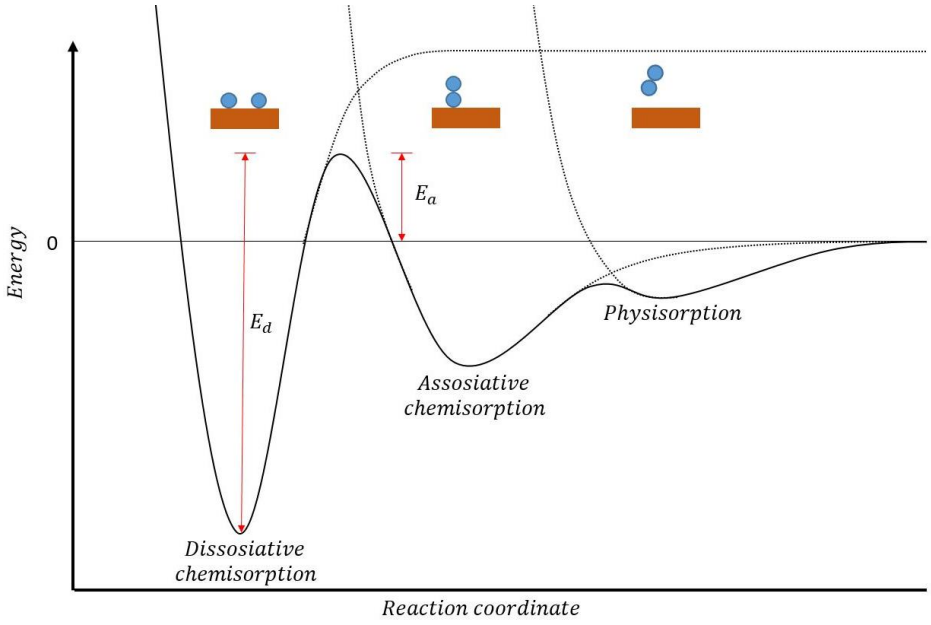

Figure 2.6: *The energy levels when an adsorbate first bonds physically before chemically bonding and eventually dissociate into separate atoms. E_a is the energy barrier that must be overcome for the adsorbate to dissociate and bond as individual atoms on the surface, while E_d is the energy needed to overcome in order to re-associate the dissociated atoms. Adapted from Concepts of Modern Catalysis and Kinetics[18].*

The figure shown above (***Figure 2.6***) is a simplified one-dimensional representation of what happens as a molecule interacts with a solid surface. In reality it is more complicated since it depends on the surface it interacts with, the orientation of the molecule and elements that interact. The barrier between physisorbed and associative chemisorbed is usually small, while the barrier between associative and dissociative chemisorption is larger.

2.2.4 Specific surface area and the BET equation

In practice, physisorption under controlled environment can be used to calculate the specific surface area (SSA) of a material. Compared to chemisorption, physisorption has the ability to adsorb into multiple layers. Brunauer-Emmet-Teller (BET) theory is a model that explain the physical adsorption of a gas on a solid surface. It is based on trying to figure out how many molecules are needed to adsorb to create a monolayer on the solid surface, and therefore considers the possibility of multiple layer adsorption. The BET equation uses the pressure and volume of an adsorbed gas to determine the SSA.

$$\frac{P}{V_a(P_0-P)} = \frac{1}{\chi V_0} + \frac{(\chi-1)}{\chi V_0}\frac{P}{P_0} \qquad \textbf{(2.4)}$$

where χ is the desorption rate constant for the two first layers, P is the pressure and V is the volume. V_0/P_0 is the volume/pressure of the monolayer. The area can be derived from this using the ideal gas law equation:

$$A = A_0 \frac{PV_0}{k_B T} \qquad \textbf{(2.5)}$$

where A_0 is the area each molecule occupies and and k_B is a constant. Nitrogen is often used due the shape and availability of the gas.

2.2.5 Properties of transition metals and metal-on-support catalysis

The transition metals are the metals that has partially filled *d* sub-shells, or that can give rise to cations with an incomplete *d* sub-shell. These elements can form many different oxide states due to the relative low energy difference between the different oxide states. Many of the transition metals also form paramagnetic compounds due to the unpaired *d* electrons.

At the edge of a solid, the density of the collective electron wave function is higher, meaning that there is a high density of electrons residing there. Since one of the constraints on the wave function is that it has to be continuous, some of the electrons “spill” out into vacuum. This

creates a dipole at the surface of the solid. An electron attempting to travel from the solid to the vacuum must overcome the work function barrier (Φ). This work function depends on the structure of the surface. For example, for *fcc* metals the (111) surface is the most densely packed and thus has the largest work function, compared to the (110) surface which is less dense and has a smaller work function. A surface also contains many defects. These defects will also affect the work function. The work function for a given surface structure generally increases from left to right in the periodic table, and is defined as:

$$\Phi = -e\phi - E_{Fermi} \qquad \textbf{(2.6)}$$

The Fermi level, E_{Fermi}, is the highest occupied energy level of an electron in a solid. By adding/subtracting electrons from the solid, the Fermi level will go up/down, respectively. The Fermi level separates the valence band and the conduction band and is usually at an equal distance from both. The potential between these two bands is called the band-gap. The bandgap can be said to represent the minimum energy required to excite an electron up to the conduction band. [18]

Usually transition metals are used as catalysts due to their broad *sp*-band and narrow *d*-band. When approaching the surface interface, the adsorbate level broadens into a Lorenzian shape that is lower in energy. The *d*-band almost functions as a molecular orbital itself towards the adsorbate. When a molecule (or an atom) approaches the surface both the bonding and antibonding orbitals split and fills up (up to the fermi level of the metal). When the molecule is adsorbed to the surface, its energy levels are broadened so that breaking and/or forming new bonds require less energy.[18]

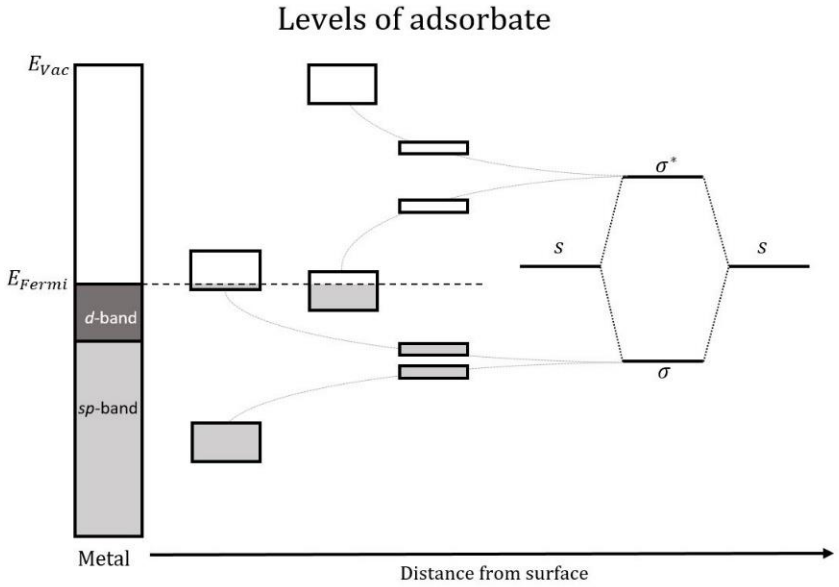

Figure 2.7: *An illustration of what happens when a diatomic molecule approaches a metal surface. The energy levels split and broaden. As a result, breaking and forming new bonds require less energy. Adapted from Concepts of Modern Catalysis and Kinetics*[18].

2.2.6 Nano catalysis

In normal nano catalysis, a nanoparticle is situated on a larger support particle. The nanoparticles are by themselves prone to sintering. A support's role is often to stabilize the metal particles, by e.g. charge transfer. These nanoparticles are subject to the *finite size effect*, which states that as particles get smaller, a higher percentage of the total atoms are on the surface of the particle. As a result of this, the atoms on the surface are less covered by other atoms, meaning more of their total electronic structure is exposed. This has many effects, one of which is that the melting and boiling point of a particle goes down as the particle gets smaller. Another effect is that the lattice of the crystals gets larger since there are fewer forces holding them together. This effect is called the quantum size-effect. The most important nanoeffect is that more of the electron cloud go outside the material since the atoms on the outside are less covered.

2.3 Properties of the electron, diffraction and electron microscopy

In order to understand the materials, chemists and material scientists have to characterize the materials. There are many different techniques that utilizes physical and chemical principles to measure and determine the properties of materials. One such technique is Transmission electron microscopy.

A Transmission electron microscope (TEM) is one of the most versatile characterization instruments used by material scientists to characterize materials. It works by looking at an electron beam after it has passed through a specimen. Due to the characteristics of the electron, a large amount of information can be obtained. Both material chemists and biochemists use such techniques

A Scanning electron microscope (SEM) works in a similar way as the TEM, but instead of looking at the beam after it has passed through the sample, it rather looks at the information from electrons that scatter back up from the sample. Due to this, the electron beam does not need to have as much energy.

A TEM normally operates with a beam acceleration energy between 60 to 300 kV, while a SEM normally operates at 1 to 30 kV. Once the electron hits the sample there is a vast amount of

information that can be collected. The beam may cause several different phenomena; e.g., excitation of the atoms, the production of x-rays and/or scattering of electrons. This last phenomenon is called diffraction. Other techniques also utilize the properties of diffraction, e.g. X-ray diffraction (XRD) and neutron diffraction. These techniques use photons and neutrons to diffract, respectively, which have different properties than electrons.

2.3.1 Properties of the electron

The electron is a subatomic particle and has a negative charge. They are classified as fermions (together with protons and their antiparticles) and are therefore subject to the *Pauli exclusion principle*, which states that no identical fermions can have the same four quantum numbers, meaning they cannot occupy the same quantum state. Due to its size, it can both be viewed as a single particle and a wave, just like the photon (the wave-particle duality). [18]

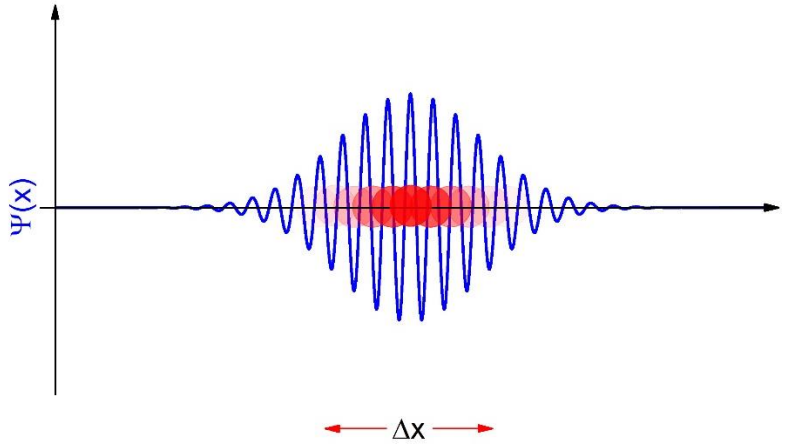

Figure 2.8: *The wave function of an electron, Ψ(x), as a function of distance x. The wavelet, and the red circles, gives an idea of where the electron is, and is based on the probability density of the function.*

The electron can be viewed as a spherical wave, which is propagating outwards from a point in space and time. It can be described by the wave function:[36]

$$\Psi = \psi_0 \, e^{-i(\omega t - \vec{k}z)} \qquad \textbf{(2.7)}$$

2.3.2 Electron scattering

When an electron hits an atom, it can undergo either elastic or inelastic scattering. Elastic scattering occurs when the electron does not lose any energy or momentum passing through the specimen, and inelastic scattering occurs when it loses energy and momentum passing through. The scattering itself occurs because coulomb forces make the electrons in the specimen and the incoming electron repulse each other, and the potential between the atomic core and the incident electron attract eachother[36].

When an electron undergoes inelastic scattering, two possible outcomes may occur to the bound electron: it can excite and relax producing x-rays in the process, or it excites all the way into vacuum producing auger electrons. Heavier elements tend to produce x-rays while lighter elements tend to produce auger electrons. When the electron undergoes elastic scattering the angle of the incident electron's trajectory is changed but it loses no momentum or energy. Diffraction experiments need elastic scattering, while spectroscopic experiments need inelastic scattering.

2.3.3 Laue Condition and the reciprocal lattice.

Two waves can interfere with each other in two different ways; constructive and destructive interference. When constructive interference occurs, the waves add together to create a single wave with a larger amplitude (energy). When two waves destructively interfere, they cancel each other because they are inverse of each other, the final wave has an amplitude/energy of zero. During an elastic scattering event that includes two points it is possible to derive the formula for when constructive interference occurs, using the *Miller indices*, which are an array of points that scatter.

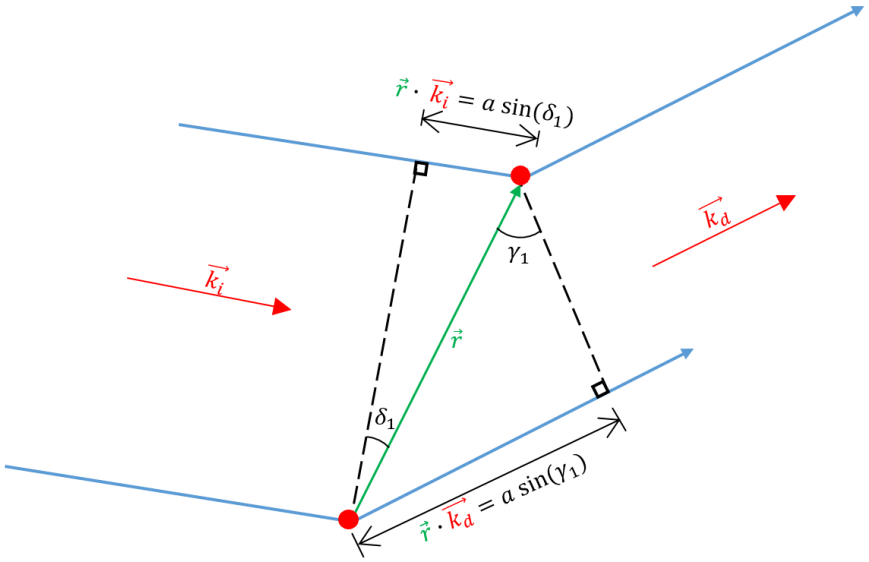

Figure 2.9: *An illustration depicting a wave, k_i, scattering from two points that are the distance r from each other creating the scattered wave, k_d. The geometry of this can be used to the find the Miller indices of the crystal.*

The *Miller indices* can be defined based on the wavelength in directions 1,2 and 3.

$$a(\sin[\gamma_1] - \sin[\delta_1]) = h\lambda \qquad \textbf{(2.8)}$$

$$b(\sin[\gamma_2] - \sin[\delta_2]) = k\lambda \qquad \textbf{(2.9)}$$

$$c(\sin[\gamma_3] - \sin[\delta_3]) = l\lambda \qquad \textbf{(2.10)}$$

Diffraction occurs when these, hkl, are integers. A more general formula for these simultaneous equations, is the *Laue equation*

$$\Delta\vec{k} = h\overrightarrow{a^*} + k\overrightarrow{b^*} + l\overrightarrow{c^*} = \vec{g} \qquad \textbf{(2.11)}$$

where $\overrightarrow{a^*}$, $\overrightarrow{b^*}$ and $\overrightarrow{c^*}$ are defined as the vectors to the lattice which is reciprocal to the lattice unit vectors $\vec{a}$, $\vec{b}$ and $\vec{c}$, meaning that they are multiplicative inverse of each other. Anytime a lattice is in real space, there simultaneously exists a reciprocal lattice in reciprocal space. Each plane in real space is described as a point in reciprocal space. It is essentially the Fourier transform of real space. The vector $\vec{g}$ in reciprocal space only equals the vector $\overrightarrow{\Delta k}$ in real space when constructive interference is true. This is known as the *Laue Condition*. This $\vec{g}$ has the properties that it is always perpendicular to the plane (hkl), and it is also related to the interplanar distance d in a manner like this:[36]

$$\Delta\vec{k} = |\vec{g}| = \frac{1}{d_{hkl}} \qquad \textbf{(2.12)}$$

2.3.4 Bragg's law

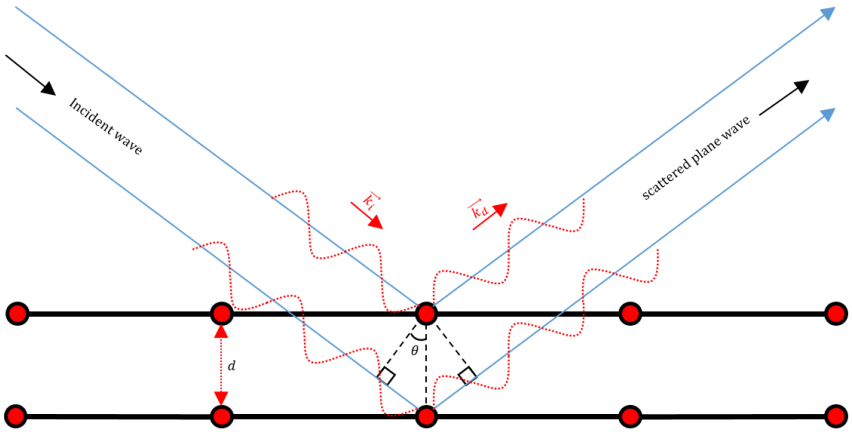

Figure 2.10: *An illustration of a wave scattering from two planes of points with the distance d from each other as described by Bragg's law.*

$$2d \sin\theta = n\lambda \quad \textbf{(2.13)}$$

The interplanar spacing, d, sets the different path lengths of the wave scattered from the top plane and the wave scattered from the bottom plane, meaning that the ray scattered from the bottom plane has a longer distance to travel than the wave scattered from the top plane. Constructive interference occurs when this difference in distance between the top and the bottom waves is equal to an integer of the wavelength, $n\lambda$. This is known as Bragg's law.[36]

2.3.5 Geometry of diffraction

A diffraction pattern of a specific material typically contains several distinct peaks. Each of these peaks corresponds to a specific interplanar spacing. This can be described by the formula:

$$Rd = \lambda L \qquad \textbf{(2.14)}$$

where R is the distance from the transmitted spot to a diffracted spot, d is the interplanar spacing that corresponds to that diffraction spot, the λ is the wavelength and the L is the length from the sample to the diffraction pattern. Usually the formula separates the real space from the reciprocal space.

$$\frac{d}{L} = \frac{\lambda}{R} \qquad \textbf{(2.15)}$$

This means that it is possible to calculate the parameters of a crystal based on its diffraction pattern.[36] Different operating-modes in TEM use these different physical phenomena to determine different information.

2.3.6 Operating-modes in TEM

When using a TEM there is the possibility to look at either a contrast image of the sample or a diffracted image of the sample. They both provide different information and have several applications. The heavier (Z) an atom is, the more it will diffract.

The diffracted image is an image of spots and lines with different intensities. Each of these spots (except the brightest spot in the middle, which is the transmitted beam) corresponds to a plane in the crystal that satisfies Bragg's law. By using the formula (geometry of diffraction) the *d*-spacing of the crystal can be calculated and the indexing of the crystal can be made. Indexing requires more than one diffraction pattern from different zone axes. Fourier transforming the image can simulate a diffraction pattern of a given image. If the crystal system in known, certain symmetrical patterns can give information of which zone axis is depicted.

Table 2.1: A table describing common symmetrical patterns that show up in the diffraction patterns for cubic systems (cubic, bcc or fcc).[36]

Zone axis	Diffraction symmetry in cubic crystals	Aspect ratio
[100]	Square	1:1
[110]	Rectangular (almost hexagonal of fcc)	$1:\sqrt{2}$
[111]	hexagonal	1:1:1

Imaging mode in TEM normally gives an image with different contrasts. An image will give contrast based on the amount of diffraction. An unaltered image will have 100% brightness in vacuum, where the transmitted beam is unaltered. The more diffraction, the more in contrast that point is. In TEM, there are many different techniques for contrast imaging. Usually they can be divided into two different main modes: direct imaging TEM and scanning TEM (STEM).

In direct imaging TEM the main technique is high resolution TEM (HRTEM). In HRTEM imaging the contrast comes from phase contrast. It is based on the fact that different diffracted waves have a different phase shift. The resolution of HRTEM is interatomic distances. This type of imaging can therefore give a lot of information about strain and stress in a solid on an atomic level.

STEM is a technique that uses a converged beam to form a point, which is then scanned over the surface of a sample. This is much like how a SEM works. Some techniques used are Annular bright field/bright field STEM (ABF/BF STEM), Annular dark field STEM(ADF STEM) and High angle annular dark field STEM (HAADF STEM). ABF/BF STEM only shows the electrons that have not been diffracted, or in the case of annular bright field; the lightest atoms with a scattering angle close to zero. ADF STEM is similar to the BF STEM, but instead of looking at the transmitted beam, the electrons that create the picture are the diffracted electrons. This means that the contrast is flipped. It is almost the same as ADT STEM, but in this case, the image is created from beams that have diffracted at a high angle. This technique is therefore best for heavier atoms which diffract with higher angles.

Spectroscopy can also be done in the TEM. The two main spectroscopic techniques are energy dispersive X-ray spectroscopy (EDS) and electron energy loss spectroscopy (EELS). In EDS, the X-rays detected are produced when the excited electrons decay. Different elements have different energy levels, meaning it will only send out specific X-rays. These X-rays can be used to identify what elements are present in the sample. Other sources such as plasmons and Bremsstrahlung X-rays can also contribute to the X-ray energy absorption spectrum.

Using information from characterization of a material, the chemical mechanisms can be investigated. These investigations are called Kinetic studies.

2.4 Chemical kinetics

Kinetics is the study of describing the rate at which a temporal change occurs in a system. Using this information, it can relate the rate to the reaction mechanisms and reaction coordination of the reaction. It includes investigation of how experimental conditions can influence the speed at which the reaction occurs and information of the yield of the reaction mechanisms and the transition states.

2.4.1 Chemical rate

The rate of reaction is defined as the change in concentration over time and is used to measure the speed, or rate, at which a product is formed. It can be defined as the function:

$$r = \frac{\Delta[n_a]}{\Delta t} \qquad \textbf{(2.16)}$$

where $n_{a,0}$ is moles of a and t is the time.

2.4.2 Conversion

Conversion, X_a, is the measurement of how much species a is converted in a chemical reaction. If the conversion is zero then no reaction has occurred, and if the conversion equals one, the reaction has gone to completion. It can be expressed using moles or molar flow rate.

$$X_a = \frac{n_{a,0} - n_a}{n_{a,0}} \qquad \textbf{(2.17)}$$

where $n_{a,0}$ is moles of a or molar flow rate of a going in to the reactor and n_a is the moles/molar flow rate from the reactor. The equation can then be rewritten as

$$n_a = n_{a,0} - n_{a,0} \cdot X_a \qquad \textbf{(2.18)}$$

Usually the conversion is given as a percentage rather than a decimal. In the case of a reaction where one reactant is turned into several products, the conversion can be expressed like this:

$$X = \frac{\sum x_{a\ atoms,j} \cdot n_{product,j}}{x_{a\ atoms,reactant} \cdot n_{reactant} + \sum x_{a\ atoms,j} \cdot n_{product,j}} \qquad \textbf{(2.19)}$$

where x is the number of atoms a in molecule j and n is the moles of molecule j.

2.4.3 Selectivity

Selectivity is the measurement of the fraction of the converted product that is converted to a specific product. It can also be given as a function of either moles or molar flow rate.

$$S_a = \frac{n_a}{n_a + n_b + \ldots + n_n} \qquad \textbf{(2.20)}$$

It is also given as a percentage, where 100% is the sum of all the different selectivity's towards the products. In the case of a reaction where one reactant is turned into several products, the selectivity towards product i can be expressed like this:

$$S_i = \frac{x_{a\ atoms,product\ i} \cdot n_{product\ i}}{\sum x_{a\ atoms,j} \cdot n_{product,j}} \qquad \textbf{(2.21)}$$

where x is the number of atoms a in molecule i / j and n is the moles of molecule i / j.

2.4.4 Yield

Yield is the measurement of the fraction of reactants that has turned a specific product. It can be derived from conversion and selectivity

$$Y_i = X_i \cdot \frac{S_i}{100\%} \qquad \textbf{(2.22)}$$

2.4.5 Turnover frequency and turnover number

Turnover frequency (TOF) is a measure of the moles product that is formed per catalytic site as a function of time, and can be expressed as the function

$$TOF = \frac{n_{product}}{t \cdot n_{catalytic\ site}} \qquad \textbf{(2.23)}$$

where $n_{product}$ is the moles of products produced, $n_{catalytic\ site}$ is the moles of catalytic sides and t is time. This equation can also be expressed as a function of rate.

$$TOF = r_{product}/n_{catalytic\ site} \quad \textbf{(2.24)}$$

TOF is a good unit with which to compare catalytic systems, regardless of concentration of catalytic site and conversion.

Turnover number (TON) is the measure of the total number of mole product formed per moles catalyst, and can be expressed as

$$TON = \frac{n_{product,total}}{n_{catalytic\ site}} \qquad \textbf{(2.25)}$$

TON can also be expressed as a function of TOF

$$TON = TOF * t_{total} \qquad \textbf{(2.26)}$$

where t_{total} is the total time of the experiment. This unit of measure is more relevant when comparing cyclic systems like homogeneous reactions and enzymatic reactions.

2.4.5.1 Active sites and TOF

In this thesis, the TOF was calculated following the method described below. Based on TEM images, an assumption was made that the Pt nanoparticles were spherical. The second assumption that was made was that the patina nanoparticles were the only catalytic active site. The reason for these assumptions were so that the materials could be compared regardless of

particle size and the amount of platinum loading. The third assumption was that all the platinum atoms that were exposed to the surface was considered an active site and not takin into account the different faces of the particles.

Based on TEM micrographs, the diameter of the particles were measured and the volume of the particles were calculated:

$$V_{Pt,NP} = \frac{4}{3} \cdot \pi \cdot \left(\frac{D_{Pt,NP}}{2}\right)^3 \qquad \textbf{(2.27)}$$

where $D_{Pt,NP}$ is the diameter of the platinum particles form TEM and $V_{Pt,NP}$ is the volume of the particle.

$$m_{Pt,NP} = \rho_{Pt,bulk} \cdot V_{Pt,NP} \qquad \textbf{(2.28)}$$

where $\rho_{Pt,bulk}$ is the bulk density of platinum and $m_{Pt,NP}$ is the mass of platinum.

$$n_{Pt,NP} = \frac{m_{Pt,NP}}{Mm_{Pt}} \qquad \textbf{(2.29)}$$

where Mm_{Pt} is the molar mass of platinum and $n_{Pt,NP}$is the number of moles platinum in the particle.

$$N_{Pt\ atoms,total} = n_{Pt,NP} \cdot N_A \qquad \textbf{(2.30)}$$

where N_A is Avogadros number and $N_{Pt\ atoms,total}$ is the number of platinum atoms in the particle The same was then calculated for the particles without the surface.

$$V_{Pt,NP\ w/o\ surface} = \frac{4}{3} \cdot \pi \cdot \left(\frac{D_{Pt,NP} - 2 \cdot D_{Pt,atom}}{2}\right)^3 \qquad \textbf{(2.31)}$$

where $D_{Pt,atom}$ is the diameter of one platinum atom and $V_{Pt,NP\ w/o\ surface}$ is the volume of the particle without the surface.

$$m_{Pt,NP\ w/o\ surface} = \rho_{Pt,bulk} \cdot V_{Pt,NP\ w/o\ surface} \qquad \textbf{(2.32)}$$

where $m_{Pt,NP\ w/o\ surface}$ is the mass of the particle without the surface.

$$n_{Pt,NP\ w/o\ surface} = \frac{m_{Pt,NP\ w/o\ surface}}{Mm_{Pt}} \qquad \textbf{(2.33)}$$

where $n_{Pt,NP\ w/o\ surface}$ is the number of moles platinum in the particle without the surface. The number of moles platinum that is on the surface particle was then calculated by subtracting the mole of the entire particle by the moles of the particle without the surface.

$$N_{Pt\ atoms,surface} = (n_{Pt,NP} - n_{Pt,NP\ w/o\ surface}) \cdot N_A \quad \textbf{(2.34)}$$

where $N_{Pt\ atoms,surface}$ is the number of atoms on the surface. The amount of active side platinum per gram catalyst was then calculated by using the weight percentage from EDS

$$N_{surface,Pt} = \frac{wt\%_{Pt} \cdot 100\%}{Mm_{Pt}} \cdot \frac{N_{Pt\ atoms,surface}}{N_{Pt\ atoms,total}} \qquad \textbf{(2.35)}$$

where $wt\%_{Pt}$ is the weight percentage form EDS, $N_{surface,Pt}$ is the number moles of active catalyst.

2.4.6 Reactors and plug flow reactor

Reactors are enclosed systems were chemical reactions take place. There are many different reactor designs used for different processes. One type of reactor is the plug flow reactor which is often used in laboratories. Plug flow reactors (PFRs) are reactors where the reactant feed goes straight through the catalyst without being mixed with it, like a filter plug in a tube, hence the name. As the reactant feed travels though the reactor, more of the feed converts into products and the concentration of reactants decreases. Both products and unconsumed reactants are present in the effluent exiting the reactor. Some of the advantages of PFRs is that it is an easy system with low pressure drops throughout the reactor. It is often used in kinetic studies since it is good for studying rapid changes inside the reaction. Some disadvantages are that temperature gradients and concentration gradients may be present throughout the reactor.

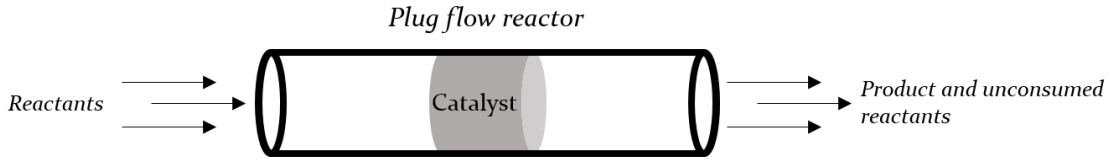

Figure 2.11: *An illustration of a plug flow reactor.*

The design equation for the flow rate in a plug flow reactor is:

$$r = F \cdot \frac{dC}{dV} + \frac{dC}{dt} \qquad \textbf{(2.36)}$$

Where F is the flow, C is the concentration, V is the volume and t is time. The rule of thumb for a plug flow reactor is that

$$\frac{\mathrm{d}_{reactor}}{\mathrm{d}_{particle}} \geq 10 \qquad \textbf{(2.37)}$$

to lower the influence of the reactor walls and that

$$\frac{lenght\ from\ catalyst\ bed}{\mathrm{d}_{particle}} \geq 50 \qquad \textbf{(2.38)}$$

to avoid bypass of the catalyst in the reactor.

2.4.7 Steady-state, intermediates and Rate-Determining Step.

Consider the reaction:

$$\mathrm{A} + \mathrm{B} \rightleftarrows \mathrm{C} + \mathrm{D} \qquad \textbf{(2.39)}$$

When this reaction occurs, the reactants A and B will approach each other. When they are close enough they will start to react and form the products C and D, intermediates. Intermediates are molecules that are formed and further reacts to give the products. These intermediates are often radical molecules, which are unstable and will not exist long. When chemical reactions take place over catalysts, these intermediates are often stabilized, making them easier to form so that the products can be formed. A chemical reaction will often have several intermediates that have different stability. The most stable and/or "slow" reaction step is called the rate-determining step. As the name suggests, the rate determining step is the step of the reaction that determines the rate at which the products are formed.

When a reaction first starts, there are a lot of changes in the system. Intermediates are being formed and used at different speeds and the systems is in chaos. Once the reaction has reached equilibrium, it is said to be at Steady-State. At Steady-State the system does not change over time as new reactants are introduced at the same rate at which the products are being formed.

2.4.8 Steady-state Isotopic Transient Kinetic Analysis

For a given heterogeneous catalytic reaction at steady-state, reactants form products through adsorbed intermediates. Steady-state isotopic transient kinetic analysis (SSITKA) permits measurement and quantification of these intermediates. The average surface residence time for an intermediate, τ_{res}, can be derived form the normalized transient response, $F(t)$.

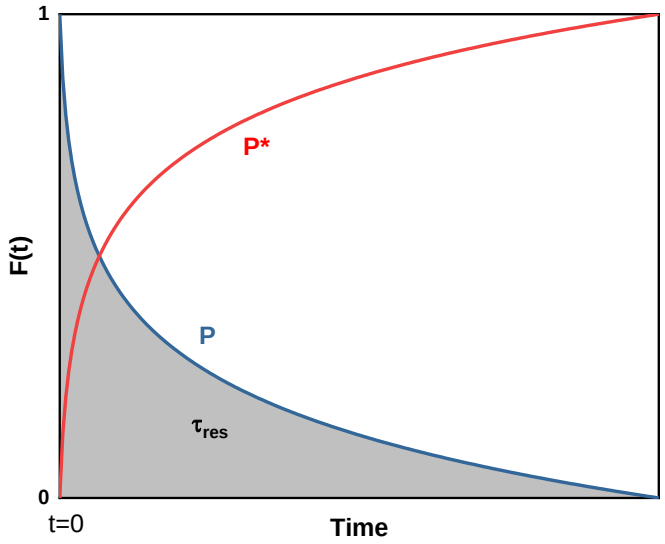

Figure 2.11: *Normalized transient curve for the species P and the isotope equivalent P*.*

$$\tau_{res} = \int_0^{\infty} F(t)dt = \frac{N_{ads}}{r} \qquad \textbf{(2.40)}$$

where N_{ads} is the amount of adsorbed intermediates and r is the rate of formation at steady-state.[37]

3 Experimental

This section describes the experimental set-ups applied in the thesis and the instruments used. For the instrumentation, a brief introduction to the technique is given, followed by the specifics of the instrumentation and experimental procedures.

3.1 Materials

3.1.1 Starting materials

The starting materials were UiO-66 and UiO-67 MOF with different modifications. The names of the samples that are investigated in this thesis are presented in ***Table 3.1***.

Table 3.1: the names of the samples included in this thesis.

Sample names	Section
UiO-66-BDC(100% NH_2)/Pt	
UiO-66-BDC(100% COOH)/Pt	**4.1.1**
UiO-66-BDC(10% NH_2)/Pt	
UiO-67-10% bipy/Pt	
UiO-67-10% bipy/Pt*	
UiO-67-10% bipy/Pt (H)	**4.1.2**
UiO-67-BN(10% bipy)/Pt	
UiO-67-100% bipy/Pt	
UiO-67-10% bipy/less Pt	
UiO-67-10% bipy/Pt *	**4.1.2**
UiO-67-10% bipy/ex Pt	
UiO-67-10% bipy/Pt** [a]	
UiO-67-10% bipy/Pt 4h	**4.1.2**
UiO-67-10% bipy/Pt 16h	

The "" and "**" are there to distinguish the different UiO-67-10% bipy samples. [a]the sample is also called UiO-67-10% bipy/Pt 0h.*

3.1.2 Metalation

The metalation process was done differently for UiO-66 and UiO-67 due to their different stability.

3.1.2.1 UiO-66 samples

The parent MOF was added to a round-bottom flask and mixed in 30 mL of distilled H_2O per gram MOF. Once the mixture was homogeneously dispersed another 30 mL of H_2O per gram MOF was added. This mixture was heated to 100 °C, whereupon $K_2Pt(II)Cl_4$ was added with a 1:1 functional linker:Pt ratio (1:10 for the samples with 100% functional linkers). The mixture was left to reflux overnight. Once completed the mixture was filtered and washed with 500 mL of H_2O heated to 100 °C three times before being dried overnight at 60 °C. The resulting powder was bottled and labeled, before being kept in a desiccator until testing.

3.1.2.2 UiO-67 samples

The parent MOF was added to a round-bottom flask and mixed in 30 mL of DMF per gram MOF. Once the mixture was homogeneously dispersed another 30 mL of DMF per gram MOF was added. This mixture was heated to 160 °C, whereupon $K_2Pt(II)Cl_4$ was added with a 1:1 functional linker:Pt ratio (1:10 for the samples with 100% functional linkers). The mixture was left to reflux overnight. Once completed the mixture was filtered and washed with 100 mL of DMF heated to 100 °C twice, then washed three times with 30 mL dry acetone before being dried overnight at 150 °C. The resulting powder was bottled and labeled before, being kept in a desiccator until testing. DMF was used due to the UiO-67 MOF being unstable in water.

3.1.3 Oxidation induced defects

The pre-oxidation the samples were done *in situ* in a quartz glass reactor. The pre-oxidation was carried out after the reduction of the Pt(II) to Pt(0). 0.600 g pressed sample was heated 5 °C/min up to 350 °C in 1:9 H_2/inert 40 mL/min, and kept there for 4 hours. After 4 hours the feed was switched to a 20 mL/min flow of synthetic air (O_2:inert 1:4) and kept there for X hours (X = 0, 4, 16). After 5 hours on stream, the feed was switched to inert 20 mL/min and the reactor was cooled to room temperature. After cooling, the sample was transferred to a separate glass vial and kept in a desiccator until further testing. The samples were not pressed again after testing due to the uncertain structural stability of the materials after burning.

3.2 Testing

To monitor the catalytic performance of the materials, a series of catalytic tests and kinetic studies were performed.

The rig used is called the "SSITKA"-rig (***Figure 3.1***). It is a rig with seven computer-controlled mass flow controllers (MFCs), four automatic 2-way 4-port valves, one manual 2-way 4-port valve and a 2-way 6-port valve. It had three different flow modes: Inert flow for flushing, reaction flow and activation flow. The automated 2-way 4-port valve was used to change between the flow-modes. The function of the 2-way 6-port valve was to pulse a gas mixture through the reactor during reaction (this feature was not used). The rig feeds into a computer-controlled reactor and then into a mass spectrometer and a gas chromatograph. Information about the temperature in the oven was recorded using thermocouples. The temperature inside the reactor tube was not recorded due to limitations with the reactor. Gas traveling through the activation and the reaction lines had the possibility to be sent through saturators filled with water. Both saturators were in a temperature-controlled water bath to control the vapour pressure of the water. The MFCs, automated valves, the reactor and the thermocouples were all controlled and monitored in the computer program LabVIEW.

The gas line that goes from the saturators to the reactor, and from the reactor to the gas chromatograph was heated with a resistance wire connected to 260 V autotransformers. During experiments the autotransformer was set to 75 V. The reason for this heating was to ensure that the products of the reaction stayed in the gas phase and did not condense and/or crystalize inside the tubing, as well as preventing the water vapour from the saturator from condensing in the line. The top and bottom of the reactor was further insulated using quartz wool. A manual needle-valve was connected on the line right after the reactor. This in order to increase the pressure on the line up to 8 bar. Pressures over the ambient pressure was required to drive the thermodynamics of reaction towards methanol.

When transient H/D switch tests were conducted, the Ar and H_2/D_2 lines were switched to Ar → CH4 20 and H_2/D_2 → MFC1. This was due to limitations of the mass flow controllers. A separate line coming from the neighbouring rig, was connected to the manual 2-way 4-port valve to avoid direct connection of hydrogen and oxygen.

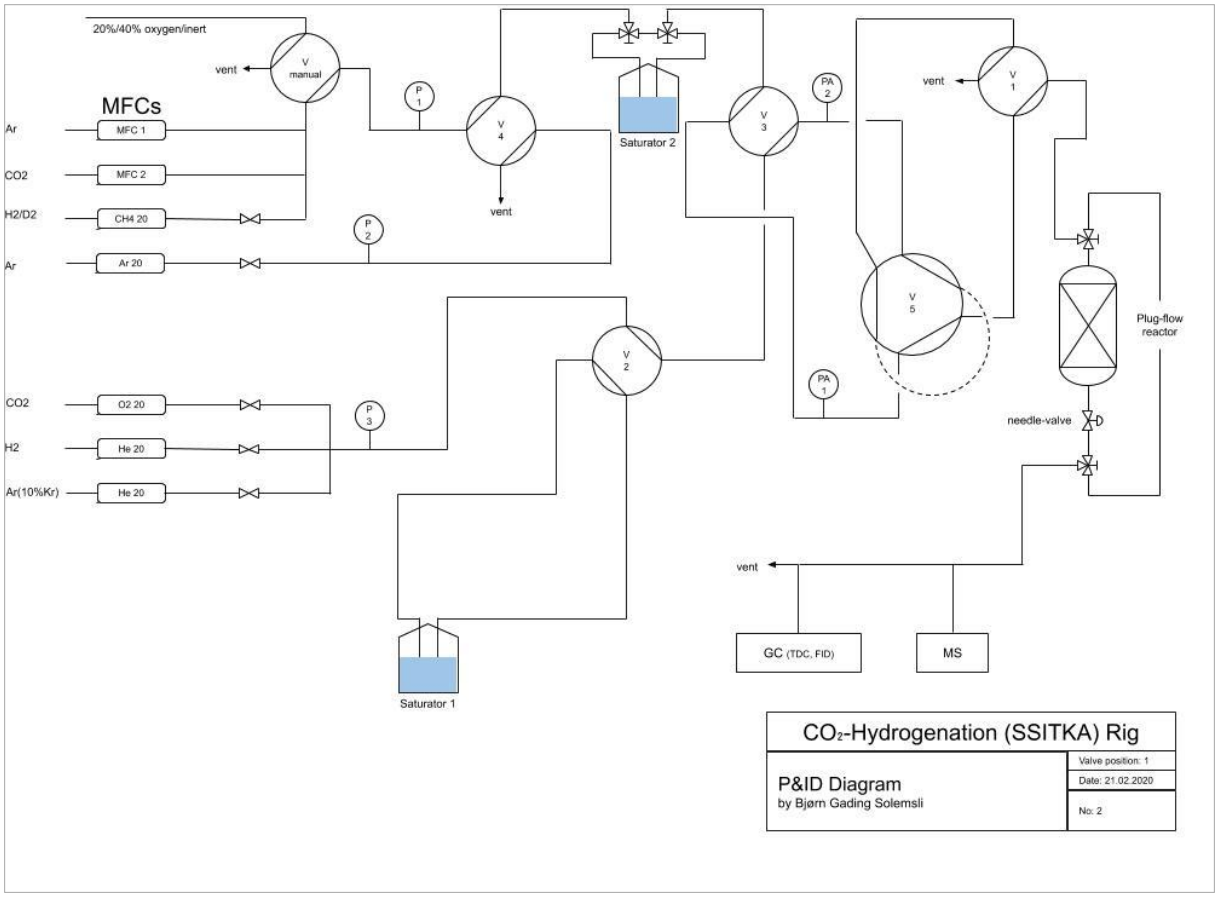

Figure 3.1: *A schematic of the rig that was used to perform all the catalytic tests. MFCs are the mass flow controllers, P and PA are the analog and the automatic pressure gauges, respectively. V are the automatic valves (2-way 4-port valves and one 2-way 6-port valve (V5)).*

3.2.1 Reactor

The reactor was a 6 cm long stainless-steel pipe with an i.d. of 0.8 cm. 14/16" Swagelok© connections were used to easily connect and disconnect the gas lines. The reactor was loaded with quartz wool in the bottom followed by pressed catalyst and silica separated by quartz wool. The extra quartz wool was used so that the catalyst would stay in the reactor, but also to separate the catalyst from the silica. The silica was added as an inert component to fully pack the reactor.

3.2.1.1 Test procedures

Before testing, the metalated MOFs were pressed with <1 metric ton of pressure using a pellet press and sieved to get a uniform bulk MOF particle size of 250-425 microns. Going much higher than 1 ton of pressure would risk damaging the structural integrity of the MOF. 200 mg of catalyst was used for all the tests.

In order to reduce the grafted platinum salts to form nanoparticles, the catalysts had to be activated in a reducing flow. A 1:9 H_2/Ar flow of 40 mL/min (STP) was used at elevated temperatures and atmospheric pressure for 4 hours.Due to the thermo-lability of the linkers containing amine-groups, the activation temperature of the UiO-66 samples was set to 200 °C, while the UiO-67 samples was activated at 350 °C, following previous studies.[34, 38] Activating for 4 hours were chosen, also based on the results of previous studies.[38]

Once the activation was complete, the reactor was cooled down to reaction temperature, and the feed was switched to reaction gases. Unless otherwise specified, tests were performed at 8 bar, 170 °C, using 200 mg catalyst and a CO2/H2/Ar(10% Kr) = 1:3:1 with a total flow of 20 mL/min (STP). A schematic of the temperature and pressure profiles is shown in ***Figure 3.2***.

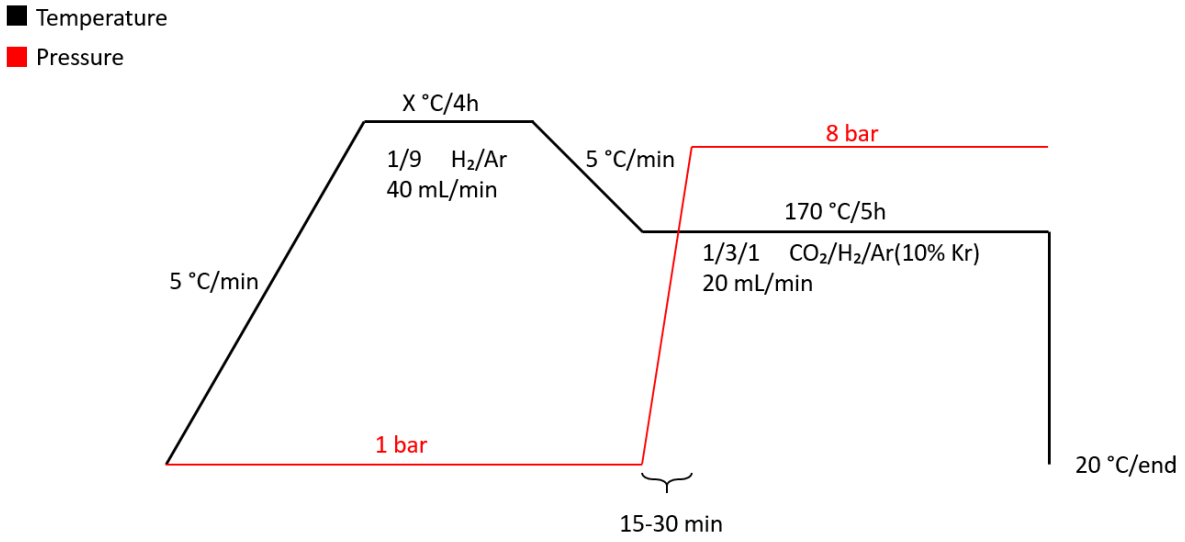

Figure 3.2: *Temperature and pressure profiles for the catalytic tests. The black line represents temperature and the red line represents pressure. Two different activation temperatures were used based on which MOF was tested (200 °C for UiO-66 samples and 350 °C for UiO-67 samples). Reactions were performed at 8 bar to promote the formation of methanol.*

The pressure was manually increased using the needle-valve positioned after the reactor. The increase in pressure was not consistent, but the target time from 1 to 8 bar was 30 minutes. The analysis of the feed coming from the reactor was not recorded until 8 bar was reached, but the stabilization of the pressure was monitored and logged throughout the experiment time. The contact times were chosen based on previous reports in literature.[1, 34]

3.2.2 Analysis

3.2.2.1 Mass spectrometer

An on-line Q-Ms (Pfeiffer) mass spectrometer was used to monitor the types of species observed in real time. A list of the masses that were traced can be seen in ***Table 3.3***.

Table 3.3: A list of the species traced and their m/z

Species	m/z
Hydrogen/deuterium	2, 3, 4*
Methane	15, 16, 17
Water	18 ,19, 20
Carbon monoxide	28
Methanol	31, 33, 34, 35, 36*
Argon	20, 40
Carbon dioxide	44
Dimethyl ether	46, 47, 51, 52
Krypton	84

**several m/z values were followed due to the possibility of deuterium occupying some or all the sites hydrogen can occupy, e.g. a hydrogen in methanol.*

3.2.2.2 Gas chromatograph

A *GC-TCD-FID (Aglient)* gas chromatograph was used to quantify the products from the reaction. It has two columns, HP-PlotU and CP-Molesieve 5A, and two detectors, TCD and FID. The carrier gases were Ar and He, although Ar was also used as the inert gas for the activation and reaction atmosphere. The GC takes one sample every 16 minutes. In column A, the lighter molecules (Kr, CO and methane) were recorded, while the heavier molecules (CO_2, water and methanol) were recorded in column B. Calibrations of the GC was done by doing several runs of known gas mixtures and averaging out the calibration constant using the formula

$$\frac{Signal\ from\ the\ GC\ (area)}{Known\ volume\ percentage} = calibration\ constant\ k \qquad \textbf{(3.1)}$$

The two different gas mixtures used for calibration were:

- 5% Ne, 2% H_2, 2% He, 5% CO_2, 2% CO, 5% CH_4, 5% C_2H_6, 5% C_3H_8, rest Ar
- 0.5% CH_3OH, 1% CH_4, 10% Ne, rest Ar

3.2.3 Data processing

Data from the GC was given as a summary text file that had be exported to a spreadsheet for data treatment. The peaks included in the summary file was peaks from O_2, N_2, Kr, CO, CH_4, CO_2, H_2O and CH_3OH. The spreadsheet software used throughout this work was *Microsoft Excel*©. Plotting of the data was done in *OriginLab* © for better visualization of the data.

3.3 General characterization and TEM characterization

Characterization with TEM was performed in order to analyze and monitor the platinum nanoparticles inside the MOF-matrix.

3.3.1 TEM

The microscope used for the TEM studies is a JEOL 2100F with a Schottky field emission electron gun (FEG). It is equipped with an energy dispersive X-ray spectrometer (EDS) system, electron energy loss spectrometer (EELS) system and a Charge-coupled device (CCD) camera which is integrated with the PC system of the microscope control. The instruments also had an Ultra high-resolution objective lens. It can have an acceleration voltage of 160 kV to 200 kV. The CCD and the EELS cameras are operated using a digital micrograph software. The EELS and EDS uses the Aztec software. The schematic of a typical TEM shown in ***Figure 3.3*** does not include the different detectors and cameras.

The setup of the magnetic lenses of the instrument can be divided into 4 different types: 1) condenser lenses (C1 and C2) whose main job is to render the divergent beam from the point source (FEG) to a parallel beam or converge the beam in STEM mode. 2) objective lenses which are situated before and after the specimen and serve to magnify the image of the specimen in either the focal, or back focal planes for direct- or diffraction imaging, respectively. 3) intermediate lenses whose job is to further magnify the image. 4) projection lens that further magnify the image and form the final image on the viewing screen.

The strength of the lenses can be adjusted by varying the electric current that passes through them. The lenses are subject to both spherical and chromatic aberrations. The JEOL 2100F also contains three apertures: the condenser aperture, the objective aperture and the selected area

(SA) aperture. These apertures are manually placed by adjusting in the x and y direction. Each aperture had several different sizes.

The instrument needs to be operated under high vacuum to stop the electrons from spreading. To capture any unwanted debris and improve the vacuum, the instrument is equipped with a "cold trap". It is important not to burn the cameras by over-exposing them to electrons. Because of this, it is necessary to always keep the intensity of the beam under control by spreading it and/or using the condenser aperture to block some of the beam.

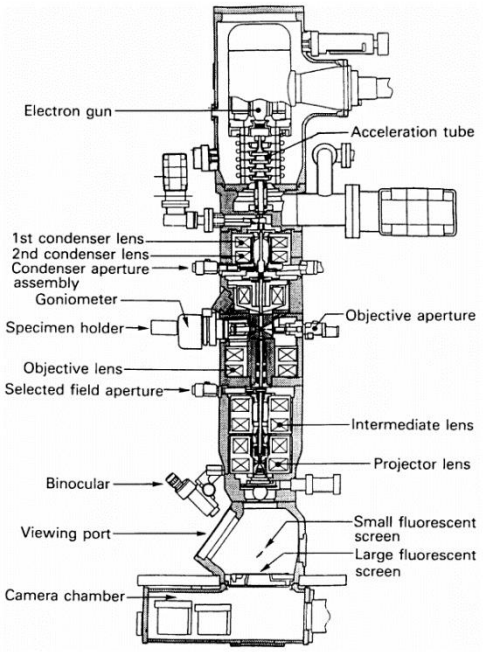

Figure 3.3: *A schematic of a TEM instrument taken from* ***Ref. 35****.*

The alignment of the instrument, the cameras as well as the beam is controlled with a panel fitted with switches and nobs situated around the microscope column, and via a computer that was connected to the instrument

A major difficulty with the analysis was that the MOF samples did not maintain their structure throughout the microscope session due to lack of conductivity and the fragility of the material. In order to combat this problem several measures were set in place. A small condenser aperture was inserted to block out a larger portion of the beam. To get better information of the whole sample and not just one part of the sample, the area of interest was often changed. In this way

the new areas analysed had not been as exposed to the electron beam making the microscope sessions easier.

3.3.2 Specimen holders and sample preparations for TEM

A double tilt holder was used when examining the samples in the TEM. As the name suggests, is has the possibility to tilt two orthogonal axes (X and Y). The holders are connected by wires to the instrument so that it can be computer controlled.

The samples were prepared by light crushing, before being transferred to 3 mm Cu grids covered by either holey of lacy carbon-films, with hole sizes in the range of 10-800 nm. Fine powders stick to the grid due to van der Waal forces. Sample preparation was also tried by first suspending the samples in solvent solution before transferring a few drops onto the Cu grid. This turned out to make the sample agglomerate into larger clusters on the grid and was therefore not used.

3.3.3 Powder X-ray Diffraction

Powder X-Ray Diffraction (PXRD) investigations were performed to evaluate if the materials were crystalline after synthesis and after catalytic testing.

The instrument used was a Chromium source powder XRD from Bruker, model D5000. It uses Cr K-α radiation selected by a Ge (111) monochromator. Measurements were performed with angles 2-50 2θ and at the fastest time setting (time scale 1). This was because only the crystallinity was verified, and no structural refinement was to be done.

3.3.4 Scanning Electron Microscopy

A Scanning Electron Microscope (SEM) was used to look at the "macro" structure (scale >100nm) to get good visualisation of the crystalline MOF morphology. The SEM had the capabilities to do a compositional analysis (EDS).

The SEM instrument used was a Hitachi SU8230 equipped with EDS systems. Sample preparation was done by mounting a two-sided carbon tape on a stainless-steel disc, before applying a small amount of sample.

When doing EDS the Pt/Zr would overlap in the spectra (Zr Lα=2.042 keV and Pt Mα=2.048 keV). Therefore, higher energy orbitals (Zr Kα= 15.744 keV and Pt Lα= 9.441 keV) had to be used.

In order to get these peaks, the beam had to be set to 30 keV, which can destroy the MOF due to overcharging. The samples were therefore sputtered with gold for 2 minutes, to increase the conductivity, giving the MOFs a longer "life-time" in the microscope. An example of the entire spectrum can be found in the supplementary information (***S8***). The microscope was operated with a high working distance and a current of 30 KeV. The EDS spectrum was taken from low magnification to get a more average composition of the material.

3.3.5 N_2 adsorption

The relative surface area of the materials was measured using N_2 adsorption. A BELSORP-mini II instrument was used. Nitrogen was adsorbed and desorbed at 77 K. The samples were pre-treated under vacuum and 80 °C and 350 °C for one and three hours, respectively. This was to remove water and other solvents/impurities in the samples. 50 mg of sample was used for each test. The SSA was calculated using the BET equation (***section 2.2.4***).

3.3.6 Thermo-gravimetric analysis

Thermo-gravimetric analysis (TGA) was used both to determine the amount of modulator present in the MOF and to test the stability of the MOF in the presence of oxygen at a set temperature over time.

The instrument used was a Netzsch STA449 F1 Jupiter. The heating time of the instrument was 30 °C/5 min up to 900 degrees in 25 mL/min N_2 flow. The samples were kept in 4 mm Al_2O_3 crucibles during the measurement. The theorized mass% was calculated with the assumption that the remaining mass was ZrO_2, giving the linker and the Zr a 1:1 ratio for a fully coordinated MOF. Theoretical weight percentage was compared to the actual weight percentage and used to determine the amounts of missing linkers per Zr-cluster.

3.3.7 Temporal analysis of Products

Temporal analysis of products (TAP) is a time-resolved technique for precisely performing kinetic characterization of a gas-solid reaction. Compared to other set-ups that use ambient or high pressure conditions, the gas pressure used in the TAP setup is low enough for Knudsen diffusion, where molecules can collide with the reactor walls but not with each other. The detection of effluent species was done by a Quadrupole Mass Spectrometer, directly connected

to the reactor. The TAP setup used is the TAP-3 at the Department of Chemistry at the University of Oslo.

3.3.8 Data processing

Gatan Digital Micrograph© was used for analysis, image enhancements and post-processing Fourier transformations of the data from TEM. The computer software *Particule2*© was used to more efficiently count and measure the size of the nanoparticles from TEM.[39]

The planes of the particles were determined by using a combined technique of two separate ways of determining the d-spacing. The first technique uses the Fourier transformation of the image, creating a simulated diffraction pattern, to manually measure the distance between the transmitted beam and the diffracted beam (see **2.3.3:** *Theory section, Laue condition and reciprocal lattice*). The second method uses a line scan across the fringes of the image and measure the intensity peaks and the distance between them in real space. Both these techniques are then compared to the theoretical spacing given by the *Miller indices* to find out zone-axes and the orientation.

PXRD data was analysed using a TOPAS software and the SEM images were directly converted to a vectorised image file. Atomic size and particle/MOF modelling were all done using the software Vesta © to visualize crystallinity data.

3.4 Source of uncertainties

Most of the uncertainties are due to human error, and since some of the valves on the testing rig was manually controlled this could affect the test conditions (temperature, partial and total pressure, contact times) inside the rector, thus the results.

Due to the low conversion of the systems investigated, some of the species present in the effluent (methane and other lower carbons) was below the detection limit of the GC. Because of this, only carbon monoxide and methanol is calculated. While investigating it TEM, the electron beam could affect causing the material to be altered while being investigate. No sign of this was observed, beyond the loss of crystallinity of the MOF within few seconds under the beam. It was therefore concluded that the material was not significantly affected to the extent of altering the results of the finding.

There may have been other sources of uncertainties present, but the three major contributors are the ones listed above.

4 Results and discussion

This chapter is divided into four main sections. The first section contains data about material specifics and general characterization of the analyzed materials before and after catalytic testing. The second section covers TEM measurements and analysis, while the third section is devoted to results from catalytic testing. Each of the sections are further divided into 4 sub-sections: *UiO-66 systems*, *UiO-67 systems*, *Different platinum loading in UiO-67-10% bipy/Pt** and *Oxidation induced defects in UiO-67-10% bipy/Pt***. In the TEM analysis chapter the UiO-66 systems and the UiO-67 systems are discussed in the same section. The final section discusses the results in a broader contexts.

4.1 General characterization

4.1.1 UiO-66 systems

The material specifics for, and provider of, the UiO-66 samples can be seen in ***Table 4.1.*** The specific surface area (SSA), the pore volumes (Vm) and crystallinity of the materials prior to metalation was reported by the provider.

Table 4.1: Material specifics for the UiO-66 samples.

Sample	UiO-66-BED(100% NH_2)	UiO-66-BED(10% NH_2)	UiO-66-BED(100% COOH)
Chemical formula	$Zr_6O_4(OH)_4A_aB_bC_cM_m$	$Zr_6O_4(OH)_4A_aB_bC_cM_m$	$Zr_6O_4(OH)_4A_aB_bC_cM_m$
BDC:Zr cluster ratio (a)	0	5.3[¤]	0
BDC(NH_2):Zr cluster ratio (b)	6[¤]	0.5[¤]	0
BDC(COOH):Zr cluster ratio (c)	0	0	6[¤]
Missing linker:Zr cluster ratio (m)	0	1	0
SAA ($m^2\ g^{-1}$)	957	1204	N/A
Vm ($cm^3\ g^{-1}$)	0.341	0.429	N/A
Pt amount (wt%)	6.0	4.9	6.8[‡]
Pt/Zr ratio	0 12	0.10	0.16
PXRD	Crystalline, single phase	Crystalline, single phase	Crystalline, single phase
Decomp. Temp. (°C)	350	420	460
Provider	ProfMOF A/S	ProfMOF A/S	ProfMOF A/S

A:BDC, B:BDC(NH_2) C:BDC(COOH), M:modulator/missing linker. The missing linker:Zr cluster ratio was estimated from TGA measurements. ¤ linker ratio estimated from synthesis from, not H^1NMR. ‡ metalation performed in this thesis.

Decomposition curves from TGA are presented in ***Figure 4.1***. The curves are of the samples prior to metalation and reveal that the samples had small amounts of defects. The **UiO-66-BDC(100% NH_2)** and the **UiO-66-BDC(100% COOH)** seem both to be close to fully coordinated, while the **UiO-66-BDC(10% NH_2)** have on average one missing linker per Zr-cluster (22,4 mass% less than the theoretical).

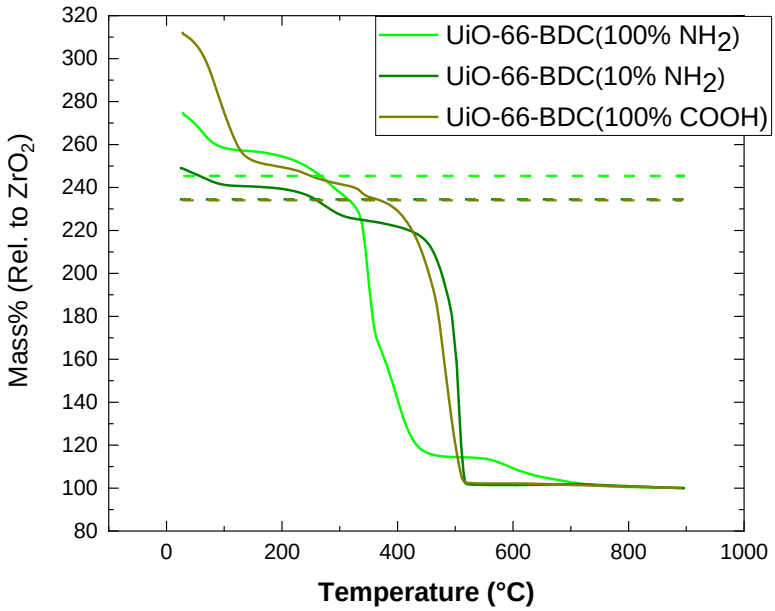

Figure 4.2: *TGA curves of the samples prior to metalation. The dotted lines are the theoretical mass% with fully coordinated clusters. The **UiO-66-BDC(10% NH_2)** and the **UiO-66-BDC(COOH)** theoretical mass% lines overlap.*

The UiO-66 samples were impregnated with $K_2Pt(II)Cl_4$ and reduced as described in the experimental section (section **3.1.1**). After metalation, the samples had three different colours; light yellow (**UiO-66-BDC(100% NH_2)/Pt**), light gray (**UiO-66-BDC(10% NH_2)/Pt**) and navy blue (**UiO-66-BDC(100% COOH)/Pt**). The samples showed to be crystalline prior to metalation, but only the two amino samples maintained crystallinity after testing. PXRD data measured after testing are presented in ***Figure 4.2***. **UiO-66-BDC(COOH)/Pt** only gave a weak signal, which suggests that the sample lost its crystallinity during testing. Some of the peaks at $2\theta > 10$ may originate from solvent and uncoordinated linkers inside the MOF-matrix.

The loss of crystallinity for the **UiO-66-BDC(COOH)/Pt** may come from platinum not being grafted to the 1,3,4-benzotricarboxylic acid linkers, causing the platinum to form a different morphology. This may also explain why the colour after metalation was so different. TGA measurements show no indication of lesser material stability than the two other samples, indicating that the reduction step may be the cause of the loss of structure.

After testing the samples all turned gray, but the **UiO-66-BDC(COOH)** sample had a much darker gray color. This gray colour indicate that the platinum in the samples had been reduced to metallic platinum. ***Table 4.2*** shows the calculated wt% of each of the samples from EDS. This was done post testing to more accurately portray the Pt/Zr-ratio in the active samples.

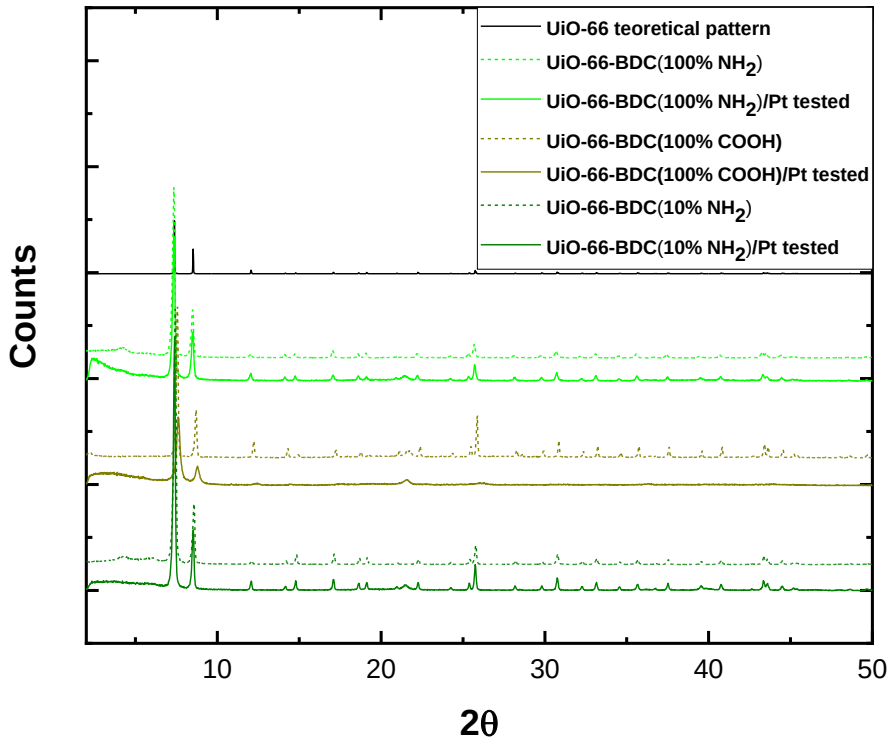

Figure 4.2: *PXRD diffractograms showing the crystallinity of the UiO-66 samples prior to metalation and after testing.*

Table 4.2: Weight percentage (wt%) of Zr and Pt calculated using SEM-EDS.

Sample	Zr amount (wt%)	Zr σ (wt%)	Pt amount (wt%)	Pt σ (wt%)	Pt/Zr ratio
UiO-66-BDC(100% NH_2)/Pt	24	0.47	6.0	0.13	**0.12**
UiO-66-BDC(100% COOH)/Pt	20	0.40	6.8	0.15	**0.16**
UiO-66-BDC(10% NH_2)/Pt	24	0.47	4.9	0.11	**0.10**

4.1.2 UiO-67 systems

The material specifics for the UiO-67 samples can be seen in ***Table 4.3***. The UiO-67 samples had different functionalized linkers compared to the UiO-66 samples.

Table 4.3: Material specifics for the UiO-67 samples.

Sample	UiO-67-10% bipy	UiO-67-10% bipy*	UiO-67-10% bipy (H)	UiO-67-BN(10% bipy)	UiO-67-100% bipy
Chemical formula	$Zr_6O_4(OH)_4A_aB_b$ C_cM_m	$Zr_6O_4(OH)_4A_aB_b$ C_cM_m	$Zr_6O_4(OH)_4A_aB_b$ C_cM_m	$Zr_6O_4(OH)_4A_aB_b$ C_cM_m	$Zr_6O_4(OH)_4A_aB_b$ C_cM_m
bpdc:Zr cluster ratio (a)	4.52[34]	4.75	5.35	0	0
bipy:Zr cluster ratio (b)	0.54[34]	0.59	0.58	0.5*	5.4*
BN:Zr cluster ratio (c)	0	0	0	5.3*	0
Missing linker :Zr cluster ratio (m)	0.3[34]	0.6	0.3	0.6	0.6
SAA (m^2 g^{-1})	2683	2299	2375	N/A	N/A
Vm (cm^3 g^{-1})	1.03	0.819	0.846	N/A	N/A
Pt amount (wt%)	1.03	1.91	1.11	0.69	3.53**
Pt/Zr ratio	0.05	0.04	0.02	0.03	0.05
PXRD	Crystalline, single phase	Crystalline, single phase	Crystalline, single phase	Crystalline, single phase	Crystalline, single phase
Decomp. Temp. (°C)	500	500	500	480	480
Provider	Dr. Sigurd Øien-Ødegaard	Dr. Gurpreet Kaur & ProfMOF A/S	Dr. Gurpreet Kaur & ProfMOF A/S	Dr. Gurpreet Kaur	ProfMOF A/S

***A**:bpdc-linker, **B**:bipy-linker **C**:BN-linker, **M**:modulator/missing linker. The missing linker:Zr cluster ratio was estimated from TGA measurements. *estimated from synthesis ratios, not H^1NMR **metalation performed in this thesis.*

The samples **UiO-67-10%bipy/Pt** and **UiO-67-10%bipy/Pt*** are the same material but from two different synthesis batches. Both batches have been reported earlier by Gutterød *et al.*.[1, 34] The reason for including both samples in this work was to investigate the reproducibility of the

batches and to be able to compare this work with published results. Compared to the other samples, the **UiO-67-BN(10% bipy/Pt)**, had smaller pores due to the size of the [1,1'-binaphthalene]-4,4'-dicarboxylic acid linkers taking up more space than the biphenyl-linkers. It was suggested that the two nitrogens in the bipyridine-linker would help facilitate the splitting of hydrogen, so a sample with 100% bipyridine-linker was also analyzed for comparison. Formenti at al. reported that the catalytic activity of Co nanoparticles on carbon was closely related to the amount and the type of nitrogen atoms which suggested a heterolytic activation of dihydrogen.[40] DFT calculations by Vilé *et al.* on a single site Pd on carbon nitride revealed that the heterolytic dissociation of molecular hydrogen, left one hydrogen bound to a nitrogen.[41]

Decomposition curves from TGA can be seen in ***Figure 4.3*** *and* show that the samples had defects. The **UiO-67-BN(10% bipy)** sample has a higher mass% plateau than the rest due to the binaphtyl-linker being heavier than the other linkers.

The difference between the **UiO-67-10% bipy*** and the **UiO-67-105 bipy (H),** was that the **UiO-67-105 bipy (H)** sample had been post-synthetically "healed" by exchanging the modulator with [2,2'-bipyridine]5,5'-dicaboxylic acid linkers. The difference between these two is clear from the TGA curves (maroon line vs. red line). The samples all appear to not be fully coordinated. The **UiO-67-100% bipy**, the **UiO-67-BN(10% bipy)** and the **UiO-67-10% bipy*** samples all have about 2/3 missing linkers per cluster (32.5 mass%, 45 mass% and 32 mass% less than the theoretical plateau, respectively). The healed version of **UiO-67-10% bipy** had on average 1/3 missing linkers per cluster (10 mass% less than the theoretical), proving that it had been "healed".

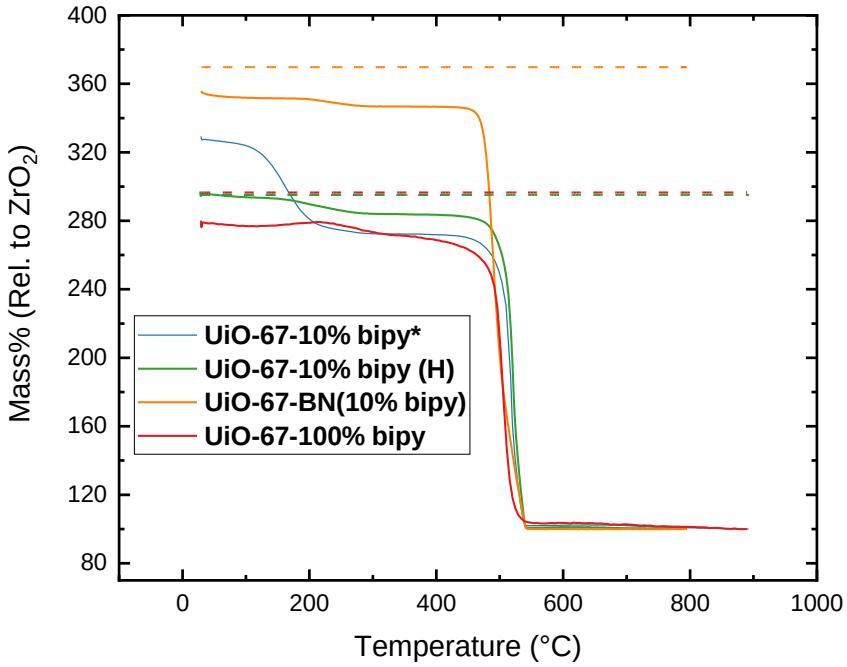

Figure 4.3: *TGA curves of all the UiO-67 samples except the* ***UiO-67-10% bipy*** *parent sample that has been reported on in literature[34]. The dashed lines are the theoretical mass% for samples with fully coordinated clusters.*

The UiO-67 samples were all impregnated using the method mentioned earlier in the experimental section (section **3.1**). The samples had all a light yellow colour after metalation, with the **UiO-67-100%bipy**-sample being the most yellow.

The crystallinity of the **UiO-67-10% bipy**, the **UiO-67-10% bipy*** and the **UiO-67-10% bipy (H)** samples has been reported earlier.[34, 42] The UiO-67 samples seem to all have retained their crystallinity after testing, as seen in ***Figure 4.4***. The peak at 28 2θ present in the diffractograms form the **UiO-67-100% bipy** sample prior to metalation may come from uncoordinated bipy-linkers in the MOF matrix. After testing, all samples had the same tint of light gray, indicating reduction of Pt(II) into metallic Pt(0).

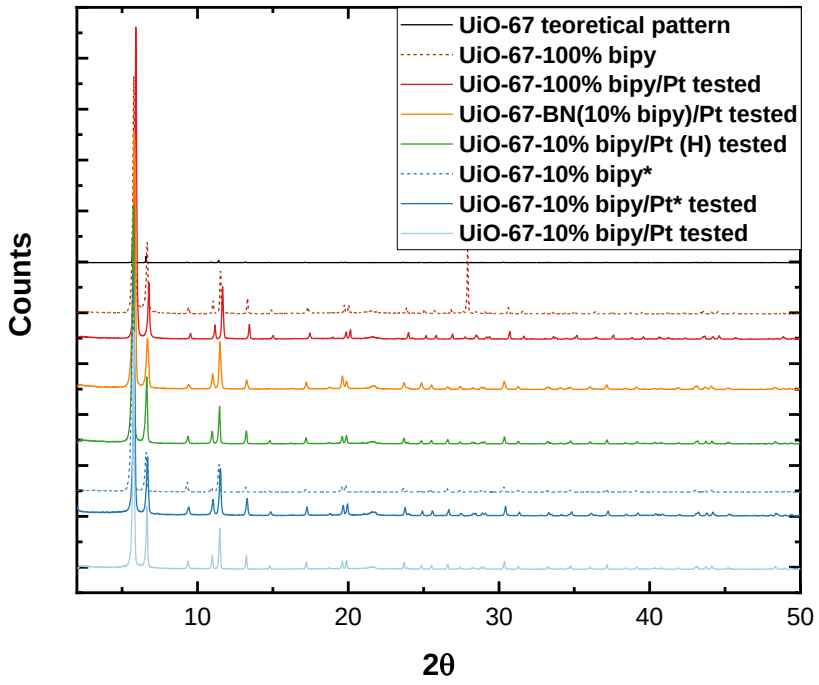

Figure 4.4: *Diffractograms of UiO-67 samples after testing. All samples seem to still be crystalline.*

Table 4.4 show the calculated wt% for each of the samples from EDS. The **UiO-67-100% bipy** sample had a larger Pt loading which may have been due to the metalation step. The platinum in the samples were added with a metal:functional-linker ratio of 1:1. The same amount of metal salt was used in the metalation of the **UiO-67-100% bipy/Pt** sample as if it was a 10% functional-linker content, to make it comparable.

This can be explained if not all the metal salt is grafted to all of the linkers. This leads to some functional-linkers without $PtCl_4^{-2}$ coordinated to it. In the case of the **UiO-67-100% bipy/Pt**, more of the metal salt may have been coordinated due to the excess of functional linkers compared to the sample with only 10% bipy linker. The **UiO-67-100% bipy/Pt** sample have a higher Pt/Zr ratio than the rest, even though they should have the same theoretical amount, which further supports this statement.

Table 4.4: The weight percentage (wt%) of Zr and Pt calculated using SEM-EDS.

Sample	Zr amount (wt%)	Zr σ (wt%)	Pt amount (wt%)	Pt σ (wt%)	Pt/Zr ratio
UiO-67-10% bipy/Pt	10‡	0.23	1	0.04	**0.05**
UiO-67-10% bipy/Pt*	25	0.49	2	0.09	**0.04**
UiO-67-10% bipy/Pt (H)	24	0.48	1	0.05	**0.02**
UiO-67-BN(10% bipy)/Pt	10	0.23	0.7	0.04	**0.03**
UiO-67-100% bipy/Pt	23	0.50	4	0.09	**0.07**

‡*the low wt% is due to the area the spectrum was taken from. The Pt/Zr ration is still valid.*

4.1.3 Different platinum loadings in UiO-67-10% bipy/Pt*

The **UiO-67-10% bipy*** parent MOF was metalated with three different amounts of platinum salt. The three different theoretical Pt/Zr ratios were 0.3, 0.6 and 0.72 for **UiO-67-10% bipy/less Pt**, **UiO-67-10% bipy/Pt*** and **UiO-67-10% bipy/ex Pt**, respectively. After metalation, the platinum content was recorded using EDS, as seen the ***Table 4.5***.

Table 4.5: The zirconium and platinum amount in the samples; UiO-67-10% bipy/Pt*, UiO-67-10% bipy/ex Pt and UiO-67-10% bipy/less Pt.

Sample	Zr amount (wt%)	Zr σ (wt%)	Pt amount (wt%)	Pt σ (wt%)	Pt/Zr ratio
UiO-67-10% bipy/less Pt	15‡	0.15	3	0.03	**0.03**
UiO-67-10% bipy/Pt*	25	0.49	2	0.09	**0.04**
UiO-67-10% bipy/ex Pt	23	0.46	4	0.09	**0.08**

‡*the low wt% is due to the area the spectrum was taken from. The Pt/Zr ration is still valid.*

4.1.4 Oxidation induced defects in UiO-67-10% bipy/Pt**

TGA analysis of the **UiO-67-10%bipy/Pt** sample with a constant temperature was performed to explore what rate the organic compounds would oxidize and burn off. Temperature selected for burning was 350 °C, and was chosen to mimic the activation temperature. The samples were calcined for 4 hours and 18 hours. The mass loaded were 6.3 mg and 6.2 mg, respectively. The colour of the samples after TGA was dark gray and black. This colour change indicate that the samples have been pyrolyzed into coke parallel to being oxidized . The curve is shown in **Figure 4.5**. Most of the linker had burned off after 600 minutes, in synthetic air (20% O_2, 80% inert). The similarity of the red and yellow lines shows the reproducibility when burning the

material in an oxidizing atmosphere. Even though this is a specific batch of the **UiO-67-10% bipy/Pt** material, the same behavior is expected for similar materials.

Based on these results, a new batch of UiO-67-10% bipy (**UiO-67-10% bipy/Pt****) was impregnated with Pt and investigated. The material specifics can be seen in ***Table 4.6***.

TGA curves show that the material has 2/3 missing linkers per cluster (23.4 mass% less than the theoretical curve) similar to the **UiO-67-10% bipy*** sample from section **4.1.2**. The decomposition plot can be seen in ***Figure 4.6***. The sample looked to be crystalline both before metalation and after testing. The diffractograms can be seen in ***Figure 4.7***.

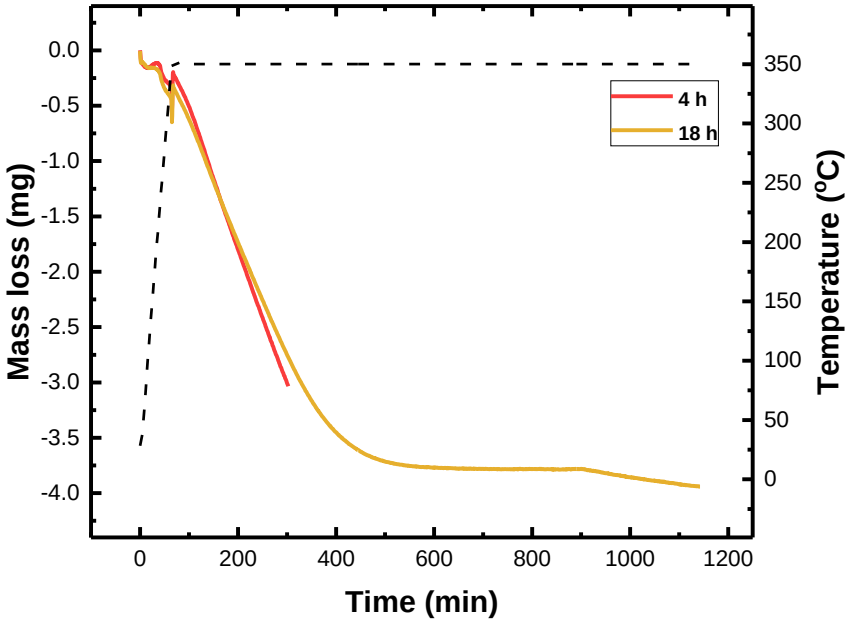

Figure 4.5: *Mass loss as a function of time and the temperature profile as a function of time with the UiO-67-10% bipy/Pt* material. The left y-axis is mass loss and the right y-axis is temperature.*

Table 4.3: Material specifics for the UiO-67 samples.

Sample	UiO-67-10% bipy**
Chemical formula	$Zr_6O_4(OH)_4A_aB_bC_cM_m$
bpdc:Zr cluster ratio (a)	5*3
bipy:Zr cluster ratio (b)	0.5*
BN:Zr cluster ratio (c)	0
Missing linker :Zr cluster ratio (m)	0.6
SAA ($m^2\ g^{-1}$)	2422
Vm ($cm^3\ g^{-1}$)	0.897
Pt amount (wt%)	2.59**
Pt/Zr ratio	0.05
PXRD	Crystalline, single phase
Decomp. Temp. (°C)	500
Provider	ProfMOF A/S

***A**:bpdc-linker, **B**:bipy-linker **C**:BN-linker, **M**:modulator/missing linker. The missing linker:Zr cluster ratio was estimated from TGA measurements. *estimated from synthesis ratios, not H^1NMR **metalation performed in this thesis.*

As previously observed by TG experiments, the material loses a significant amount of mass when being exposed to synthetic air at elevated temperatures. In order to further investigate this oxidation process, an experiment using a Temporal Analysis of Product (TAP) set up was conducted. The spectra can be seen in ***Figure 4.6***.

The TAP test was done to investigate what comes off the MOF when it is subjected to oxygen at higher temperatures. The test was done at 350 °C with a 5 °C/min ramp-up in inert atmosphere, before switching to oxygen. A leak-valve was utilized to feed small amounts of gas into the reactor. The reactor itself was kept at low pressure (close to vacuum) and fed directly to a mass spectrometer. The masses monitored were in the range 1-200 AMU. For this experiment the platinum sample was not reduced before oxidation. This decision was made to be able to see the oxidation of MOF without interference from the platinum particles.

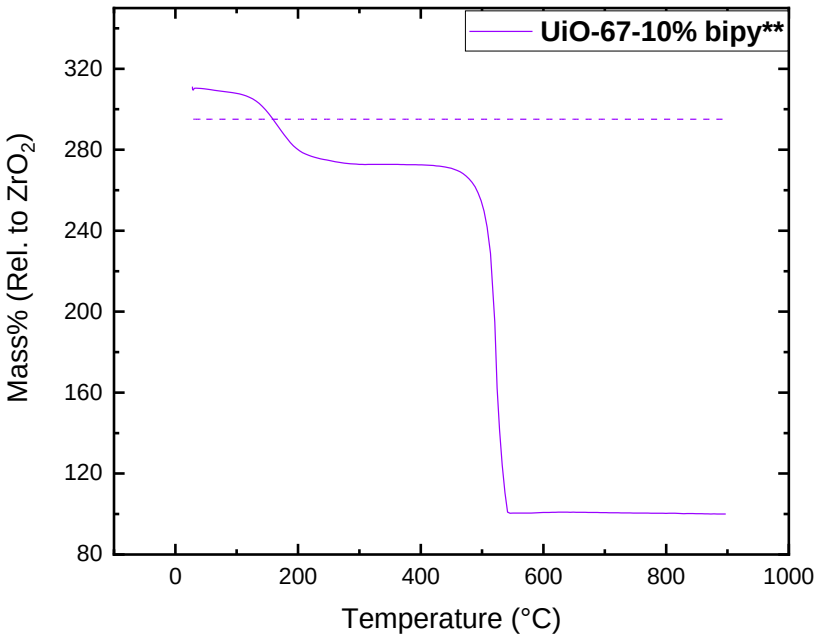

***Figure 4.6**: TGA curves of the UiO-67-10% bipy** sample. The material seems to have 2/3 missing linkers per cluster (one linker is 32.51 mass% relative to ZrO_2).*

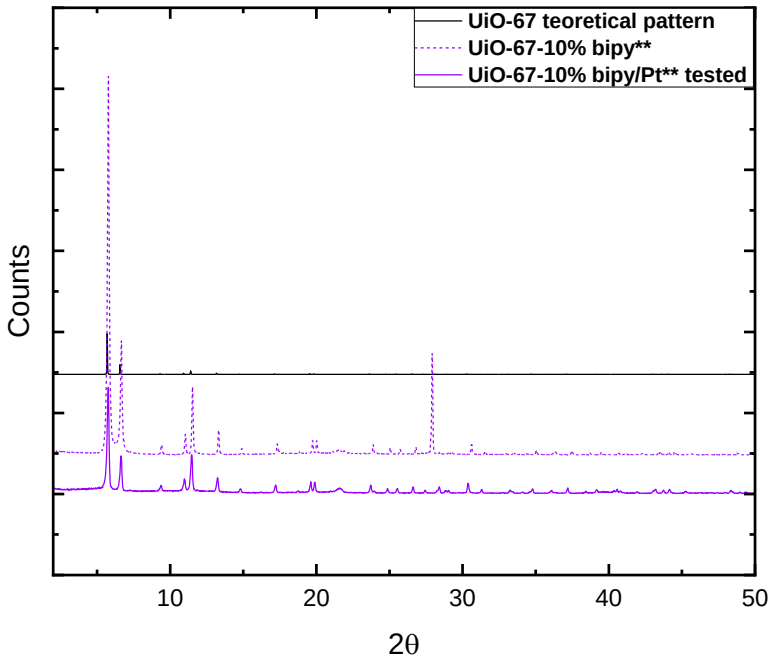

Figure 4.7**: A PXRD diffractogram of the **UiO-67-10% bipy* sample after synthesis.*

Spectra of the species observed can be seen in ***Figure 4.8***, and a plot of the two spectra 330 seconds before and after the switch can be seen in ***Figure 4.9***. The first figure shows the time at which the switch from inert atmosphere to pure oxygen atmosphere takes place. The Ar peak (40 AMU) is the dominating peak until the switch at 512 seconds, when the O_2 peak (32 AMU) starts to take over. A peak at 78 AMU is present with the same intensity before and after the switch and can be linked to aromatic carbons. Carbon dioxide and hydrochloric acid are also present before and after the switch at 36 AMU and 44 AMU, respectively. The original scan was from 0-200 AMU, but only up to 100 AMU is displayed. This is due to no significant change in the mass range above 100 AMU.

Surprisingly, the CO_2 peak does not increase after the switch as opposed to the CO peak, which leads to the conclusion that the organic compounds in the MOF does not full oxidize into CO_2, but only into CO. The peak at 20 AMU is from neon in the argon flow. Some small peaks (close to the detection limit) are seen both before and after the switch at around 50 AMU, but their identity is unknown. The water related peaks (17-19 AMU) also increase slightly when oxygen was introduced, as expected. There was no change in the peaks from the aromatic species (around 78 AMU).

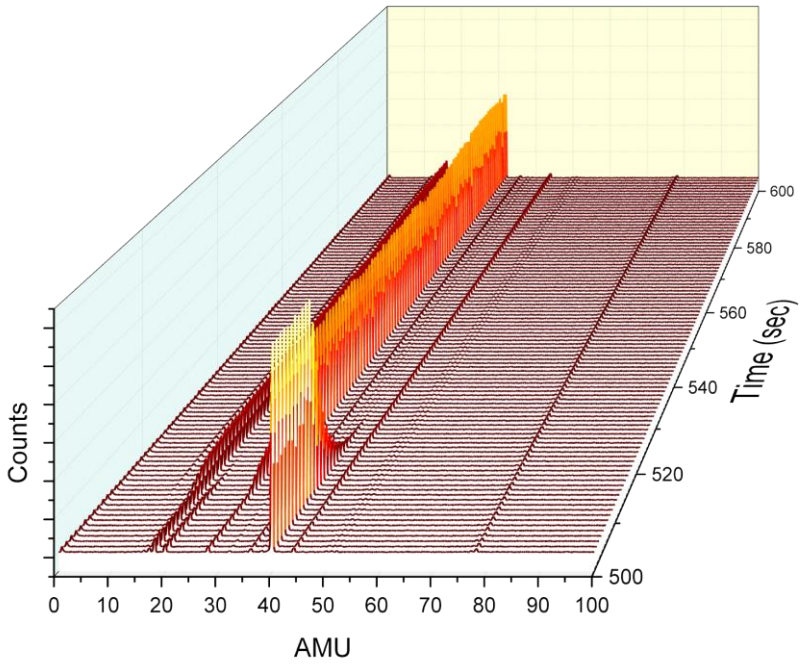

Figure 4.8*: Three dimensional plot of the mass spectrometer data from the TAP experiments. The x-axis is the AMU, the y-axis is the detector counts and the z-axis time in seconds.*

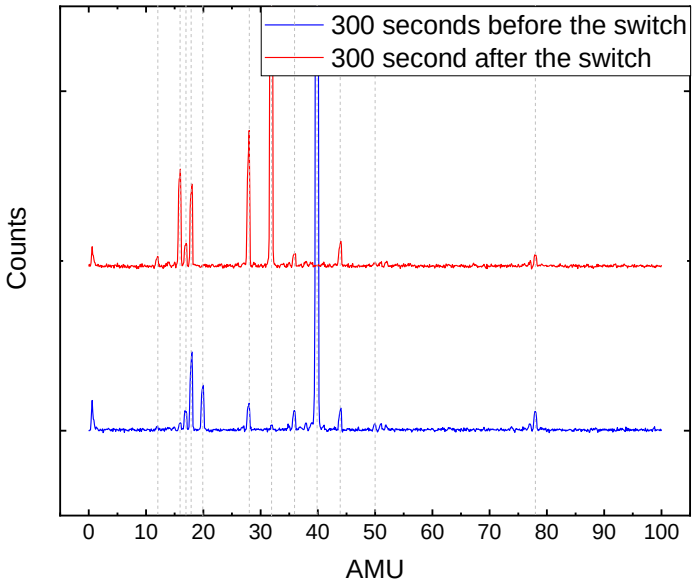

Figure 4.9: Mass spectrum 300 second before and after switch from argon to oxygen in the TAP setup.

Based on the controlled burning in the TGA (***Figure 4.5)***, a small scale *in situ*. oxidation was performed with three different data points; not altered (0 hours in oxygen), 4 hours in oxygen and fully burned (~16 hours in oxygen). The expected amount of defects would be 0 < 4 < 16 hours in oxygen, with the last one to be porous amorphous ZrO_2 with imbedded Pt salt and some (unburned) carbon contamination. The small-scale experiment was done using 140-170 mg sample to see the relative mass loss of the three different burning times.

In order to better be able to compare the samples with the previous investigation in this thesis, reduction of Pt was done the same way (4h in 10% H_2/inert at 40 mL/min). The colour of the samples after the oxygen treatment were tones of grey, going darker as the oxidation time increased. The 16h sample was completely black. After oxidation, the surface area of the sample was measured (***Figure 4.10***). EDS was done to elucidate the Pt/Zr ratio in the samples after the treatment in synthetic air (***Table 4.4***). The wt% of Zr and Pt increase as the time in oxygen increases. This further indicates that the organics burn away leaving ZrO_2 and Pt

Table 4.4: The zirconium and platinum content of the samples after different time of exposure to oxygen at elevated temperatures from EDS, and the Pt/Zr ratio.

Sample	Zr amount (wt%)	Zr σ (wt%)	Pt amount (wt%)	Pt σ (wt%)	Pt/Zr ratio (%)
UiO-67-10% bipy/Pt**	21	0.44	3	0.07	**0.06**
UiO-67-10% bipy/Pt 4h**	26	0.69	4.1	0.13	**0.07**
UiO-67-10% bipy/Pt 16h**	70.5	1.85	8.0	0.22	**0.05**

With increasing time in oxygen atmosphere, the surface area of the samples decreased from 2089 m^2/g to 298 m^2/g. This may indicate that the MOFs loses its structure and/or the pores started to be covered up by either ZrO_2 or platinum. As the samples are being burned, a handle can be seen on the desorption curve. This may suggest that meso-porosity is being created as the samples start to decompose in the oxygen atmosphere. This could also be seen from the diffractograms shown in ***Figure 4.11***.

As the samples burn, peaks at 28, 32 and 42 2θ starts appearing. These peaks may come from the formation of ZrO_2 as the MOF gets destroyed. Comparing the diffractograms to theoretical computed diffractograms for crystallography data, it can be determined that peaks at 30 2θ may come from the formation of cubic or tetragonal zirconia. The reason why both are possible is because it is hard to distinguish the two from PXRD alone. Due to the spread of the peak, it can be argued that the crystallites are very small (*Scherrer equation*). Although some indications of peaks are there, the 16 hour burned sample is mostly amorphous. The tetragonal ZrO_2 was not included due to it being metastable.

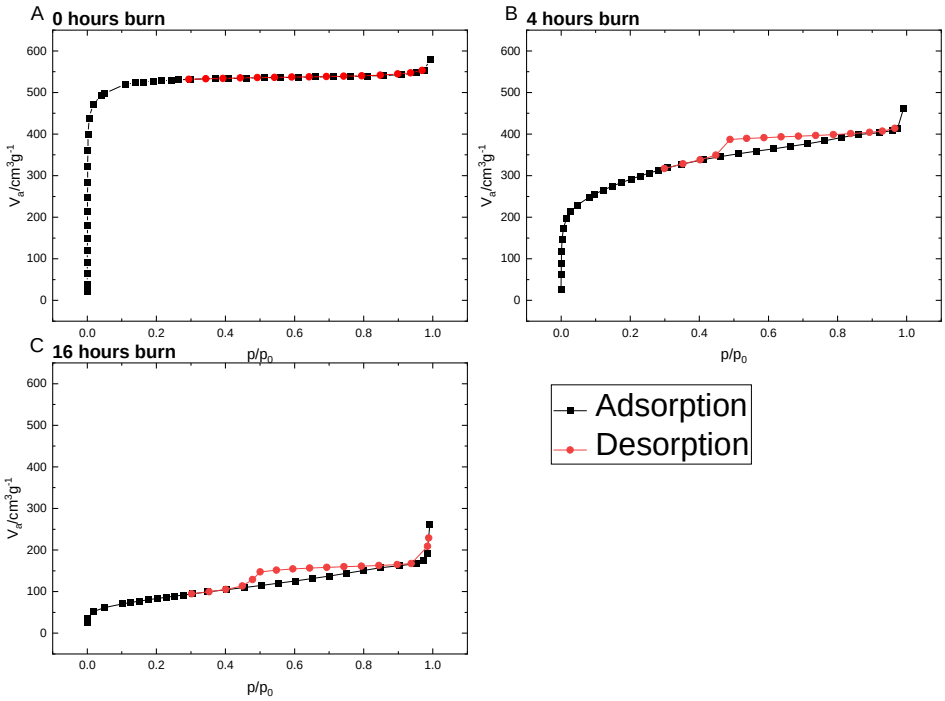

***Figure** 4.10: The N_2 adsorption isotherm of the 3 at 77 K samples after being treated at 350 °C in 1:4 O_2:He 20 mL/min flow; 0h, 4h and 16h (**A, B** and **C,** respectively).*

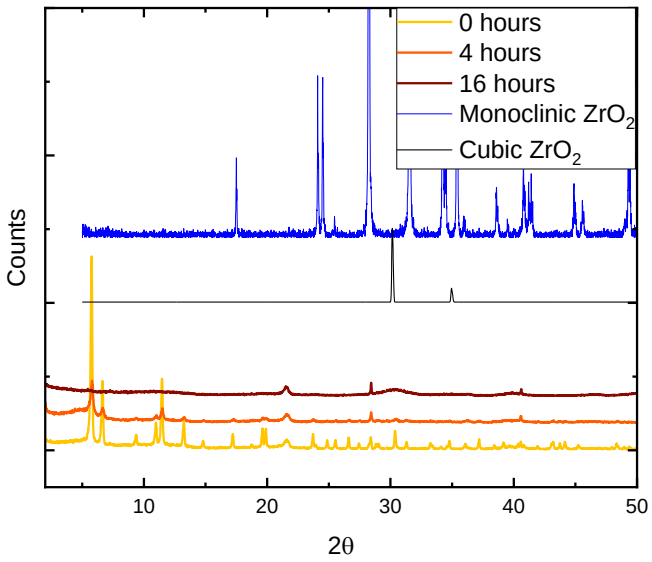

Figure 4.11**: Diffractograms of the **UiO-67-10% bipy/Pt* samples after 0h, 4h, and 16h in 1:4 O_2:He 20 mL/min flow. The black and blue lines are from cubic and monoclinic ZrO_2, respectively. The crystallography data was take from Materials Project. [43, 44]*

4.2 TEM analysis and characterization of the Pt nanoparticles

4.2.1 UiO-66 and UiO-67 samples

UiO-66 and UiO-67 samples, except the **UiO-66-BDC(10% NH_2)/Pt** and **UiO-66-BDC(100% COOH)/Pt**, were found to have a uniform distribution of Pt nanoparticles within the MOF-matrix. This is exemplified in the BF and HAADF STEM images of the **UiO-67-10% bipy/Pt*** sample in ***Figure 4.12***, where the Pt particles are seen as dark and bright, respectively, due to platinum's relative high atomic number compared to the MOF matrix. The lines on the right side of pictures A and B are charging of the MOF particles, which frequently occurred while investigating using TEM/STEM. In pictures C and D the MOF crystallite is viewed down the [110] direction, as indicated by the Fourier transform of the image (**S13**). The diameter of the Pt particles was measured. The corresponding data are summarized in ***Table 4.5.***

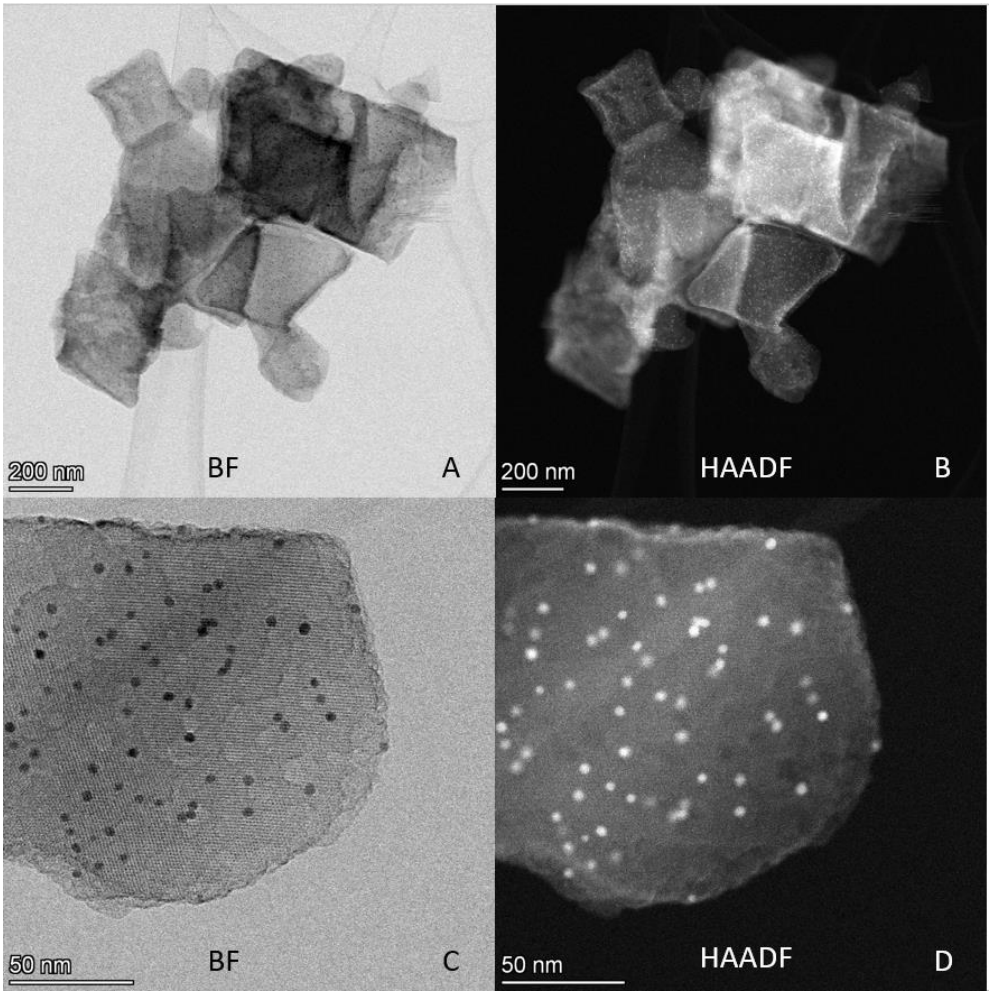

Figure 4.12: *Bright field (BF) and high angular annular dark field (HAADF) STEM images of the* ***UiO-67-10% bipy/Pt**** *after 4 h reduction in 1:9 H_2:Ar and 5 h testing in 1:3:1 CO_2:H_2:Ar(10% Kr). The black (on the BF image) and white (on the HAADF image) specs are the platinum particles.*

More than 500 particles were measured in each sample to ensure statistically significant data. The nano sized Pt particles are found to have uniform size for all of the samples except for the **UiO-66-BDC(10% NH_2/Pt)** sample (***S11)***. In this sample, signs of agglomerated particles with a diameter larger than 10 nm were observed.

Interesting to note, is that the two **UiO-67-10% bipy/Pt** samples have a substantial large difference in mean nanoparticle size, even though they should be the same material. Similarly, the **UiO-67-10% bipy/Pt (H)** seem to have larger particles than the parent **UiO-67-10% bipy/Pt***. The **UiO-67-BN(10% bipy/Pt)** sample have the smallest nanoparticles of the UiO-67 systems, while the **UiO-66-BDC(100% NH_2)/Pt** sample have the smallest of the UiO-66 systems.

Table 4.5: The statistics of the platinum nanoparticle sizes.

Name of the samples	Mean particle size (nm)	σ (nm)	Particles counted
UiO-67-10% bipy/Pt	4.23	1.13	707
UiO-67-10% bipy/Pt* (H)	4.02	1.02	1487
UiO-67-10% bipy/Pt*	3.74	1.05	1460
UiO-67-BN(10% bipy/Pt)	3.14	1.63	677
UiO-67-100% bipy/Pt	4.29	1.13	786
UiO-66-BDC(100% NH_2)/Pt	2.7	0.49	536
UiO-66-BDC(100% COOH)/Pt	N/A**	N/A**	N/A**
UiO-66-BDC(10% NH_2/Pt)	10.12	7.06	40*

*Distribution plots can be seen in figures **S5-S9**. *only 40 particles counted due to large (>>10 nm) particles (**S10**). ** The **UiO-66-BDC(COOH)/Pt** sample seem to have a coating of Pt around the MOF crystallites(**S11**), so counting was not attempted.*

When decreasing the bin size of the columns in the histograms, distinct sizes stood out and created holes in the distribution (**S5-S9**). This may indicate "magic numbers" for the platinum particles indicating stable clusters of platinum atoms e.g., nanoparticles.

TEM was also used to see if there were any indications of the growth-relationship between the MOF and the Pt nanoparticles. Since platinum is in the face centred cubic crystal system, the preferred shape is to form octahedral crystals. The [111] direction is the slowest growing face of such crystals, and the [111] surface should therefore be the dominating face.

When looking at STEM and TEM micrographs in ***Figure 4.13***, the particles were shown to not be spherical but rather hexagonal 2D representations of an octahedral crystal. This indicate that

the platinum nanoparticles grow into their preferred shape inside the MOF, and that the MOF does not afflict any change in their crystal growth.

The spherical/rounded appearance of the particles was attempted explained by simulating a 3 nm platinum nanoparticle inside a MOF-matrix and compared to real images (***Figure 4.14***). The simulated MOF is viewed along the [111] direction of the MOF, with the particle being viewed along the [123] direction and with a nanoparticle size of 3 nm. The orientation of the platinum particle was chosen at random. When the particle is inside the MOF, the faceted edges of the particle becomes less visible, and can therefore be perceived as a round, spherical particle. An explanation of this is that particles in thicker areas and at lower magnification looks round due to the loss of detail as the contrast decreases. This phenomenon disappeared when the magnification of the instrument increased, and when the contrast of the images improved, as seen on ***Figure 3.13***. The appearance of elongated particles could be explained by two particles either being agglomerated into one particle, or two particles situated closely to each other, but at different height, appearing as one mis-shaped particle when viewed in 2D.

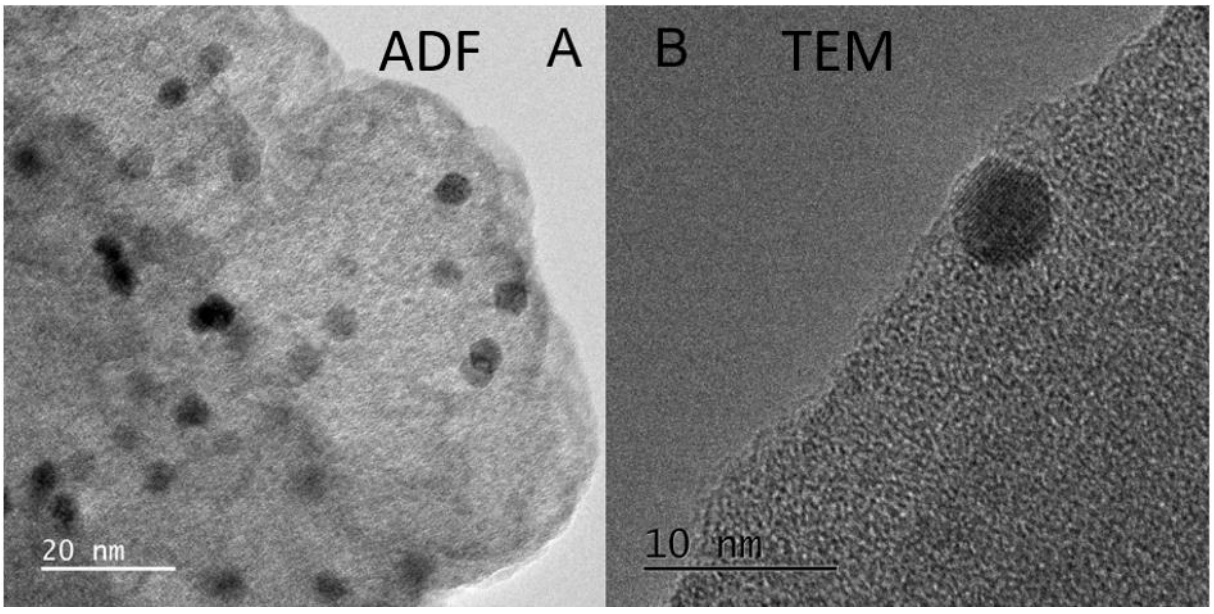

Figure 4.13: *TEM micrograph images showing the high magnification images (**A, STEM**) of the **UiO-67-10% bipy/Pt (H)** and (**B, TEM**) of the **UiO-66-BDC(100% NH_2/Pt)** sample.*

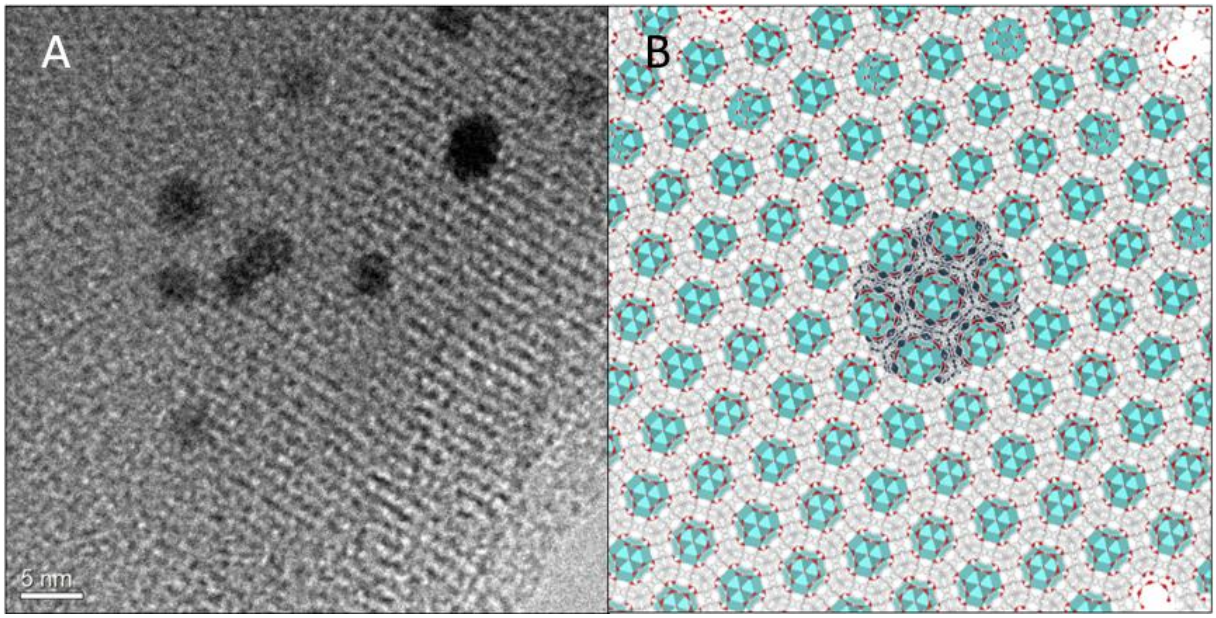

Figure 4.14: *Micrograph of (**A**) of the **UiO-67-10% bipy/P** and (**B**) a model of UiO-67 with an imbedded nanoparticle. The cyan polyhedra with the red corners represent the Zr_6O_8 clusters (oxygen is red) of the MOF. The linkers are depicted as light gray bonds. The platinum nano particle is represented by the darker blue color for contrast and better visualization.*

It was hypothesized that if the particle was to grow out of the MOF it would be expected for them to be in zone axis at the same time, as well as have the same directionality of the fringes when in zone axis. This was because both the MOF and the particles prefer the face centered cubic crystal system. Due to the unstable nature of the frameworks themselves, finding an area where the particle and the MOF were in zone axis, proved difficult. STEM was used to capture an image with both in zone axis.

As shown in the TEM image in ***Figure 4.15***, the platinum nanoparticles do not have the same direction as the MOF. This further supports that the nanoparticles does not grow "out" of the, but rather grow freely inside the MOF, which further may explain why they grow into perfect crystals. The other platinum particles in the images are not in zone axis, which would be expected if their growth were influenced by the MOF. In the few instances that two nanoparticles were in zone axis at the same time, their fringes were not in the same direction. As can be seen in **Figure 4.16,** the two Fourier transformed images are not in the same direction, further indicating that growth direction and orientation of the platinum particles are random.

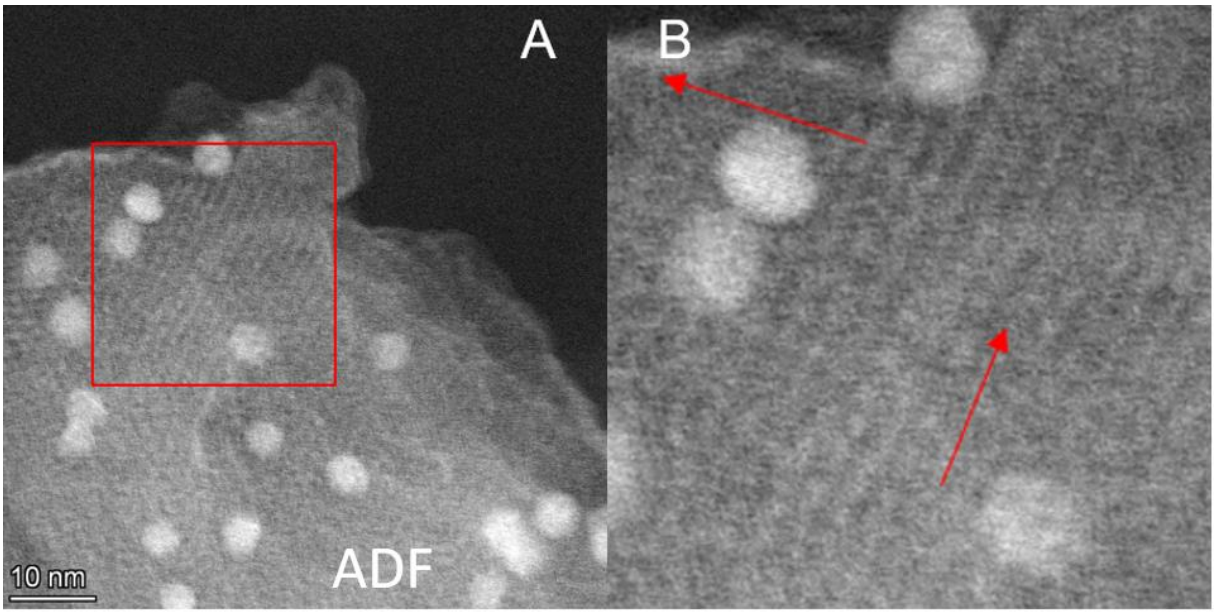

Figure 4.15: *The left image (**A**) is a STEM image showing a high magnification image of the **UiO-67-10% bipy/Pt (H)**. The right picture (**B**) is a post-processing zoom to better show the fringes of the nanoparticle. The red box in image **A** indicates the area that is zoomed in and the red arrows in image **B** indicate the direction of the fringes.*

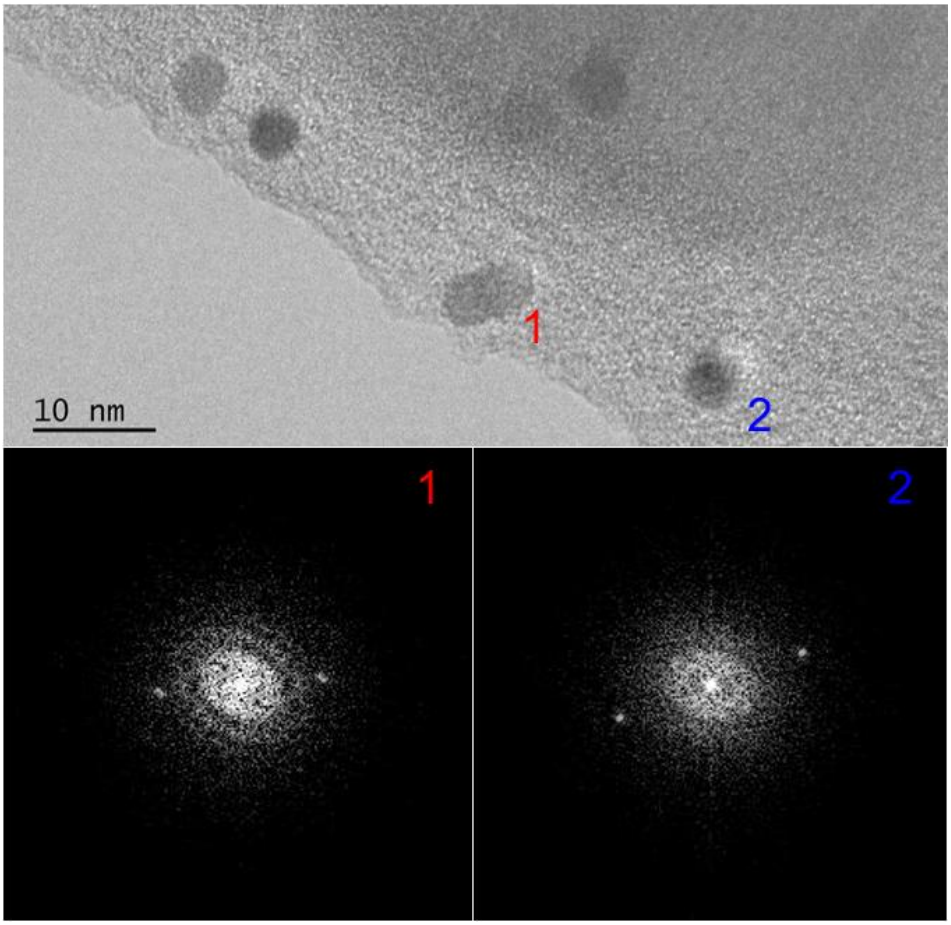

Figure 4.16: *TEM images and Fourier transforms of the **UiO-67-10% bipy/Pt (H)** sample.*

STEM investigations revealed that the particles tend to be on and/or close to the surface of the MOF crystals, as seen in ***Figure 4.17***. Although this is the case, the nanoparticles seem to stay well dispersed in the material. As is know from literature, the salt will graft to the bipy-linkers in the post synthetic metalation of the MOFs.[34] If the functional linker is well dispersed, the impregnation of platinum can be assumed to be well dispersed as well. If the functional linker has only been incorporated close to the outer layer of MOF, the platinum will only be situated where the functional linker is situated. It is also a factor of how long the impregnation procedure takes for the platinum salt to diffuse into the MOF network.

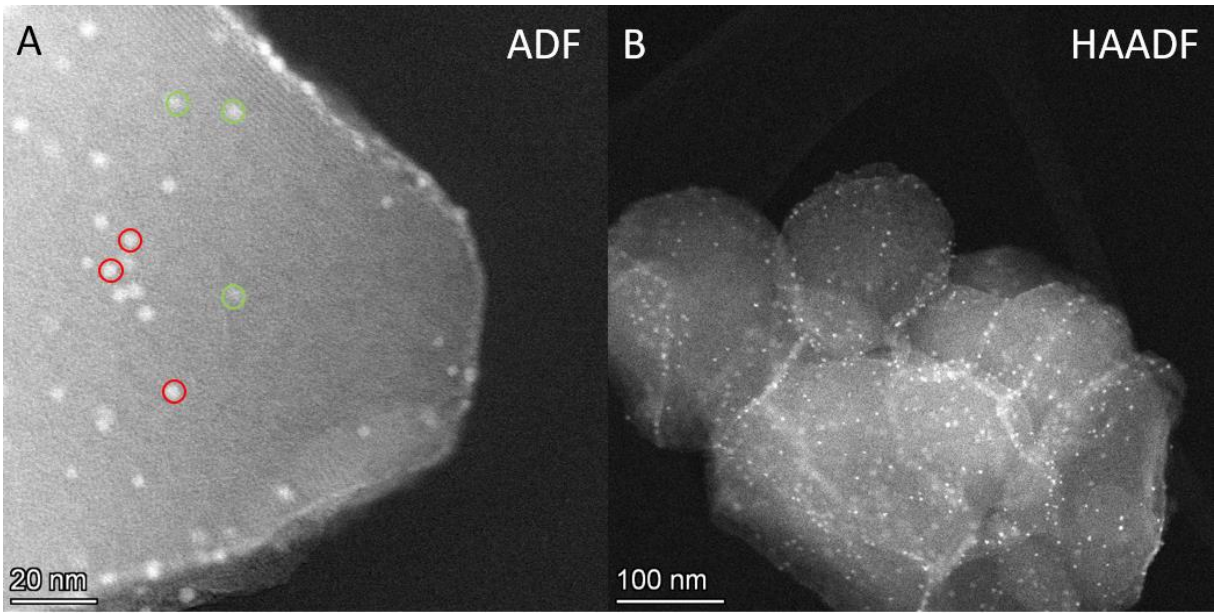

Figure 4.17: *ADF and HAADF STEM high magnification images of the* ***UiO-67-10% bipy/Pt (H)****.* ***A*** *is of one of the corners of the octahedral MOF crystal. The red and green circles on image* ***A*** *show the different particles that are in the same plane of focus.* ***B*** *depicts agglomerated MOF particles, where the density of Pt nanoparticles is highest close to the edges and between the MOF crystallites.*

ADF and HAADF STEM images also revealed that the MOF crystallites are meso-porous with cavities with 1-4 nm in diameter inside the MOF structure, as can be observed in ***Figure 4.18***. Even though there are many pores where the platinum can agglomerate, it has stayed dispersed in the material. The pores are observed as the darker spots in the MOF crystallites.

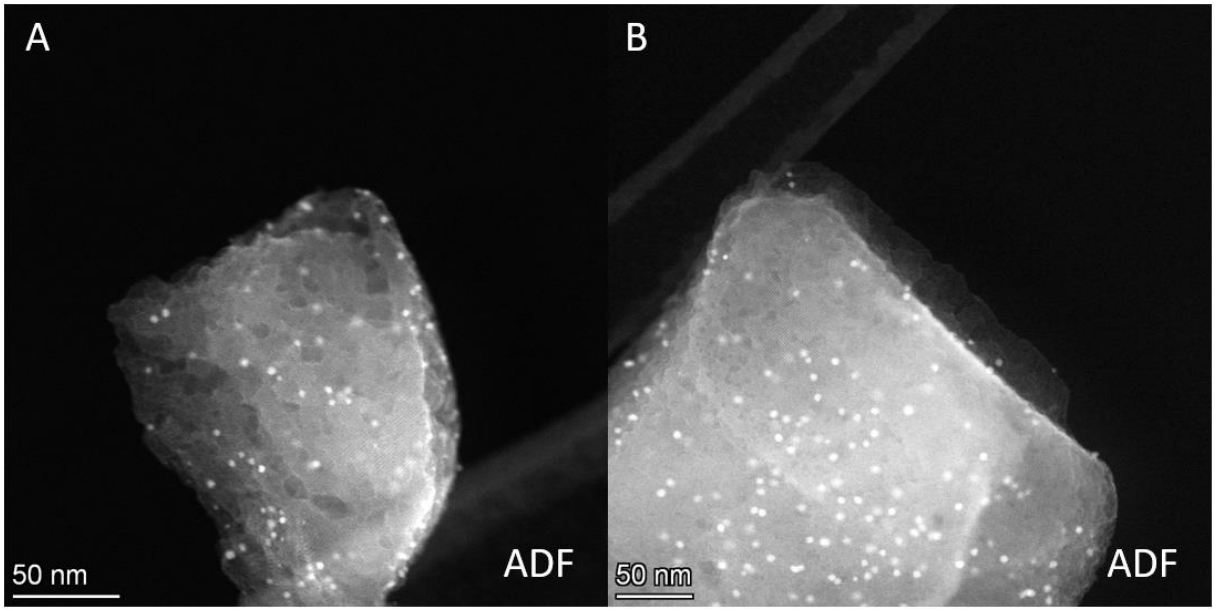

Figure 4.18: *STEM images showing the high magnification images of (**A**) **UiO-67-10% bipy/Pt*** and of (**B**) **UiO-67-10% bipy/Pt (H)**. The pores can be seen as the darker spots on both image **A** and **B**.*

Where the platinum nano particles larger than the octahedral holes in the pores of the MOF grow, has been a question for a long time; do they grow in existing holes or do they create their own holes, destroying some of the surrounding MOF in the process? Based on the number of pores without any particles in them as seen on ***Figure 4.18***, it is indicated that the particles may create their own holes in the growing process. To further investigate this question, tomography measurements are needed.

For the **UiO-66-BDC(COOH)/Pt** sample, no apparent grafting site for the Pt may be the reasons why the material ended up getting a platinum "coating" on the outside and not on the inside of the MOF. A similar platinum impregnation method was used for this sample as the rest, although an incipient wetness impregnation method might have been a more efficient way to ensure a satisfactory diffusion of $K_2Pt(II)Cl_4$ into the framework.

When looking at the **UiO-67-10% bipy/Pt*** and the **UiO-67-10% bipy/Pt* (H)** samples it was expected that the healed sample would have the smallest nanoparticle size. This is the opposite of what is observed from TEM images. The **UiO-67-10% bipy/Pt***sample has the same Pt nanoparticle size as reported earlier by Gutterød *et al.*.[1]

The gray and dark navy blue colour of the **UiO-66-BDC(10% NH_2/Pt)** and the **UiO-66-BDC(COOH)/Pt** samples (section **4.1.1**) prior to testing, coincide well with the appearance of large or undefineble Pt nanoparticles found in TEM. The samples may have been reduced before being tested, which gave them the gray influence in the colour of the bulk material. This may

also explain why the nanoparticles found in these samples seem to only be located on the outer surface (as seen in **S8-S9**).

Based on the analysis from TEM the active sites for the catalysts were calculated. This was done by assuming that the active catalytic sites were the platinum atoms on the surface of the nanoparticles. The number of active sites for each of the samples can be seen in ***Table 4.6.***

Table 4.6: The number of moles of surface Pt sites per gram of catalyst and the number of Pt atoms. This is based on nanoparticle size measured in TEM and wt% from EDS. The far right column is the number of Pt particles per gram catalyst. Calculation is shown in section 2.5.5.1.

Sample	Number of active sites (mol/g_{cat})	Number of particles per gram catalyst
UiO-67-10% bipy/Pt	$1.22 \cdot 10^{-5}$	$1.21 \cdot 10^{16}$
UiO-67-10% bipy/Pt* (H)	$2.70 \cdot 10^{-5}$	$1.52 \cdot 10^{16}$
UiO-67-10% bipy/Pt*	$4.21 \cdot 10^{-5}$	$3.25 \cdot 10^{16}$
UiO-67-BN(10% bipy/Pt)	$1.07 \cdot 10^{-5}$	$1.98 \cdot 10^{16}$
UiO-67-100% bipy/Pt	$4.15 \cdot 10^{-5}$	$4.07 \cdot 10^{16}$
UiO-66-BDC(100% NH_2)/Pt	$1.04 \cdot 10^{-4}$	$2.64 \cdot 10^{17}$
UiO-66-BDC(100% COOH)/Pt	N/A*	N/A
UiO-66-BDC(10% NH_2/Pt)	$2.56 \cdot 10^{-5}$	$4.58 \cdot 10^{16}$

*The formula used to calculate this is shown in section **7.1**. *since there were no clear nanoparticles for the **UiO-66-BDC(100% COOH)/Pt**, no calculation was done (**S11**).*

4.2.2 Different platinum loadings in UiO-67-10% bipy/Pt*

The **UiO-67-10% bipy/less Pt**, **UiO-67-10% bipy/Pt*** and **UiO-67-10% bipy/ex Pt** samples have quite similar Pt nanoparticle size although the metal loading was different (as seen in **Figure 4.20** and **Table 4.7**). The difference in height of the column is due to the number of particles in each data set. All samples had 700 or more particles counted. The small difference in particle size may indicate that the Platinum particles prefer a size regardless of the platinum loading amount, indicating that the MOF do have some constraints on the particle size. The amount of platinum on the surface of the nanoparticles and the number of particles in the sample were calculated and can be seen in ***Table 4.8***. The nanoparticle distribution went from **UiO-67-10% bipy/less Pt** sample with very few particles, to **UiO-10% bipy/ex Pt** sample which had more particles.

Table 4.7: The mean platinum particle size and the standard deviation of the samples UiO-67-10% bipy/Pt*, UiO-67-10% bipy/ex Pt and UiO-67-10% bipy/less Pt.

Sample	Pt Nano particle size (nm)	σ (nm)
UiO-67-10% bipy/less Pt	3.5	0.964
UiO-67-10% bipy/Pt*	3.7	1.05
UiO-67-10% bipy/ex Pt	4.0	0.955

The samples seem to have the same particle sizes between 3.5 and 4 nm in diameter, increasing from the sample with least platinum content, to the sample with the most platinum content.

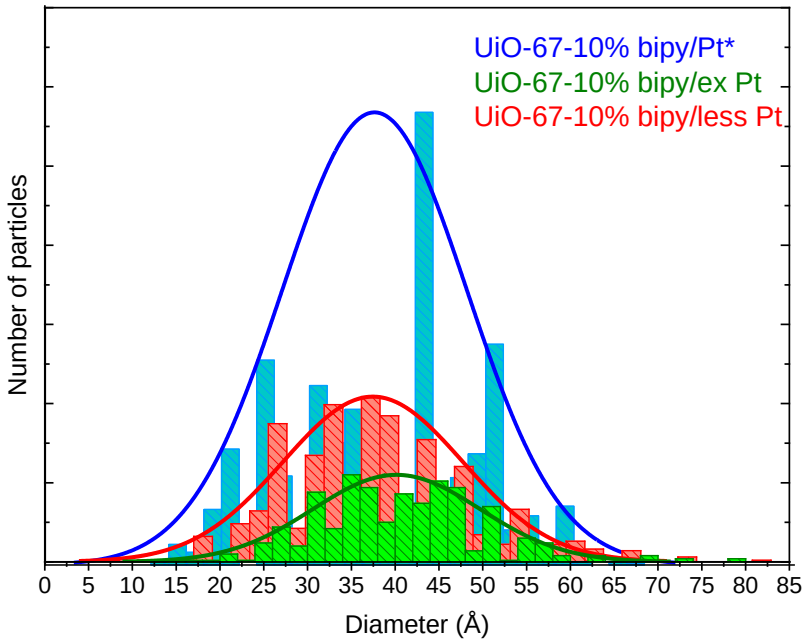

Figure 4.20: *Histograms showing the size distribution of the three samples with different platinum loading; UiO-67-10% bipy/Pt* (blue), UiO-67-10% bipy/ex Pt (green) and UiO-67-10% bipy/less Pt (red).*

Table 4.8: The number of moles of platinum atoms on the surface of the nanoparticles. The right column is the number of Pt nanoparticles per gram catalyst. This was calculated using nanoparticle size from TEM and composition from EDS.

Sample	Pt on the surface (mol/g_{cat})	Number of particle per gram catalyst
UiO-67-10% bipy/less Pt	$3.8 \cdot 10^{-6}$	$5.49 \cdot 10^{-15}$
UiO-67-10% bipy/Pt*	$4.2 \cdot 10^{-5}$	$3.25 \cdot 10^{-16}$
UiO-67-10% bipy/ex Pt	$4.6 \cdot 10^{-5}$	$5.15 \cdot 10^{-16}$

4.2.3 Defects in UiO-67-10% bipy/Pt** induced by oxygen calcination

After the small batch samples had been subjected to the oxidation step, the samples were investigated in TEM. As suggested by adsorption measurements, the structural integrity of the framework collapsed the longer the material was exposed to oxygen at elevated temperatures. This can be seen on the TEM micrographs in ***Figure 4.22***. The amount of platinum on the surface was calculated based on particle size from TEM and wt% platinum from EDS and can be seen in ***Table 4.9***.

Although the smooth edges of the framework crystallites started to roughen up as the materials were oxidized, the overall size of the crystallites did not appear to change as much. The rapid decrease in surface area, as shown by adsorption experiments, indicated that the material would shrink and fully collapse after a significant time subjected to an oxidative atmosphere. TEM data reveal that some structure is lost, but that the loss of surface area my come from coating of the outside of the MOF (as seen on the micrographs of the 16h sample). It is presumed that it is ZrO_2 that is being formed in bulk and closes off the pores of the framework. Due to the similarities of the peaks in Zr and Pt in EDS, this proved hard to investigate. Statistical analysis of the TEM micrographs show that the nanoparticles increase in size as the structures are collapsing, from 3.6 nm to 5.4 nm in diameter (***Figure 4.21***). Due to the design of the experiment, all the samples were presumed to have 3.6 nm platinum particles before the oxidation, and the particles grew as the framework around started to collapse. The difference in height of the three distribution curves is due to the size of the different datasets.

Table 4.9. The number of moles of platinum on the surface of the nanoparticles per gram catalyst. This was calculated from nanoparticle size from TEM and composition form EDS

Sample	Pt on the surface (mol/g_{cat})
UiO-67-10% bipy 0h	$3.5 \cdot 10^{-5}$
UiO-67-10% bipy 4h	$4.2 \cdot 10^{-5}$
UiO-67-10% bipy 16h	$7.6 \cdot 10^{-6}$

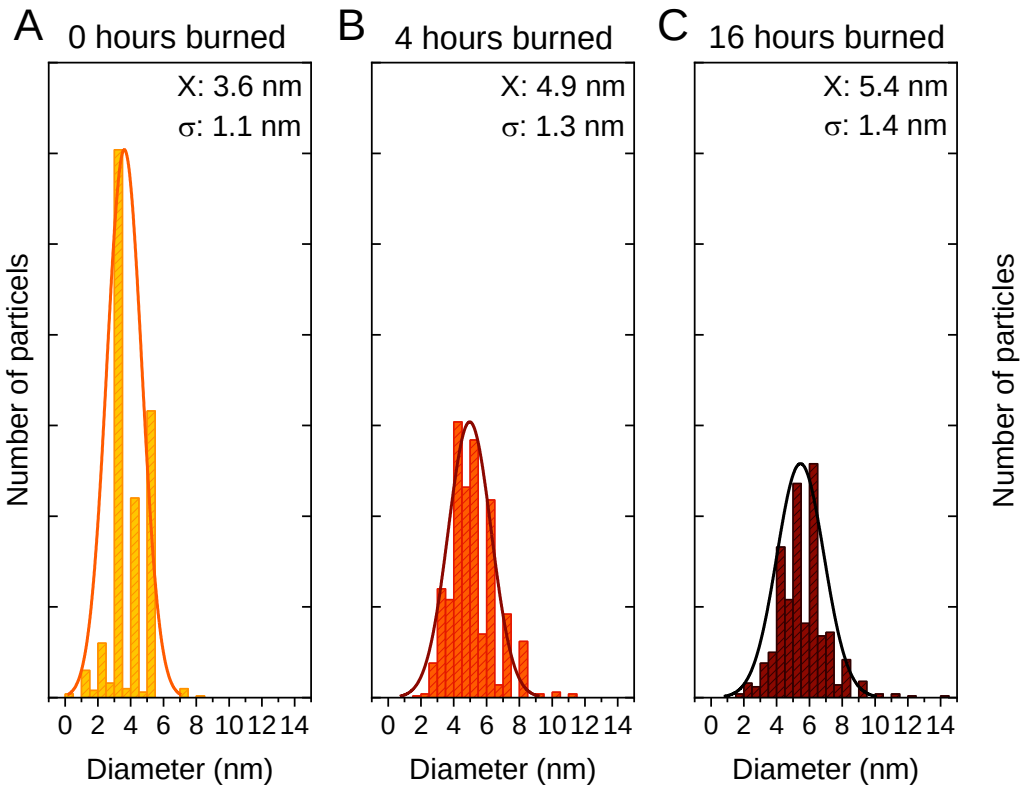

Figure 4.21: *The Pt nanoparticle size distribution curves for the three samples: 0 hours (**A**), 4 hours (**B**) and 16 hours (**C**). X is the mean particle size and σ is the standard deviation.*

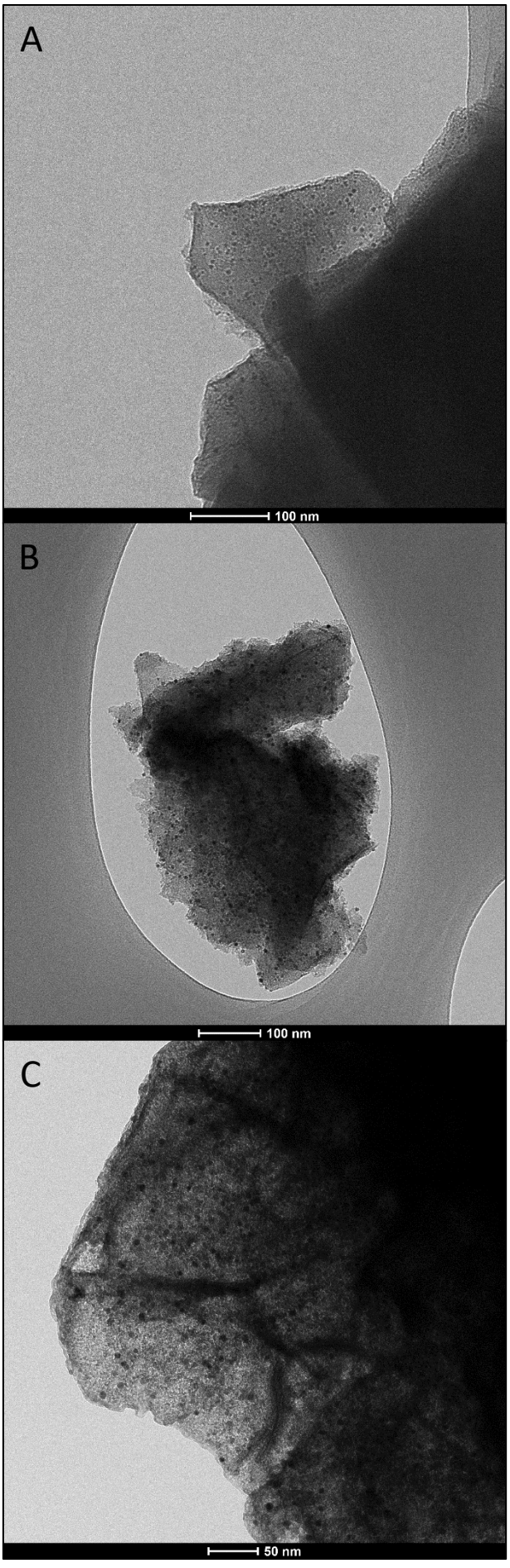
A
100 nm
B
100 nm
C
50 nm

*Figure 4.22: TEM micrographs of the three samples after 0h (**A**), 4h (**B**) and 16h (**C**) in oxidation conditions. Nanoparticles were observed in all the samples. These micrographs were taken at, and in collaboration with the Utrecht University.*

4.3 Catalytic activity

4.3.1 UiO-66 systems

The samples were activated at 200 °C for 4 hours in 1/9 H_2/Ar atmosphere before being ramped down to 170 °C in a 1/3/1 CO_2/H_2/Ar(10% Kr) atmosphere, as described in the experimental chapter (section **3.2.2**). Due to the manual stabilization in pressure, the first two data points may not be correct. A 28 hour run illustrates that the catalysts show no signs of deactivation, as seen on ***S1***. Reproducibility tests were also conducted and can be seen in ***S2***. It shows good reproducibility with an uncertainty of 0.1% on average. The CO_2 conversion of the samples is shown in the graphs in ***Figure 4.23***.

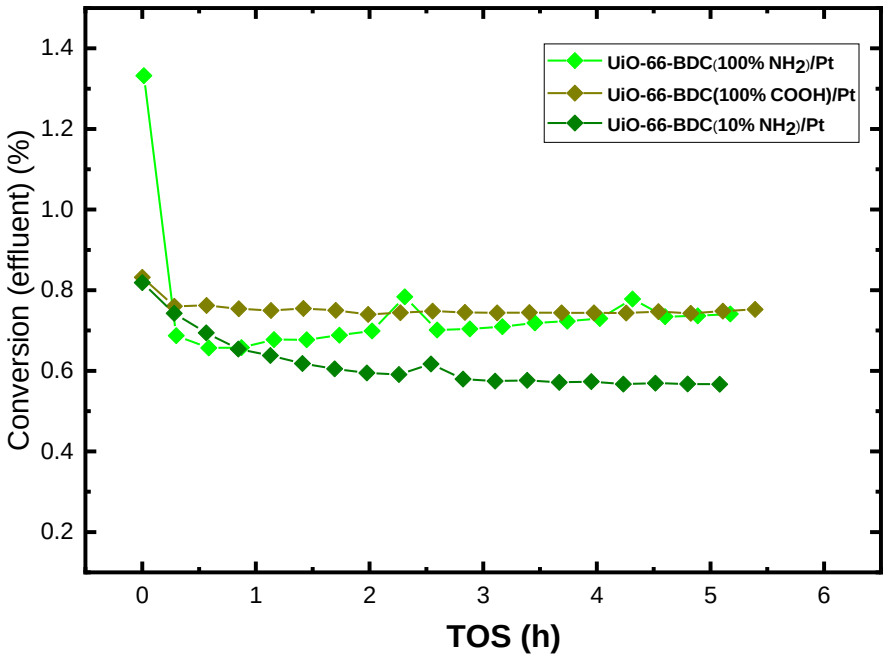

Figure 4.23: The CO_2 conversion as a function of time of the UiO-66 samples. The samples were tested at 170 °C in a 1:3:1 CO_2:H_2:Ar(10% kr) 20 mL/min flow.

The samples show low, but reproducible conversion. The two samples with only functionalized linkers, **UiO-66-BDC(100%NH_2)/Pt** and **UiO-66-BDC(100% COOH)/Pt**, give a conversion of 0.8%, while the **UiO-66-BDC(10% NH_2)/Pt** give a conversion of 0.6%. The **UiO-66-BDC(100%**

COOH)/Pt is the only sample that is stable at steady-state. The **UiO-66-BDC(100% NH_2)/Pt** show a slight increase over time, and the **UiO-66-BDC(10% NH_2)/Pt** sample show a slight decrease. The selectivity can be seen in **Figure 4.22**.

The selectivity towards methanol for all samples range from 20% to 2.5% at steady-state with the **UiO-66-BDC(100% NH_2)/Pt** sample having the highest selectivity. All samples reach steady-state with an increase, and similar decrease, in methanol selectivity and carbon monoxide selectivity, respectively, except the **UiO-66-BDC(10% NH_2)/Pt** which show an inverse trend. The **UiO-66-BDC(100% NH_2)/Pt** and the **UiO-66-BDC(10% NH_2)/Pt** show a large difference in selectivity, being more selective to methanol and carbon monoxide, respectively. This may be due to the large difference in Pt nanoparticle size (3 nm vs. 10 nm in average, see ***Table 4.5***). The higher methanol selectivity of the **UiO-66-BDC(100% NH_2)/Pt** sample may suggest a larger interface between the Pt nanoparticle and the Zr-nodes in this catalyst.

The rate of formation was calculated based on carbon dioxide flow and GC signal of the effluent from the reactor as can be seen in ***Figure 4.23***. The **UiO-66-BDC(100% NH_2)/Pt** showed the highest methanol formation rate, ending with a rate of 0.6 mol kg^{-1} h^{-1}, corresponding to a effluent yield of 0.14%. All the samples show ten times lower MeOH rates compared to CO rates, and even though the **UiO-66-BDC(100% COOH)/Pt** sample have quite different Pt morphology, having a Pt coating and not nanoparticles like the two samples, it shows similar formation rates.

The estimated amount of active sites per gram catalyst, as calculated in section **4.2.1**, was used to calculate the turnover frequency for all samples (***Figure 4.24***). The turnover frequency is greatly influenced by the nanoparticle size. The larger the particles, the less percentage of the atoms in the particle have access to the surface; finite size effect. The **UiO-66-BDC(10% NH_2)/Pt** sample has a higher TOF towards both CO and MeOH, with CO reaching 0.0029 mol s^{-1} mol^{-1} at steady-state and MeOH reaching 0.0001 mol s^{-1} mol^{-1}. Both BDC(NH_2) samples have a higher TOF towards CO.

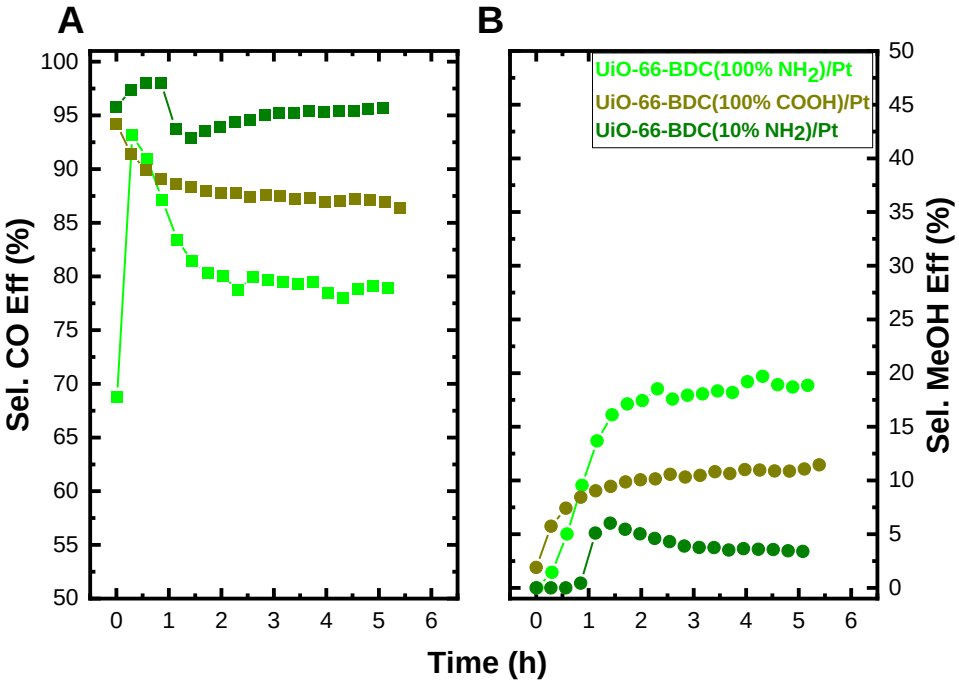

Figure 4.22: *The selectivity towards carbon monoxide and methanol for the UiO-66 samples as a function of time. The plots on the graph to the left (**A**) is the carbon monoxide effluent selectivity while the plots on the graph to the right (**B**) is the methanol effluent selectivity.*

The MeOH TOF is very similar for the two NH_2-samples, but the CO TOF is very different. The high turnover frequency of CO for the **UiO-66-BDC(10% NH_2)/Pt** sample may come from having a larger platinum surface area where the CO_2 and H_2 can dissociate into CO and H_2O, thus increasing the rate at which CO is formed. The Turnover frequency of the **UiO-66-BDC(100% COOH)/Pt** was not included due to not having definable nanoparticles.

Overall, the performance of these three samples may be allocated the difference in the platinum distribution and particle size. The samples have vastly different platinum nanoparticle sizes and this can be linked to the difference in catalytic activity. It is hard to say if the various functionalization of the framework in the samples had any effect on the catalytic activity due to the difference in the platinum species. What can be said is that the linkers in the framework influence the platinum reduction and particle growth, as stated in the previous section (**4.2.1**).

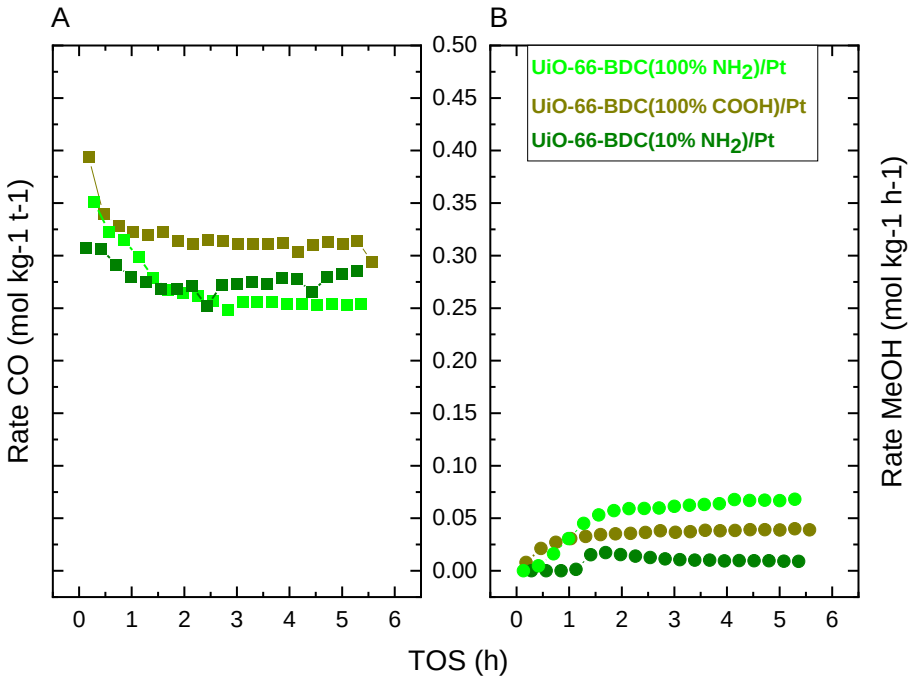

Figure 4.23: *The rate of formation of carbon monoxide and methanol for the UiO-66 samples as a function of time on stream. Carbon monoxide rates to the left (**A**) and the methanol rates to the right (**B**). The y-axes are the same for both graphs.*

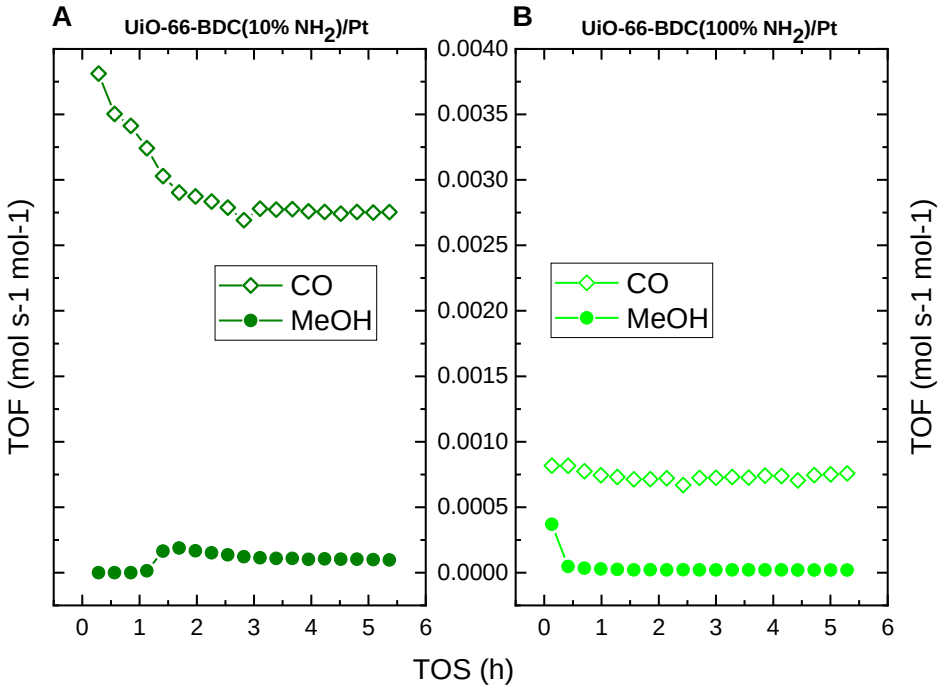

Figure 4.24: *The turnover frequency towards CO and MeOH for the **UiO-66-BDC(10% NH₂)/Pt** (**A**) and **UiO-66-BDC(100% NH₂)/Pt** (**B**). Only the two samples with the amine group are represented here due to the lack of countable nanoparticles for the **UiO-66-BDC(100% COOH)/Pt** sample. **A** and **B** share the same y-axis.*

A difference between the three samples that can influence the reaction is the acidity of the different functional sites. The COOH group is an acid while the NH_2 group is a base. This may influence the way hydrogen is being transported throughout the system, since hydrogen will attract more to the amine group. This is of course if the hydrogens in the linkers contribute to the reaction, not just the chemisorbed hydrogen on the Pt particles going directly to the open sites at the Zr-nodes. Since the **UiO-66-BDC(100% COOH)/Pt** show quite similar selectivity and formation rates as the two other samples it can be argued that the linker play a minimal role on the reactions.

4.3.2 UiO-67 systems

The samples were activated at 350 °C for 4 hours in a 1/9 H_2/Ar atmosphere before being ramped down to 170 °C in a 1/3/1 CO_2/H_2/Ar(10% Kr) atmosphere, as described in the experimental chapter (section **3.2.2**). The CO_2 conversion of the samples is shown in the graphs in ***Figure 4.25***.

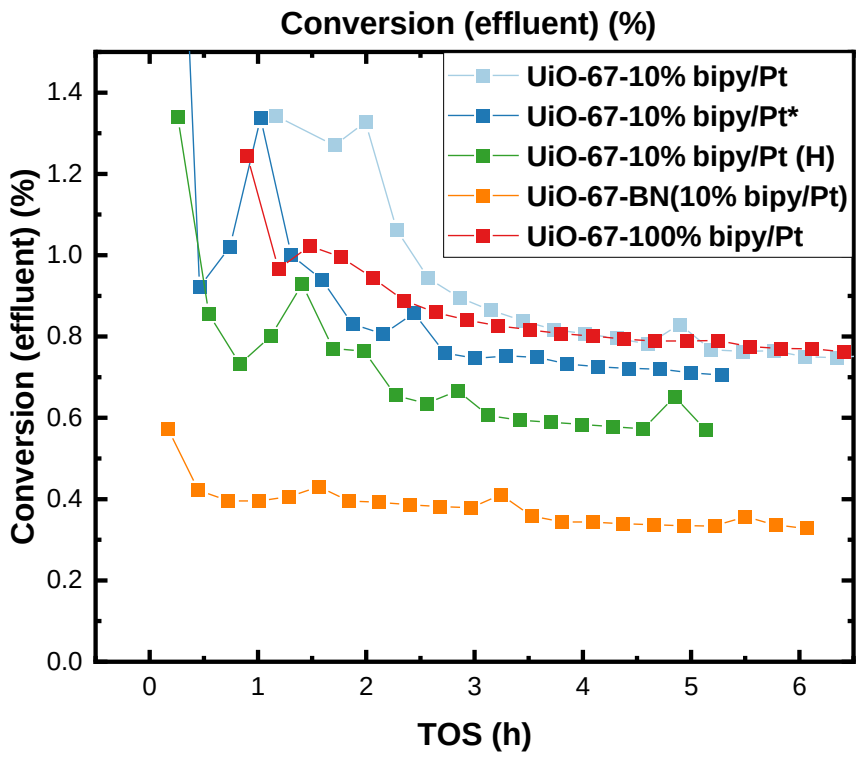

Figure 4.25: *The CO_2 conversion as a function of time on stream of the UiO-67 samples . The two first data points have the largest amount of uncertainty due to the manual increase in pressure. The samples were tested at 170 °C in a 1:3:1 CO_2:H_2:Ar(10% Kr) 20 mL/min flow.*

All samples take a while to reach steady-state, having a large decrease in the first few measurements. Except for the **UiO-67-BN(10% bipy)/Pt**, all of the samples reach a conversion between 0.5 to 0.8%. Concerning selectivity, only carbon monoxide and methanol will be investigated here. Both methane and other lower carbon species are also present, but they account for less than 1% of product selectivity, and are considered negligible. CO is the main product over all materials.

The selectivity, as seen in ***Figure 4.26***, towards methanol starts off with a peak for all of the samples, except the **UiO-67-BN(10% bipy)/Pt** sample, which has only a slight peak. The MeOH selectivity drops down after about two hours. This behavior was not observed for the UiO-66 samples. This peak is also present for the carbon monoxide selectivity, but with a negative peak. The selectivity feature in methanol is twice as high as the selectivity at steady-state. The slope of the peaks as they go towards steady-state seems to have similar shapes, indicating that they are caused by the same phenomenon.

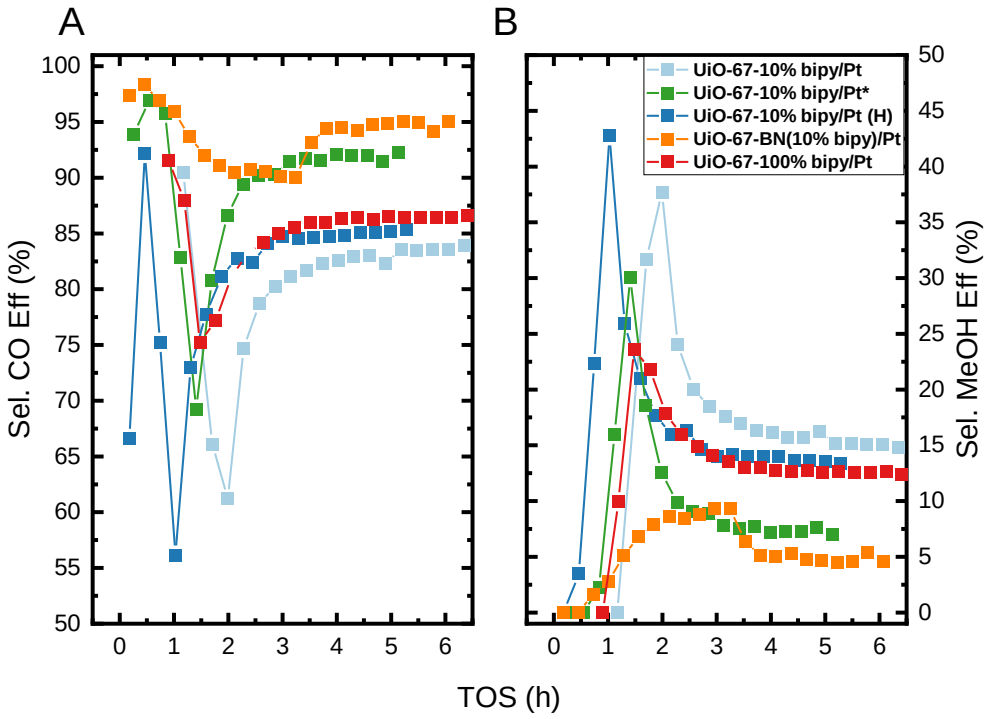

Figure 4.26: *The selectivity towards carbon monoxide and methanol for the UiO-67 samples as a function of time. The plots on the graph to the left (**A**) is the carbon monoxide effluent selectivity while the plots on the graph to the right (**B**) is the methanol effluent selectivity.*

By looking at the rate of formation of the two species (***Figure 4.27)***, the cause of the peaks in methanol and carbon monoxide selectivity can be linked. The peak is not present for the carbon monoxide rate, while it is present for the methanol rate. The presence of this peak in methanol formation suggests that the methanol formation is inhibited after a while. All three of the UiO-67-bipy samples show similar rates, while the **UiO-67-BN(10% bipy)/Pt** sample show both lower carbon monoxide and methanol formation rates. The UiO-67 sample with the highest methanol rate is the **UiO-67-10% bipy/Pt**, with a rate of 0.6 mol kg^{-1} t^{-1}, corresponding to an effluent yield of 0.115%. The **UiO-67-10% bipy/Pt*** showed similar rates, as expected. The peak in methanol formation rate is not present for the **UiO-67-BN(10% bipy)/Pt**.

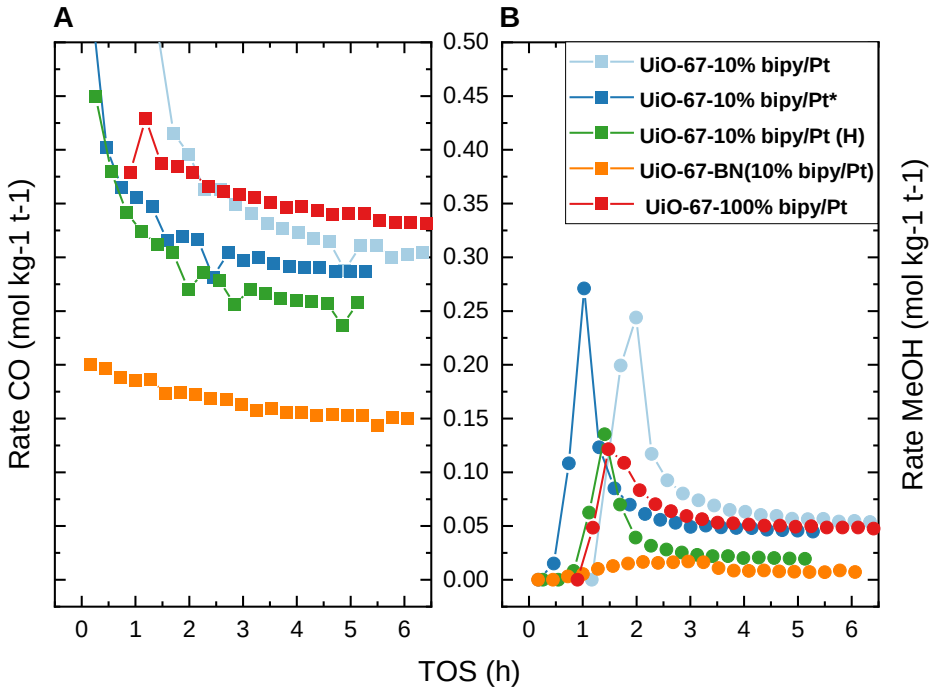

Figure 4.27: *The rate of formation as a function of TOS form carbon dioxide (**A**) and methanol (**B**) for the UiO-67 samples. The y-axes is the same.*

The peak in methanol rate is not present in the UiO-66 samples, indicating that the initial pathway that methanol formation follows is somewhat different. The tests show that the version of **UiO-67-10% bipy/Pt*** that had been healed had in general lower activity than the unaltered one, both having a lower CO and MeOH rate.

It is interesting to note that the two samples with larger Pt nanoparticle sizes, **UiO-67-10% bipy/Pt** (4.23 nm) and **UiO-67-100% bipy/Pt** (4.29 nm) had highest and lowest TOF, respectively, among the UiO-67 samples. The two samples with intermediate Pt nanoparticles

had TOFs in-between the two. This result show that other parameter than the Pt nanoparticle size is influencing sample activity.

The turnover frequency was also calculated for the UiO-67 samples and can be found in ***Figure 4.29***.

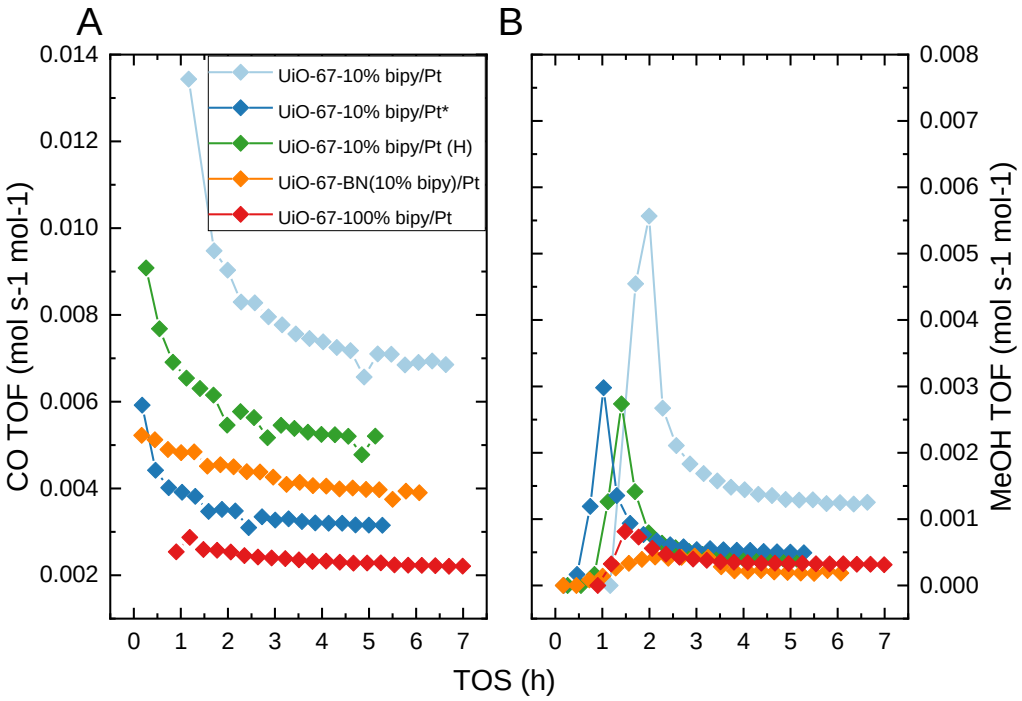

Figure 4.29: *The TOF towards CO (**A**) and MeOH (**B**) for the UiO-67 samples.*

The **UiO-67-10% bipy/Pt** sample show the highest TOF for both carbon monoxide and methanol. Both the healed and the unaltered version of the **UiO-67-10% bipy/Pt*** have the same TOF towards MeOH, but have a 0.002 mol s^{-1} mol^{-1} difference in CO TOF at steady-state. The healed samples, **UiO-67-10% bipy/Pt (H)**, have less missing linker defects. This result might suggest a correlation between MOF defectiveness and MeOH formation, supporting the arguments and findings made by Gutterød *et al.*.[1]

To further investigate the peak in MeOH rate, a series of tests were conducted to investigate whether it was due to the difference in activating temperature between UiO-66 and UiO-67 samples (200 °C versus at 350 °C). A sample of **UiO-67-10% bipy/Pt** was therefore tested after being activated at 200 °C and compared with the same sample activated at 350 °C. The carbon monoxide and methanol yield were calculated and plotted and can be seen in ***Figure 4.30***.

As expected, and shown in previous unpublished works by Solemsli *(BSc project)*, the MeOH production peak disappears when the catalyst is activated at 200 °C. [33, 38] Both the CO and MeOH yield from the 200 °C activated catalyst were lower than the one activated at 350 °C. The missing data points in the sample activated at 200 °C is due to very large uncertainty. The sample activated at 200 °C had about the same Pt nanoparticels than the sample activated at 350 °C (3.4 ± 1.2 nm). Gutterød *et al.* reported that samples are able to be reduced by the reaction feed.[34] This may have been the case and why the sample activated at 200 °C a lower activity.

It was later found out by Gutterød *et al.* that this peak is related to water formed during synthesis, re-hydrating the Zr-node after water desorbs during activation at 350 °C, exposing the Zr-O-Zr sites.[42, 45] When reintroducing a wet inert feed, the initial peak in methanol disappeared while the MeOH formation and steady-state remained the same. A plot of this can be seen in ***Figure 4.31***. This indicates that water and methanol precursor, CO_2, compete for the Zr-O-Zr sites on the node, limiting the formation of methanol.

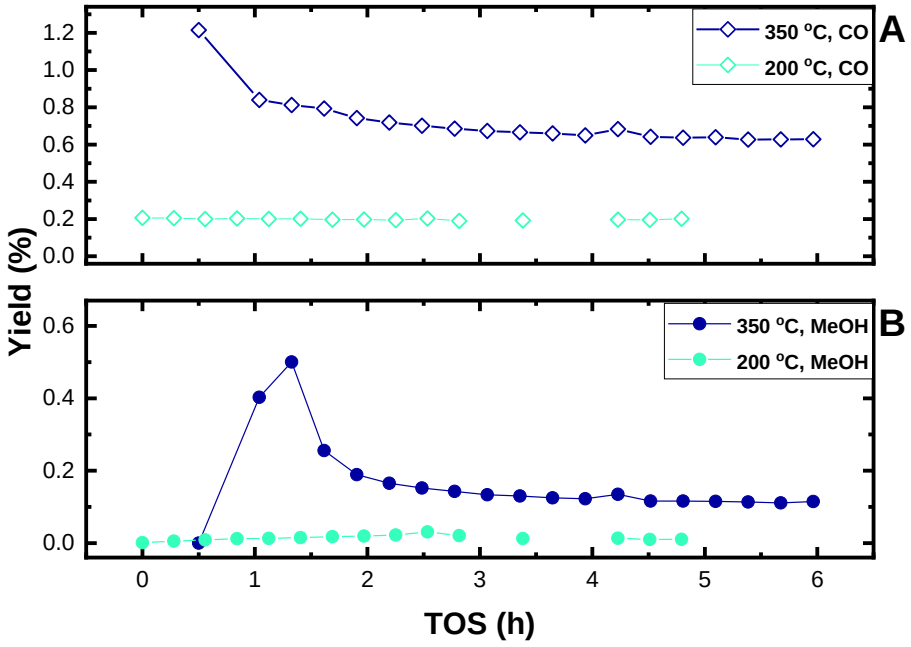

Figure 4.30: *Graphs comparing percentage yield (effluent) as a function of time on stream of the* ***UiO-67-10% bipy/Pt*** *samples activated at 350 °C and 200 °C in 1:9 H_2:Ar 20 mL/min flows. The top graph (**A**) is the carbon monoxide yield, while the bottom graph (**B**) is the methanol yield.*

These results show that the UiO-67-100% bipy/Pt sample has the same activity towards methanol while having less activity towards CO. This might be a result of the increased nitrogens in the system that could help facilitate the splitting of molecular hydrogen, as suggested by Formenti and Vilé *et al.*.[40, 41]

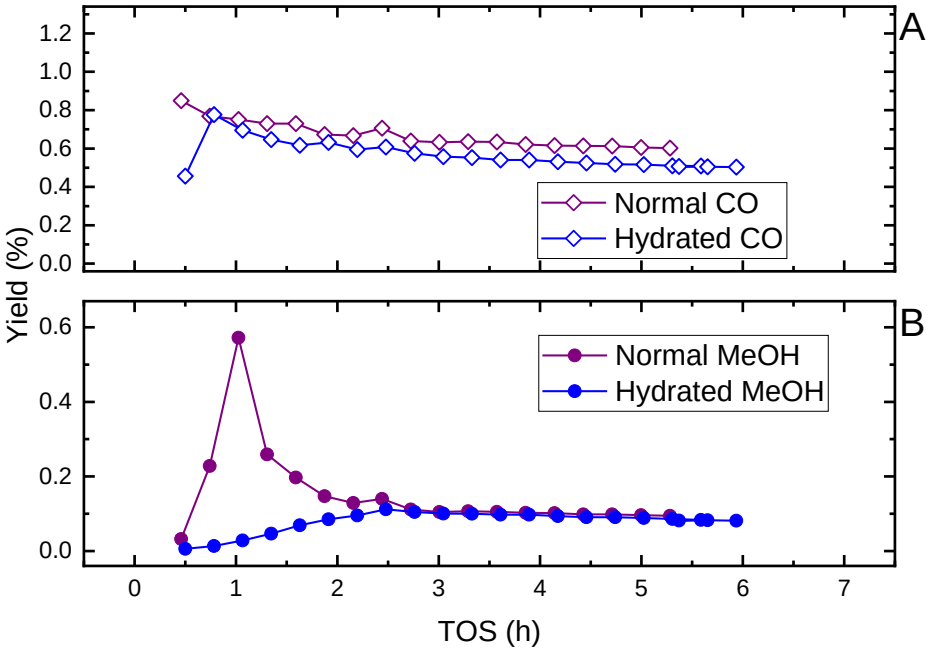

Figure 4.31: *Graphs comparing percentage yield (effluent) as a function of time on stream of the* ***UiO-67-10% bipy/Pt**** *sample vs. the same sample rehydrated before reaction. The top graph (**A**) is the carbon monoxide yield, while the bottom graph (**B**) is the methanol yield.*

When looking at different UiO-67-type structures, Øien-Ødegaard *et al.* found that the UiO-67-BN sample showed a much higher stability to water.[46] This was linked to the binaphtyl-linkers sterically shields both the Zr-nodes and the carboxylic groups from being able to adsorb gaseous species. This also causes the pore volume to decrease compared to the normal UiO-67 system. The lack of the initial peak in MeOH formation for the **UiO-67-BN(10& bipy)/Pt** sample may be explained by this phenomenon. Since water and CO_2 adsorbs on the on the same Zr-node site, this shielding may also decrease the methanol formation and explain the lower activity of the **UiO-67-BN(10% bipy)/Pt** compared to the other UiO-67 samples.

4.3.3 Different platinum loadings in UiO-67-10% bipy/Pt*

The three samples with different Pt loading were tested using the same procedure as the previous samples. The CO_2 conversion, as depicted on ***Figure 4.32***, show that the two samples **UiO-67-10% bipy/less Pt** and **–ex Pt**, have higher conversion than the standard **UiO-67-10% bipy/Pt*** sample. The samples all follow the same trend as they all reach steady-state.

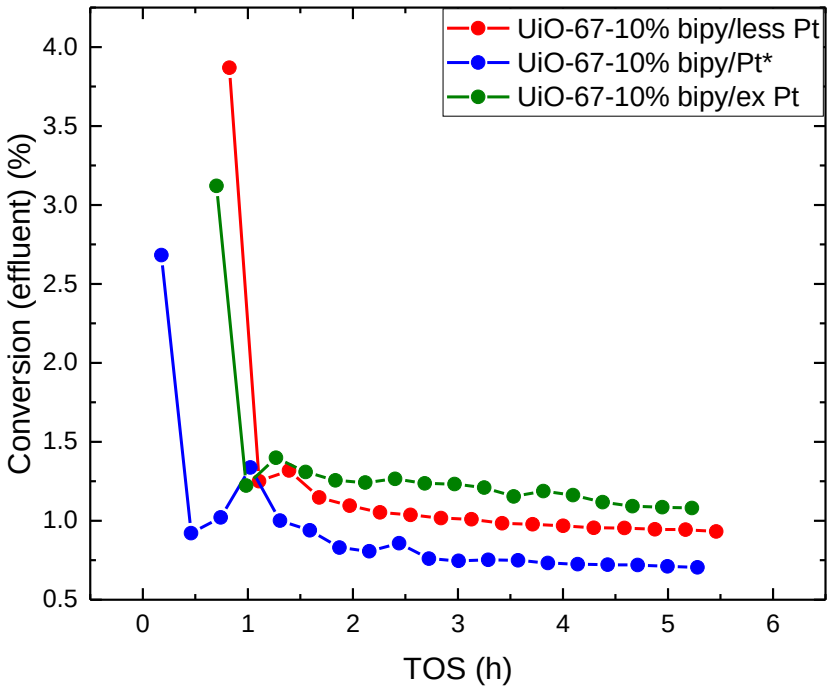

Figure 4.32: *A plot of the CO_2 conversion as a function of TOS for the three samples: UiO-67-10% bipy/less Pt (red), UiO-67-10% bipy/Pt* (blue) and UiO-67-10% bipy/ex Pt (green). The samples were tested at 170 °C in a 1:3:1 CO_2:H_2:Ar(10% Kr) 20 mL/min flow.*

The carbon monoxide and the methanol selectivity can be seen in ***Figure 4.33***. Both the standard and the low Pt content sample behaved the same way with a methanol selectivity of 12-14% when the reaction has reached steady-state. The **UiO-67-10% bipy/ex Pt** appears to have more sites leading to MeOH formation than the two other samples ending with a selectivity of about 17.5% compared to 13.8% and 12.2% for **UiO-67-10% bipy/Pt*** and **UiO-67-10% bipy/less Pt**, respectively. The **UiO-67-10% bipy/less Pt** sample have the highest CO selectivity of 87.5% at steady-state, while the **UiO-67-10% bipy/Pt*** and **UiO-67-10% bipy/ex Pt** had 85% and 80%, respectively.

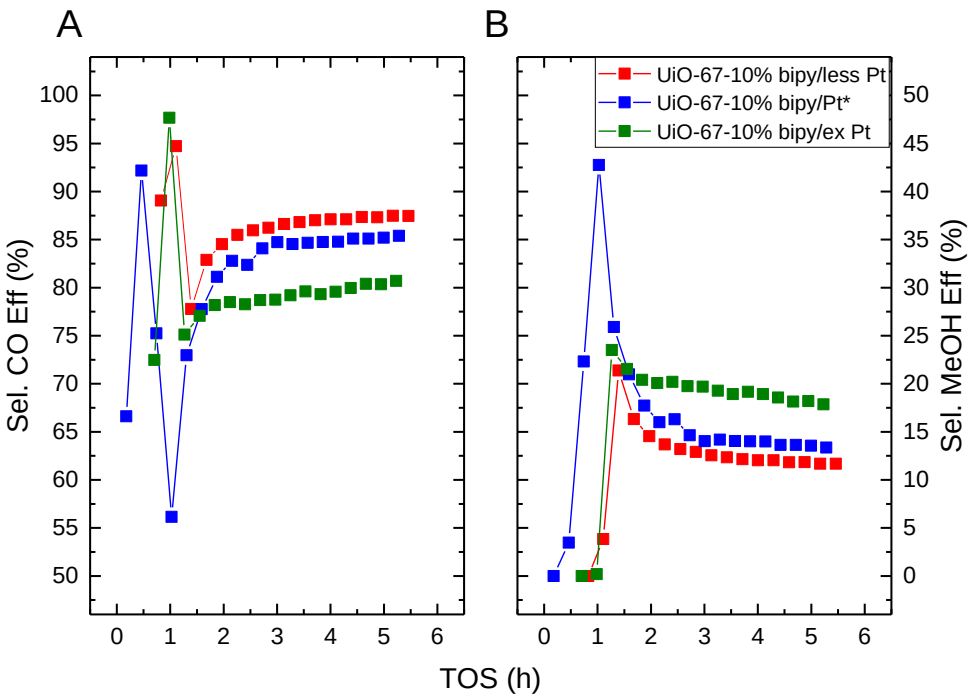

Figure 4.33: *A plot of the CO (**A**) and MeOH (**B**) selectivity as a function of TOS for the three samples.*

The rate of formation of CO and MeOH was also calculated (***Figure 4.34***). The same trend as with the earlier UiO-67 samples was seen. The peak in the MeOH formation, show up here for all the samples, similar to the other UiO-67 systems. The samples have similar MeOH rate, but have a vastly different CO rate. The **UiO-67-10% bipy/ex Pt** sample had the highest rate towards both products.

In order to be able to directly compare these samples, turn over frequencies for both carbon monoxide and methanol were calculated. The results were plotted as a function of TOS in ***Figure 4.35***. Here it becomes apparent that the TOF for the **UiO-67-10% bipy/less Pt** sample is higher than the TOF for the two other samples. The two other samples had about the same TOF towards CO. The **UiO-67-10% bipy/ex Pt** had the highest MeOH TOF, while the two others had the same MeOH TOF. The **UiO-67-10% bipy/less Pt** sample was therefore tested again. The results can be seen in ***Figure S13***, and show that the results are reproducible.

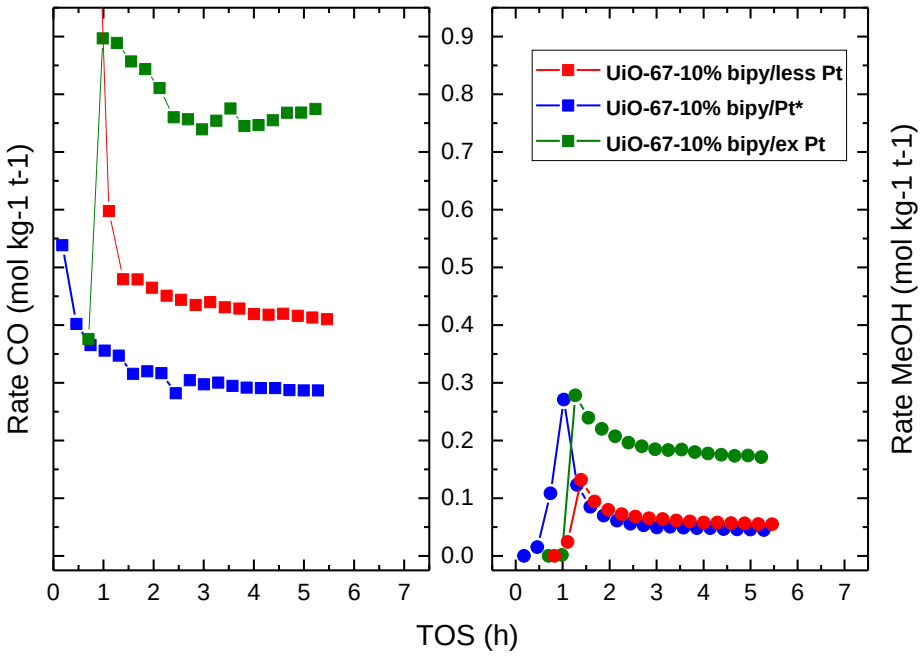

Figure 4.34: *A plot of the CO (**A**) and MeOH (**B**) rate of formation as a function of TOS for the three samples.*

The **UiO-67-10% bipy/less Pt** had slightly fewer and smaller particles than the two other samples. The amount of low coordinated faces on a particle will increase as the particle gets smaller. The high CO TOF indicates that dissociation of CO_2 into CO and H_2O occurs on these low coordinated sites, supporting the theoretical investigation of Li *et al.*.[47] The relatively low turnover frequency towards methanol for the UiO-67-10% bipy/less Pt sample can be explained by the lower density of platinum nanoparticles (see ***Table 4.8***). Fewer platinum particles in the system means less possible Zr-node:Pt nanoparticle interfaces.

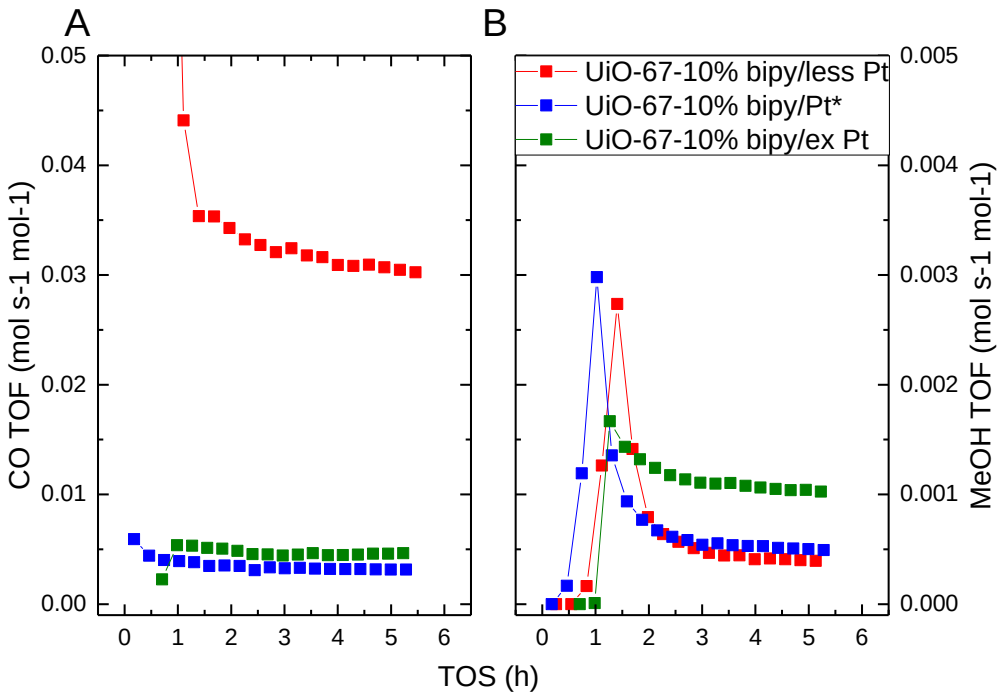

Figure 4.35: *A plot of the CO (**A**) and MeOH (**B**) turn over frequency (TOF) as a function of TOS for the three samples.*

4.3.4 Defects in UiO-67-10% bipy/Pt** induced by oxygen calcination

The two extreme points were chosen to test, **UiO-67-10% bipy** 0h** and **UiO-67-10% bipy/Pt 16h**. This was due to time constraints. The samples were tested in collaboration with Dr. Christian Ahoba-Sam at a rig setup that had mechanical pressure control of the reactor. It was therefore decided to test the samples at different pressures (0-30 bar) and at different temperatures (170-375 °C). The UiO-67-10% bipy/Pt 0h was only tested up to 240 °C due to the possibility of collapse of the material. Since the UiO-67-10% bipy/Pt 16h was presumed to have lost most of its MOF structure, it was tested to the extreme (375 °C). The conversion as a function of temperature and pressure can be seen in ***Figure 4.36***.

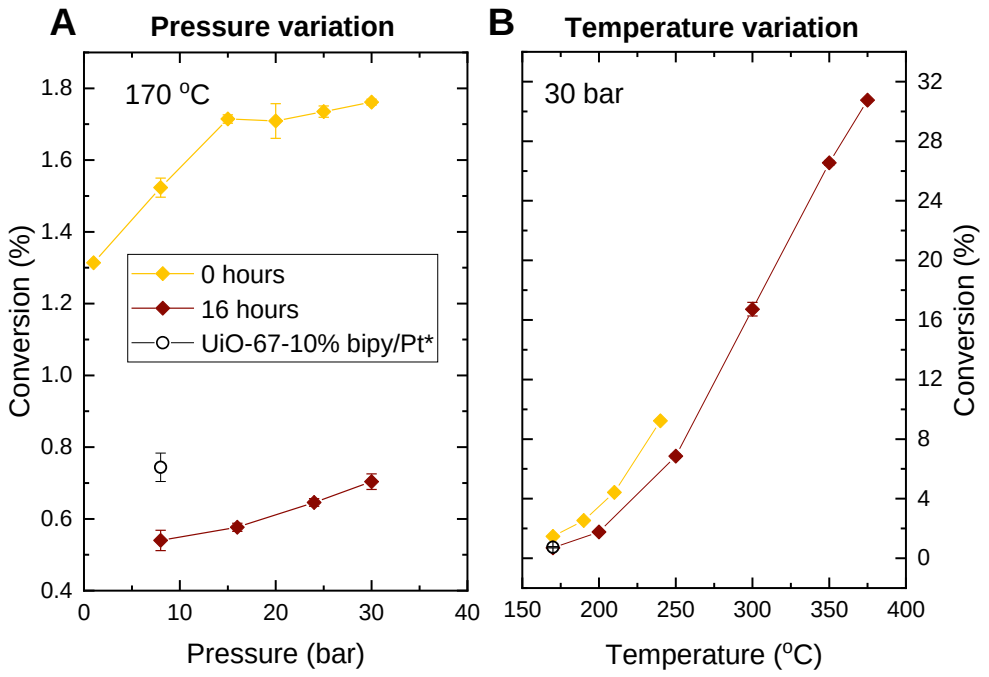

Figure 4.36: *Conversion of the samples* ***UiO-67-10% bipy/Pt 0h*** *(yellow) and* ***UiO-67-10% bipy/Pt 16h*** *(maroon) and* ***UiO-67-10% bipy/Pt**. Plot **A** show the pressure variation and plot **B** show the temperature variation. The temperature was held constant at 170 °C in **A** and the pressure was held constant at 30 bar in **B**. The samples were tested in a 1:3:1 CO_2:H_2:Ar(10% Kr) 20 mL/min flow.*the y-axis are not the same*

The conversion of the samples increases exponentially with increase in temperature, while only increasing slightly with increase in pressure. The unaltered sample yields the highest conversion of the two samples, even higher conversion than the similar **UiO-67-10% bipy/Pt*** sample. The **UiO-67-10% bipy/Pt 16h** sample has an exponential increase in conversion until the sample reaches 375 °C. This is the temperature at which the UiO-67 MOF will start to degrade. The change in the trend of the graph may indicate that not all the organics had been burned off in the oxidation step. The change in conversion over time can be seen in ***Figure 4.37***. The high conversion right after the temperature variation is due to the change back to 170 °C from 375 °C. The activity of the 16 hour burned sample is very stable after both pressure and temperature variation. This may be because most of the pore structure has been lost during the oxidation.

The selectivity as a function of both pressure and temperature can be seen in ***Figure 4.38*** and ***Figure 4.39***, respectively. The selectivity towards methanol increases as the pressure increases for both the samples, following what is expected considering the thermodynamics. The burned sample have the highest MeOH selectivity of 48% at 30 bar and 170 °C, but has increased activity towards methane as well.

The methanol selectivity decreases as temperature increases. This is to be expected when considering the thermodynamics of the reactions. At higher temperature methane and CO is more favorable, and also what has been seen earlier by Gutterød *et al.*.[42] What is interesting to note is that the selectivity towards carbon monoxide decreases when the temperature goes above 300 °C. At 375 °C, the methane selectivity is at high as 42.5% for the burned sample.

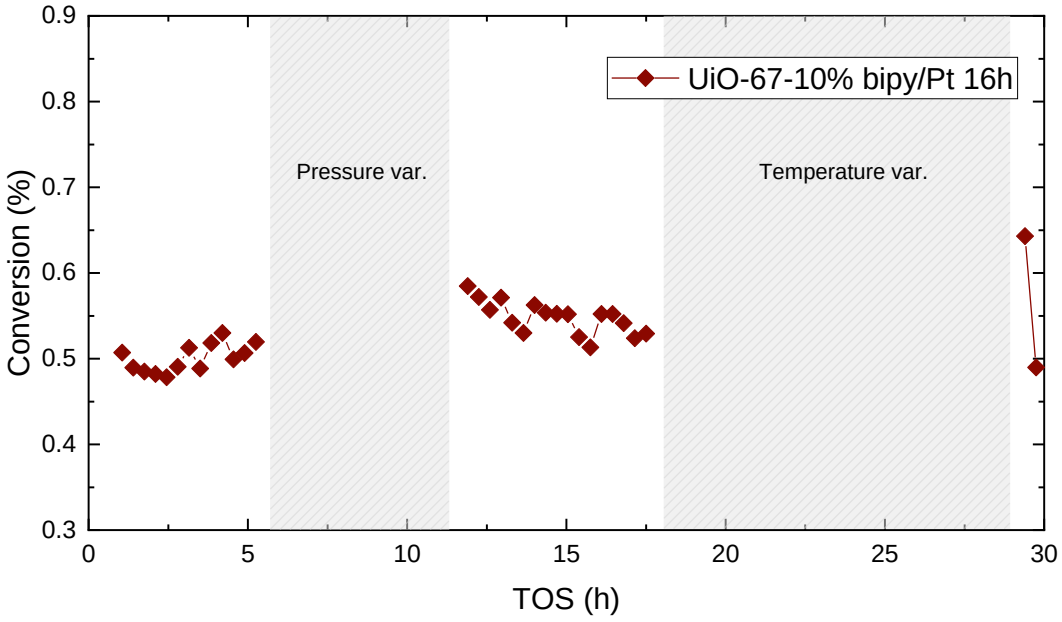

Figure 4.37: *Conversion as a function of TOS for the* ***UiO-67-10% bipy/Pt****. The two gray areas are the timeslot of the pressure variation and the temperature variation tests.*

Based on these experiments it is clear that to increase the formation of methanol, the thermodynamics have to be favorable. When the reaction takes place at 30 bar the collisions between species increases, thus increasing the adsorption and interaction with H_2 and CO_2. For a molecule as relatively large as methanol (CH_3OH) it is therefore favorable to have high pressure, low temperature and a high H_2/CO_2-ratio, while carbon monoxide is favored at lower pressure.[48] According to Le Chateliers principle, the position of equilibrium will move to counteract the change in the system. By increasing the pressure, equilibrium will try to reduce the pressure by forming fewer molecules. Since the methanol formation reaction consumes four molecules to make two molecules, compared to five to three and two to two towards methane and carbon monoxide, respectively, the equilibrium will favor the formation of methanol (see ***Eq. 1.6-1.8***).

In the effort of converting carbon dioxide, having high selectivity towards methanol can be seen as more important than having high conversion. This is due to the ease of separating the methanol (with water) at room temperature. The remaining effluent feed can then be converted to other species, such as hydrocarbons though the use of other catalysts, or reused.

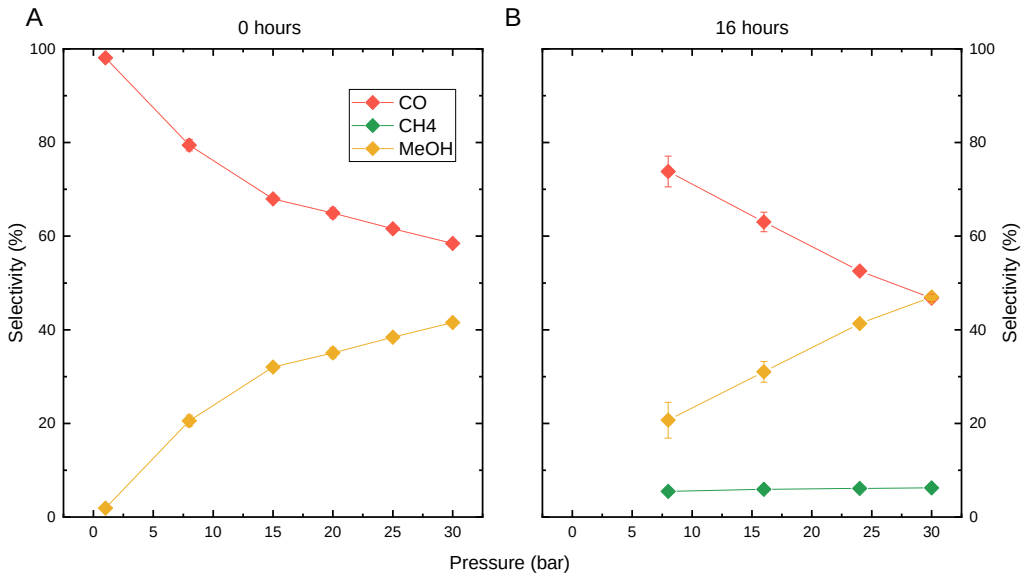

Figure 4.38: *CO, CH_4 and MeOH selectivity for the samples* ***UiO-67-10% bipy/Pt 0h*** *(**A**) and* ***UiO-67-10% bipy/Pt 16h*** *(**B**) as a function of pressure.*

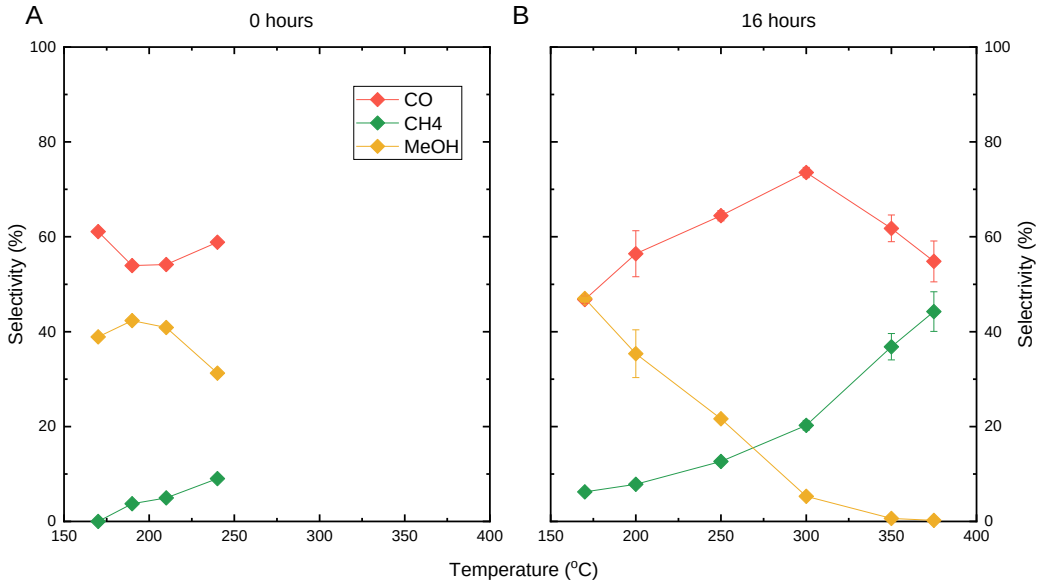

Figure 4.39: *CO, CH_4 and MeOH selectivity for the samples* ***UiO-67-10% bipy/Pt 0h*** *(**A**) and* ***UiO-67-10% bipy/Pt 16h*** *(**B**) as a function of temperature.*

Even though the morphology of the two samples is quite different, and the conversion being different, they seem to follow the same trend with changing temperature and pressure. This may suggest that the same reaction pathways are present in both samples. The burned sample have a higher selectivity towards methanol at 170 °C and 30 bar, while having a lower conversion. The lower conversion may be caused by the lower availability of the surface as the structure of the oxidized sample deteriorates leading to less more available Zr-node sites, or similar sites in the ZrO_2.

A hydrogen to deuterium transient study at 1 bar and 170 °C was performed with the **UiO-67-10% bipy 0h** sample. The formation rates of this test can be seen in ***Figure 4.40***, and the normalized MS spectrum can be seen in ***Figure 4.41***. When the feed was switched for H_2 to D_2, both the methane and methanol formation rates increased, while the carbon monoxide rate decreased 98.2%, 71.9% and 10.6%, respectively. At isotope steady-state the difference in formation rates were:

$$r_{CO,H_2}/r_{CO,D_2} = 1.12 \qquad \textbf{(4.1)}$$

$$r_{CH_4,H_2}/r_{CH_4,D_2} = 0.02 \qquad \textbf{(4.2)}$$

$$r_{CH_3OH,H_2}/r_{CH_3OH,D_2} = 0.28 \qquad \textbf{(4.3)}$$

These numbers show the presence of an inverse kinetic isotope effect (KIE) for methane and methanol, and a normal KIE for carbon monoxide. The inverse KIE observed for methane and methanol formation is typical for when a reaction involves addition of hydrogens to a sp- or sp^2-hybridized carbon, leading to a hybridization change. The formation of methanol involves two such steps, formation of formate and the formation of dioxymethylene, with the last intermediate being assumed to take place, but is not observed.[1] The inverse KIE for methane is clearly present, but the actual ratio is uncertain due to the CH_4 signal in hydrogen atmosphere is close to the detection limit of the chromatograph. The $r_{CH_3OH,H_2}/r_{CH_3OH,D_2}$ observed here is less than what Gutterød et al observed for the system ($r_{CH_3OH,H_2}/r_{CH_3OH,D_2} = 0.36$ and $r_{CH_4,H_2}/r_{CH_4,D_2} = 0.6$).[1] Furthermore, for $r_{CO,H_2}/r_{CO,D_2}$, a slight decrease in KIE is observed, as opposed to what is reported by Gutterød *et al.*.[1] This can be explained by the doubling of mass when switching to deuterium (***Eq. 1.6***).

Using the signal for the MS, the surface area residence time and the amount of adsorbed intermediates for methane and methanol were calculated using ***Eq. 2.40***. The results are shown in ***Table 4.10***. In order to account for products in the gas phase, the transient from the inert, Kr, was subtracted from the calculated surface residence time.

Table 4.10: The surface residence time and the amount of adsorbed intermediates.

Species	Surface residence time, τ_{res} (s)	Amount of adsorbed intermediates, N_{ads} (mol kg^{-1})
CH_4	6.5	$6.27 \cdot 10^{-7}$
MeOH	24	$1.32 \cdot 10^{-4}$

Both methane and methanol requires the same Zr-O-Zr site to be formed, but follow different reaction pathways. Gutterød *et al.* based these calculation from a C^{12}/C^{13}-transient experiment and reported higher $\boldsymbol{\tau_{res}}$ and $\boldsymbol{N_{ads}}$ values. This difference may be caused by the higher conversion of the **UiO-67-10% bipy/Pt 0h** compared to the sample tested by Gutterød *et al.*.[1] The system took longer to reach steady-state when it was switched back to a hydrogen atmosphere.

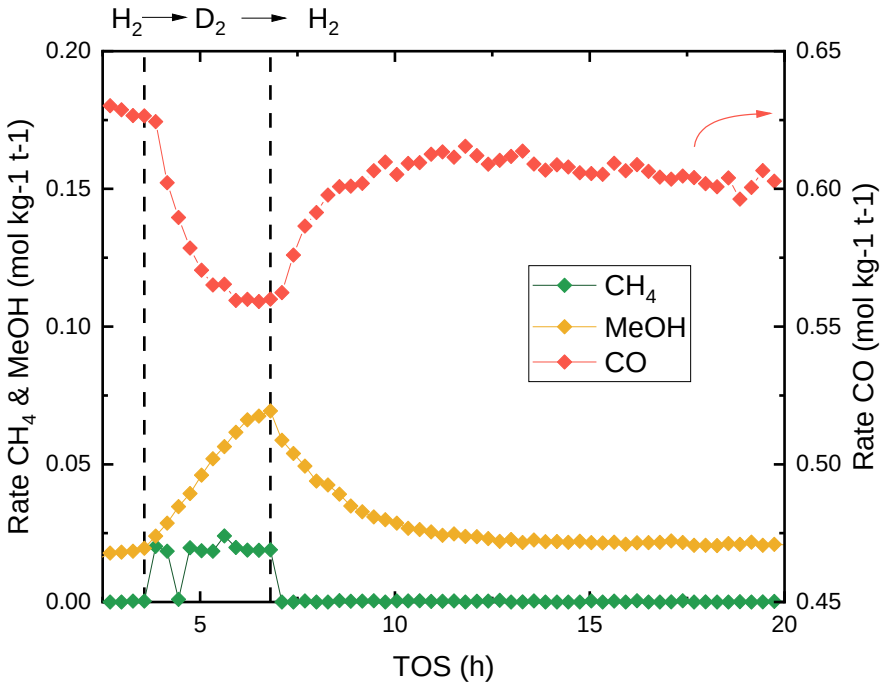

Figure 4.40: *CO, CH_4 and MeOH rates for the samples* ***UiO-67-10% bipy/Pt 0h*** *during the transient from H_2, to D_2 back to H_2. The methane and the methanol are on the left y-axis, while carbon monoxide is on the right axis. The dashed lines indicate when the feed was switched from H_2 to D_2 and back.*

Both the methane and methanol signal drop rapidly down to 0.4 and 0.8, respectively, after the switch. This drop is likely due to the delay in the feed when the feed is switched from hydrogen to deuterium. Because of the delay, it was hard to define the best point to normalize the data to.

Based on the raw data shown in ***Figure 4.42***, the delay was estimated to be around 10 seconds. Gutterød *et al.* observed that the methane signal rapidly decreased, indicating that the surface residence time for the methane intermediates was short. This is not observed here, as the methane signal decreases exponentially from 0.4 to 0.1. The overall shape of the curves also differ a little from the curves presented by Gutterød *et al.*. The two materials used can therefore be said to behave slightly different, as can be seen from the difference in conversion and selectivity of the two samples.

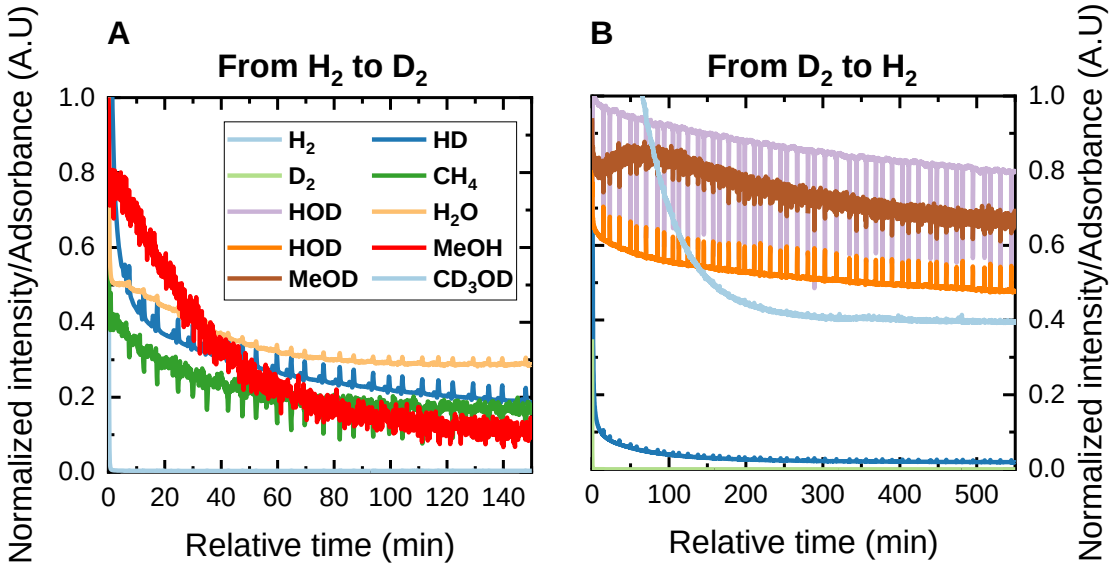

Figure 4.41: *Normalized MS spectrum from when the feed was switched to deuterium (***A***) and when the feed was switched back to hydrogen (***B***). The data is normalized to the signal right before the switch.*

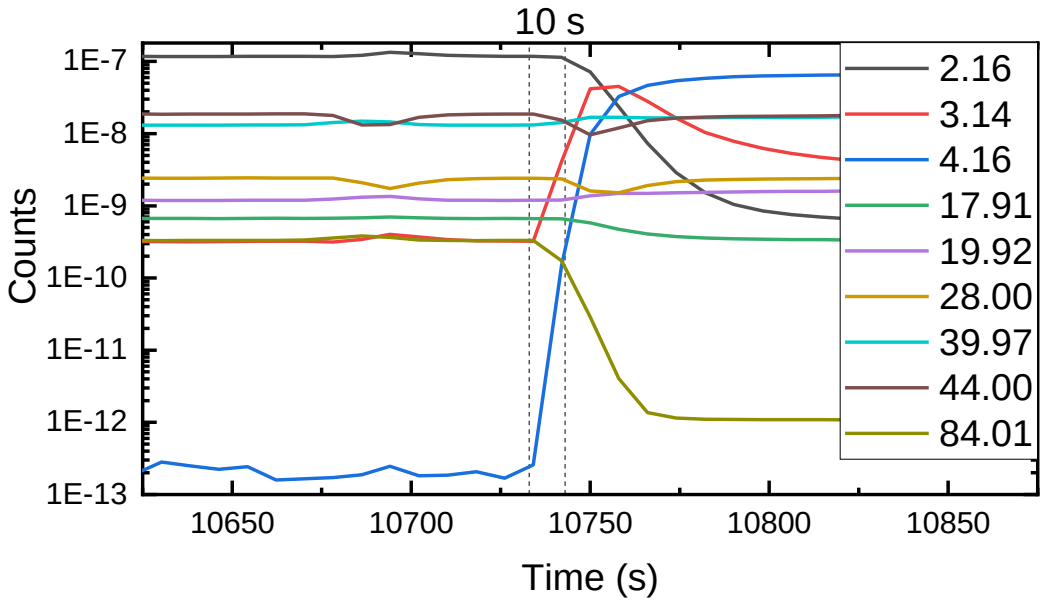

Figure 4.42: *Raw data form the MS depicting the delay from when the feed was switched from hydrogen atmosphere to deuterium atmosphere. The dotted lines indicate the 10 second delay.*

4.4 Discussion

As stated in the Abstract and Introduction, the aim of this thesis was two-fold: First, to study Pt nanoparticles formed in various UiO-66 and -67 metal-organic frameworks (MOFs) by Transmission Electron Microscopy (TEM), and second, to study the Pt-containing MOFs as catalysts for the CO2 hydrogenation reaction. In the previous sections, results obtained over each group of materials were presented and discussed. In this section, the ensemble of results will be considered and discussed.

4.4.1 Pt nanoparticles in MOFs

Based on the investigation in TEM the nanoparticle size can be said to be between 2.4 nm and 5.5 nm. Some deviations exists, namely the **UiO-66-BDC(10% NH_2)/Pt** sample and the **UiO-66-BDC(100% COOH)/Pt** who had very large and no definable particles, respectively. Statistics of the samples reveal that each sample has a uniform nanoparticle size distribution with minimal spread in size. In the micrographs, the particles appeared either as circles or as defined shapes with 4-6 edges. A model was made of a 3 nm particle using surface energies reported by Material Virtual Lab© using the NanoCrystal© software using Wulff-construction (***Figure 4.43***). Based on this model, it was concluded that the platinum nanoparticles should make a hexagonal shape in the TEM and STEM images, when looking down the 111 face.[49-52] The large surfaces that show the hexagonal pattern is the [111] surface. This particle contains 1061 platinum atoms with 6,14% of the atoms exposed to the surface.

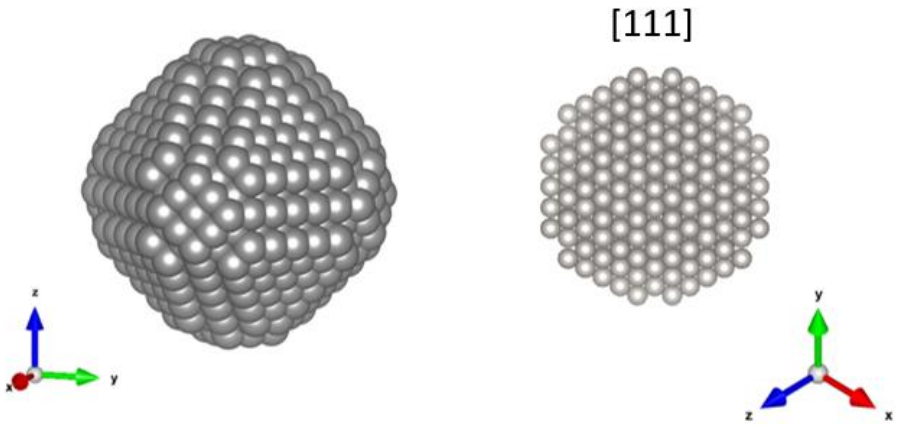

Figure 4.43: *A model of a 3 nm (diameter) platinum nanoparticle, if grown without any outside influence. The particle was built using the surface energies reported by Martials Virtual Lab ©[49-51] using the software NanoCrystal ©[52]. The crystallography data was take from Materials Project[53, 54].*

The defined edges observed suggest that octahedral crystals have been formed. All the platinum particles form these type of crystals, indicating that the dominant face of the platinum particles is the [111] face in the systems.

To understand the way the particle may have formed inside the MOF matrix, many factors have to be considered. One factor that may play a role is the synthesis of the parent materials. During synthesis the amount of missing linker/modulator has proven to be harder to control than first assumed. Extensive tests by Kaur *et al.* revealed the possible ways of tuning the synthesis of the UiO-67 MOFs to get the desired amount of defects.[32] The three UiO-67 samples were synthesized before and after this knowledge was acquired, so the amount of defects in each sample may vary. TGA analysis was used to estimate the amount of defects in a sample. To more accurately get a description of the amount of each linker and missing linker/modulator, H^1NMR of the digested MOF prior to metalation is normally used, ad such analysis was not part of the current study. It is therefore hard to separate the samples based on the amount of defects.

Even when the same batch was used, as in the case for the **UiO-67-10% bipy/Pt*** and **UiO-67-10% bipy/Pt (H)**, getting the same amount of grafted $PtCl_4^{-2}$-salt into the frameworks proved difficult. Even though the same procedure was followed for all the UiO-67 samples, they all ended up with different amounts of platinum in the system. There are many factors that may play a role in this, one of them being the dispersion of the grafting site, e.g., the functional linker. Since the dispersion of the linker is yet unknown, decoupling the dispersion of functional linker and diffusion of the platinum salt is not possible. All samples proved to reduce the platinum after being subjected to a reducing hydrogen atmosphere, although the final morphology of the metallic platinum was different. Without a clear grafting site for the salt, like for the case of the **UiO-66-BDC(100%COOH)/Pt** sample, the platinum will not form nanoparticles, but grow into larger entities. This may be caused by lack of diffusion of the salt, leaving most of the salt close to the surface. This sample also showed signs of being reduced after synthesis based on the difference in colour from compared to the two other UiO-66 samples after metalation.

The exact mechanism for platinum nanoparticle formation is still unknown, but it is well documented that the reduction in hydrogen is key for the formation of metallic platinum from the $PtCl_4^{-2}$-complexes.[33, 34, 55, 56] The reduction of the grafted platinum complex is hypothesized to occur with the following reaction, where n=1 for the amine part of the bipy-linkers and n=2 for the amine part of the BDC linkers:

$$(-\mathrm{NH}_n)_2\mathrm{Pt(II)Cl}_2 + 2\mathrm{H}_2 \rightarrow \mathrm{Pt(0)} + 2\mathrm{HCl} + 2(-\mathrm{NH}_{n+1}) \qquad \textbf{(4.4)}$$

Moliner *et al.* suggested that the platinum atoms in a zeotype Chabazite A crystal migrate within the porous system in H_2, before agglomerating on the surface and form particles[55]. A similar mechanism can be argued to be occurring the MOF systems.

Although there are more than enough cavities for the platinum particles to merge and create larger particles, it does not seem like the platinum particles migrates into these cavities and agglomerate. Even after a long time under the electron beam in the TEM, the particles do not grow or move, although the surrounding MOF degrades. This confirms the extraordinary stability of these particles as reported by Gutterød *et al.,* and can be explained if the diffusion of platinum atoms is limited.[1]

The "perfect" shape of the nanoparticles can also be explained if they mainly form on, or close to the surface of the MOF crystallites. The nanoparticles that are not covered by MOF will naturally grow based on the different surface energies of the different faces, thus creating nice crystals with complete particles and no "unfinished" faces. Gutterød *et al.* discussed that the interaction between the Pt nanoparticle and the Zr-cluster weakens the node-to-linker O-C bonds, thus the nanoparticle can grow beyond the spatial limitations of the MOF pores.[1] This may also explain why defined crystal shapes can be found in the MOF.

The uniform size and distribution of the particles is probably a result of Ostwald ripening taking place to a certain degree, but they seem to stop growing after a while, which is why the particles are quite similar in size. This suggests that the diffusion of platinum species inside the MOF is limited.

The MOF and the nanoparticles do not share any growth relation ship. Based on the lack of observed interactions in TEM between the platinum nanoparticle crystals and the surrounding MOF-matrix may suggest that the platinum particle is not stabilized by the MOF, but rather contained by it.

4.4.2 Performance of UiO-66/Pt and UiO-67/Pt as CO_2 hydrogenation catalysts

This master thesis is an extension of a PhD thesis that was performed (partially) in parallel with the current thesis by Gutterød *et al.*.[42] The PhD thesis work revealed mechanistic details about the CO_2 hydrogenation reaction over two specific Pt/UiO-67-bpy MOF samples, which are called: "**UiO-67-10% bipy/Pt**" and "**UiO-67-10% bipy/Pt***" in the current thesis. Briefly, it was revealed that the role of Pt NPs in this system is mainly to facilitate the reverse water gas shift reaction (***Eq. 1.6***), and that the interface between the Pt NPs and the Zr nodes of the MOF

framework is essential for the formation of methane and methanol. More precisely, it was found that methanol is formed via formate species attached to open Zr sites, and that Pt NPs provide hydride species required to reduce CO_2 via formate to methanol.[1, 42]

All samples in this thesis were tested under the same conditions (temperature, total pressure, reactant feed ratios, contact time) and is therefore considered to be directly comparable. Most of the UiO-66 and UiO-67 samples give a conversion at about 0.75% while having different selectivity.

Literature studies suggest a correlation between Pt nanoparticle size and catalytic activity. Mayrhofer *et al.* saw an increase in the binding strength of oxygenated species with decreasing particle size of Pt.[57, 58] Similarly Maillard *et al.* observed that the mobility of carbon monoxide on Pt nanoparticles smaller than 4 nm was lower than compared to bulk metal surfaces.[59] Li *et al.* did DTF calculations on the Pt(111) and the Pt(211) surface for 0.7 to 3 nm nanoparticles that revealed that the oxygen adsorption energy was lower on the Pt(211) surface in particles larger than 0.7 nm.[47] Since the particles observed inside the MOF here are generally larger than 3 nm, it can be argued that the Pt(211) surface or other low coordinated sites (Pt(332), Pt(322) etc.) are the active surfaces on the platinum particles. Compared to the Pt(111) surface (0.093 eV/Å^2), the Pt(211) surface (0.110 eV/Å^2) and other low coordinated surfaces are less stable. This means that as the particle grows, these surfaces become less available. This indicates that smaller particles should be more active than larger particles, as long as they do not confine to the quantum-size effect (approx. larger than 1 nm).[60] Having small particles should also increase the number of possible interactions with the Zr-nodes, thus also having an increased activity for methanol.

Interestingly, this is not observed for the samples investigated here. As shown in ***Figure 4.29***, the platinum nanoparticle size does not affect the activity of the MOF. Gutterød *et al.* reported that CO adsorbed on the platinum particles may block hydrogen from adsorbing, inhibiting the formation of methane and methanol.[1] The similar conversion regardless of nanoparticle size for the samples may suggest that the platinum surface is close to saturation with adsorbed CO, inhibiting the reaction.

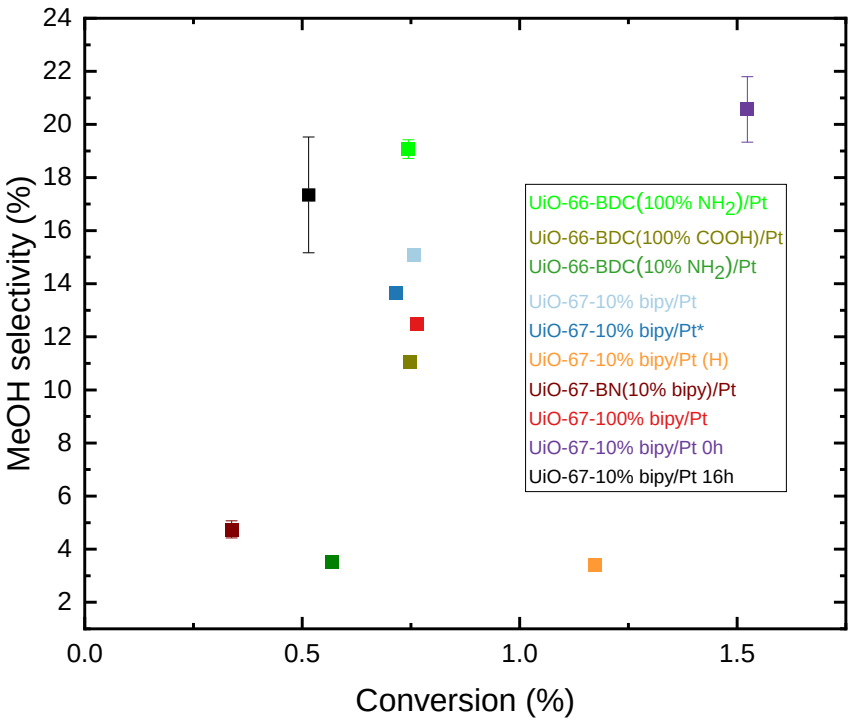

Figure 4.44: *MeOH selectivity as a function of CO_2 conversion.*

A plot of the methanol selectivity as a function of conversion can be seen in ***Figure 4.44***. It cannot be concluded that there is a clear correlation between the conversion and the MeOH selectivity. Since all the samples have 75% or higher selectivity towards CO, it can be said that the conversion is more influenced by the RWGS reaction than by other reactions. CO formation does not require an interface between the Pt nanoparticles and the Zr-node, so the conversion would be similar for the systems if they have the same amount of platinum surfaces, regardless of the surrounding MOF. This also shows that the linkers of the samples do not seem to take part in the reaction in any observable way.

The initial peak in methanol formation observed for the UiO-67 samples suggest that water formed during the reaction compete with MeOH for the Zr-O-Zr sites. As previously stated, is this peak not present for the UiO-66 samples. This may be due to the activation temperature used for the UiO-66 samples. The Zr-nodes have the ability to dehydrate, exposing the Zr-O-Zr when heat-treated. Shearer *et al.* reported that this dehydration occurred between 250-300 °C, which is higher than the activation temperature used for the UiO-66 samples.[45] Since CO is the dominant product of the reaction, the inhibiting by water is not significantly relevant for the

overall conversion of the catalysts. Gutterød *et al.* suggested that the total rate of conversion could be defined by the following equation.[1]

$$r_{total} = k \cdot K \cdot \frac{P_{CO_2}^{0.9} \cdot P_{H_2}^{0.2}}{\left(P_{CO} + P_{H_2O}\right)^{1.1}} \qquad \textbf{(4.5)}$$

Since the RWGS reaction is the dominant reaction, the inhibition from water could be regarded as close to zero, thus the poisoning of the Pt nanoparticles by CO is responsible for limiting hydrogenation of CO_2 over UiO-Pt MOFs.

The results in ***Section 4.3.2***, show that the reproducibility of a batch is more difficult in terms of replicating the catalytic behavior than first assumed. Even though the **UiO-67-10% bipy/Pt**, **UiO-67-10% bipy/Pt*** and **UiO-67-10% bipy/Pt 0h** samples are synthesized following the same synthesis protocols, they show vastly different activity, both in terms of conversion and selectivity, Pt amount and Pt nanoparticle size.

Based on the results from varying the amount of platinum in the **UiO-67-10% bipy/Pt*** sample, it seems that the nanoparticles need to be sufficiently large in order to ensure an interface between the Zr-node and the Pt nanoparticle. The particles are all larger than the cavities in the framework, which suggests that there will be an interaction. This all suggests that there is not clear correlation between the particle size and the activity of the catalysts. The uncertainty of the diffusion of $PtCl_4^{-2}$-complex before grafting to the bipyridine sites makes a direct comparison between the three samples difficult. It may be that the platinum complex is dispersed in a smaller area in the UiO-67-l0% bipy/less Pt sample, so that the diffusion of Pt(0) may appear the same. There does not seem to be any correlation between the selectivity and the platinum nanoparticles size. In ***Figure 4.45 A***, the selectivity as a function of platinum nanoparticle size is shown. The **UiO-66-BDC(100% COOH)/Pt** sample is excluded from the plot due to the previous mentioned lack of definable nanoparticles.

The results from the **UiO-67-10% bipy/Pt*** samples with different metal loading further support the results by Gutterød *et al.*. The role of the platinum nanoparticle is to dissociate H_2 and CO_2 and methanol is formed by hydrogen from the platinum particle and carbon dioxide adsorbed on the Zr-node, forming the formate intermediate. Based on these results, the ideal system for this would be to have a high density of small Pt nanoparticles anchored to a ZrO_2 surface with high surface area to maximize the number of low coordinated sites at the intersection between the two components.

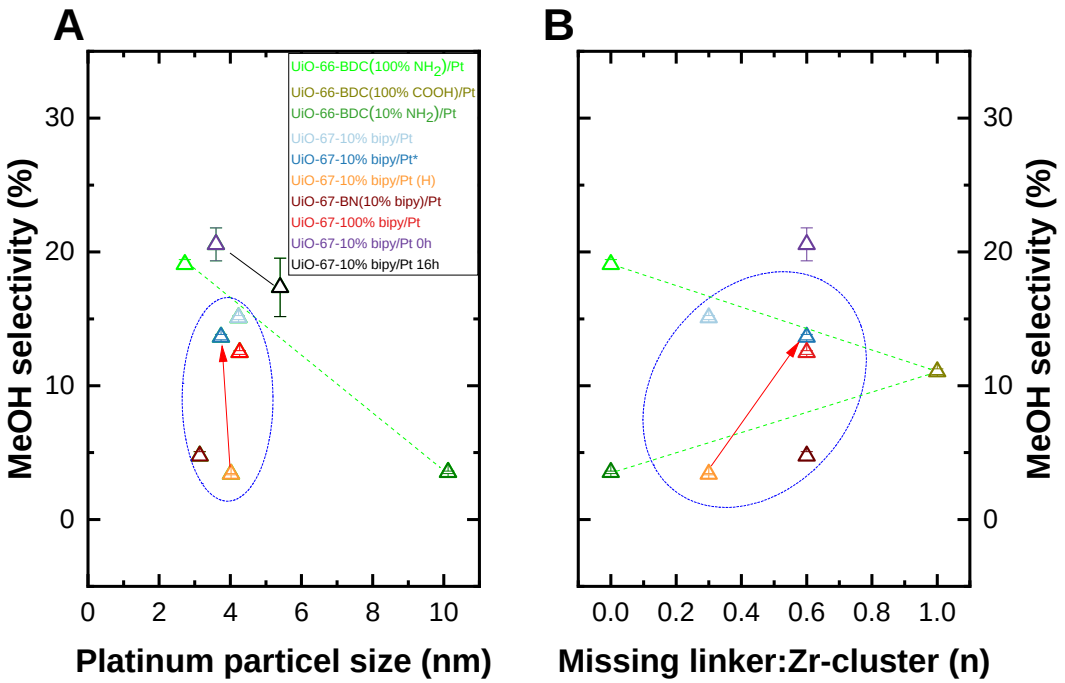

Figure 4.45: *Selectivity as a function of Pt nanoparticle size (**A**) and Selectivity as a function of missing linker:Zr-node ratio (**B**). Both y-axes have a break from 30% to 60%. The lines/circles indicate which samples below to the same group; green = UiO-66, blue = UiO-67 and black = oxidized samples. The red arrows show the difference between the parent and healed **UiO-67-10% bipy/Pt***.*

Gutterød *et al.* suggested an increased selectivity towards methanol with increasing missing linkers.[1] A plot of the selectivity as a function of the estimated missing linker:Zr-node was made to see if there was any correlation. This plot can be seen in ***Figure 4.45 B***. Due to both the rough estimation of the missing linker amount and the difference in material characteristics between the samples, a trend may be hard to see, and the spread of the data-points seem to show a horizontal linear tend. The two samples that can be compared is the **UiO-67-10% bipy/Pt*** and **UiO-67-10% bipy/Pt (H)** as they both originate from the same **UiO-67 10% bipy*** batch and have similar Pt nanoparticle sizes. They show a trend (red arrows) that having less missing linkers gives a lower selectivity towards methanol, supporting the results from Gutterød *et al.*[1] The **UiO-67-10% bipy/Pt 16h** is assumed to have an infinitely large missing linker:Zr-node ratio, and is not included in the plot.

From literature studies, ZrO_2 stands out among the oxides as a good candidate as a support or promoter for CO_2 hydrogenation. This is due to its weak hydrophilic character that benefits the desorption of H_2O, which again increases the methanol selectivity.[61] Over the Cu/ZrO_2-based catalyst, both the copper and zirconia surfaces partake in the formation of methanol. Using IR spectroscopy, Schilke *et al.* found that CO_2 could absorb and form bicarbonate species on the

zirconia surface.[62] This is similar to the formate species forming on the Zr-nodes of the MOF as reported by Gutterød *et al.*.[1] Comprehensive studies of different oxides reveal that in the case of metal on oxide supported catalysts, the catalytic activity depends on the interface between the metal and the oxide.[63, 64] These systems used copper as the metal component of the catalyst. As seen in this thesis the methanol formation for the Pt/UiO-MOF systems is also dependent on these interfaces. It can therefore be argued that the role of the Zr-node is the same as the role of ZrO_2 in a normal metal on support type catalyst. The main difference the MOFs makes is therefore solely structural confinement of the system, increasing the surface area and dispersing the Zr-nodes and the platinum.

When the MOFs are oxidized, the structure of the MOF disappears and leaves Pt nanoparticles dispersed in a ZrO_2-matrix, increasing the amount of interactions between the metal and the support, while increasingly losing surface area with time on stream. MOFs are very expensive to make, and are therefore less attractive as catalysts for industrial use. Zirconia on the other hand is readily available, making it more accessible for industry. The main difference between the ZrO_2- and the MOF-system is the conversion. Although the oxidized sample had higher MeOH selectivity, it comes at a cost for conversion. The **UiO-67-10% bipy/Pt 0h** had more than twice the conversion at 170 °C and 30 bar. It therefore becomes a discussion of priorities , is the selectivity a more important factor than the conversion. Due to the possibility of separating the methanol and water from the effluent, the remaining effluent can be reused. Gutterød *et al.* noted the possibility of carbon monoxide poisoning the reaction by binding to the Pt particles, taking up the sites required to dissociate the hydrogen.[1] If this is the case, then reusing the effluent can become detrimental as the carbon monoxide concentration on the Pt increases for each reuse, decreasing the activity of the catalyst.

5 Conclusion

In this work, the overall target was to investigate Pt nanoparticles formed in various UiO-66 and -67 metal-organic frameworks by Transmission Electron Microscopy, and to study the Pt-containing MOFs as catalysts for the CO_2 hydrogenation reaction. The focus of this thesis was to try to improve the understanding of the platinum nanoparticles and the mechanisms of the reaction.

- When reduced in hydrogen, platinum grows into octahedral crystals that partially destroy the MOF framework around them. Most of the Pt nanoparticles tend to be close to, or on the surface of the MOF crystallites. The platinum shows no growth relationship with the MOF framework.
- The diffusion of the metallic platinum atoms is limited in the system before agglomeration into crystals.
- Increasing the amount of missing linker defects increases the selectivity towards methanol, evidencing that the Zr-node takes part in the formation of methanol. Water inhibits the formation of methanol by competing for the open Zr-O-Zr sites on the Zr-node.
- There is no direct correlation between the type of MOF linkers and the catalyst performance, and there is no direct correlation between the Pt nanoparticle size and catalyst performance.
- The UiO-67 samples continue to exhibit an excellent structural and catalytic stability under test conditions. The UiO-66 systems show the same trend.
- The reverse water-gas shift reaction dominated the system regardless of material, and CO adsorbed on the Pt nanoparticles is the main inhibitor of the reaction.
- Missing linker defects can be introduced in the UiO-67 MOF by subjecting it to a 20% oxygen flow at 350 °C. The organic components of the MOF oxidize into CO and some of the structure of the MOF is lost. After prolonged time in oxygen, XPRD revealed hints of tetragonal ZrO_2.
- When platinum nanoparticles are reduced before the framework is oxidized, the Pt nanoparticle size increases with the duration of the oxidizing conditions, but stays dispersed within the material.
- Fully oxidized samples show higher selectivity towards methanol although having a lower conversion at 30 bars compared to parent UiO-67 MOF impregnated with Pt. At

8 bars, the parent MOF sample shows both higher selectivity towards methanol and higher conversion. This suggests that the Zr-nodes behave similarly to ZrO_2 supports.

6 Future work

The **UiO-67-10% bipy/Pt 16h** catalytic system created by oxidizing the UiO-67 MOF is an expensive way of creating Pt on zirconia catalysts. If Pt/ZrO_2 is the way to go, then less expensive synthesis routes have to be used while not losing the dispersion and size of the Pt nanoparticles.

The amount of defects has proven to be a crucial part for the presence of Zr-O-Zr sites. Defects can be created in many ways. The most common ways are during synthesis by controlling the amount of modulator, or thermally induced post synthetically. To further understand the control of temperature induced defects in MOF more screening of oxidation conditions has to be done. In this work only three different time scales investigated, and the oxidation flow was chosen at random. Future work should investigate the rate of defect generation at different conditions to tune the control of defects.

The way the materials are synthesized has proven to have great impact on the catalytic activity of the materials. The dispersion of grafting sites for the metal salt is crucial to ensure the dispersion of the nanoparticles after reduction. Having better understanding of how to achieve homogeneous dispersion of functional linkers in the MOF matrix is therefore important. This also needs a good way of analyzing the position of these linkers. Previously, H^1NMR of digested MOF and structure refinement with XRD have been used to estimate the amount and location of the functional linkers, but these methods only give an average of the system and not an accurate result. Therefore new techniques are needed to further the understanding of the material, e.i., the catalytic activity and mechanisms.

Some of the materials investigated did not have any site for the platinum to graft on to, but post-synthetic wet impregnation of the metal salt was still preformed. In the future the metal should be introduced into the MOF with the incipient wetness impregnation method to ensure that the metal is satisfactory introduced when no apparent grafting site is present.

In this thesis platinum nanoparticles were investigated in transmission electron microscope. The particles were found to often be located close to or on the surface of the MOFs. To further investigate this, tomography experiments are required. Tomography will be able to more accurately determine the location of the nanoparticles in the system. Recent advances in technology has made electron microscopy of sensitive materials such as MOFs more accessible. These techniques are still too expensive for the general market, but in time may become accessible and make structural investigations of MOFs more readily available.

In the samples investigated here, the presence of water proved to inhibit the formation of methanol by occupying the sites on the Zr-nodes. To further investigate the nature of this phenomenon, a wet H/D-transient experiment could prove useful. Due to the poisoning of the reaction by CO, more transient experiments are needed to get a better mechanistic understanding of the systems.

The work in this thesis have provided insight into the catalytic system for the CO_2-hydrogenation reaction. As shown above, there are still many questions that are left unanswered.

7 Acknowledgments

I would like to acknowledge Dr. Maela Manzoli from the Department of Drug science and Technology at the University of Turin for advice on handlings sensitive materials in TEM, and access to analyzing software. I further acknowledge Koen W. Bossers, Christia Jabbour and Laurens D. B. Mandemaker from the Inorganic Chemistry and Catalysis group at Utrecht University for interesting discussions and TEM characterization, Dr. Evgeniy Redekop from the Department of Chemistry at the University of Oslo for TAP measurements and Dr. Christian Ahoba-Sam for high pressure tests.

8 Supporting information

This section contains supporting information to the thesis.

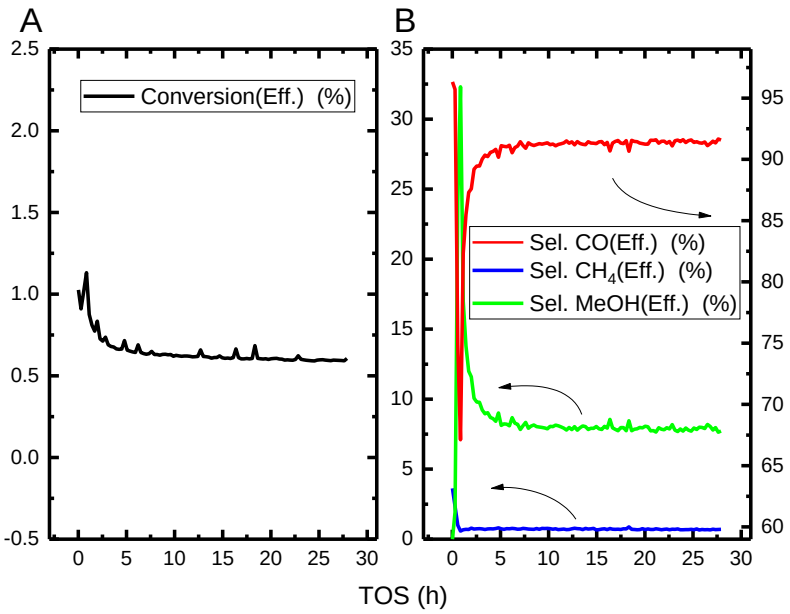

:

S1: *The stability of the UiO-67-10% bipy/Pt (H) catalyst over a 28 hour TOS. Graph* ***A*** *show the conversion and the graph* ***B*** *show the selectivity. Methane and methanol selectivity is on the left axis and carbon monoxide selectivity is on the right axis. Notice the stability of the selectivity as well. The high stability of the methane (blue line) is due to the small amount that is detected by the GC, so fluctuations were harder to detect compared to the CO and the MEOH signals.*

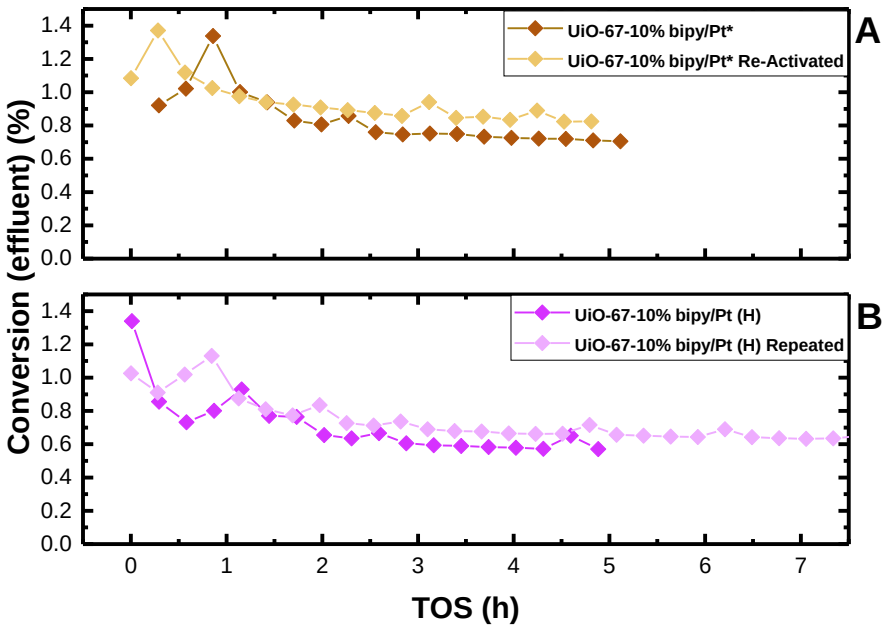

S2: *Graphs showing the reproducibility of the samples. Graph **A** show the sample UiO-67-10% bipy/Pt * run compared the same reactor loading after being reactivated and tested again at 8 bar. Graph **B** show two separate tests of the UiO-67-10% bipy/Pt (H) sample (separate loadings). The uncertainty of catalytic tests can be compared to the difference in values shown in the two graphs.*

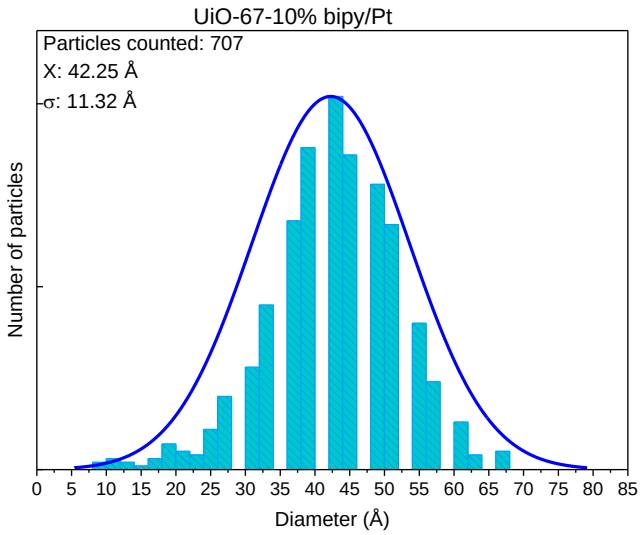

S3: *A histogram showing the nano particle size distribution for the UiO-67-10% bipy/Pt sample. The distribution seem to have a very Gaussian bell-shape, but has distinct holes in the distribution. This could be because of magic number; that nano-particles have distinct number of atoms that it prefers to have, due to the packing and the charge. Both the mean (X) and the standard deviation (σ) is given as Å.*

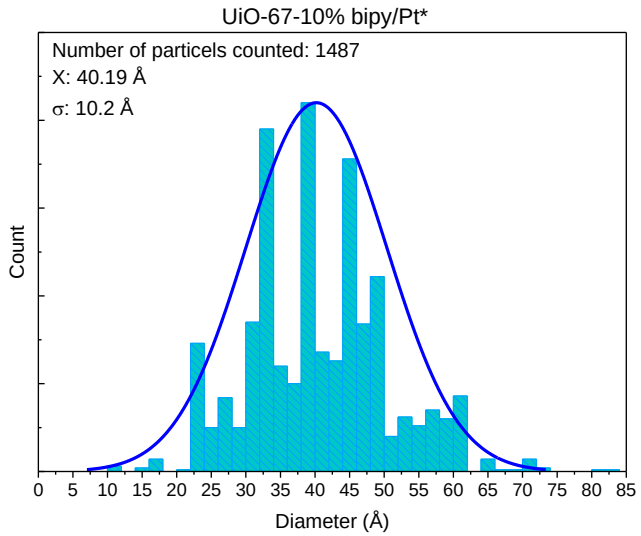

S4: *A histogram showing the nano particle size distribution for the UiO-67-10% bipy/Pt* sample.*

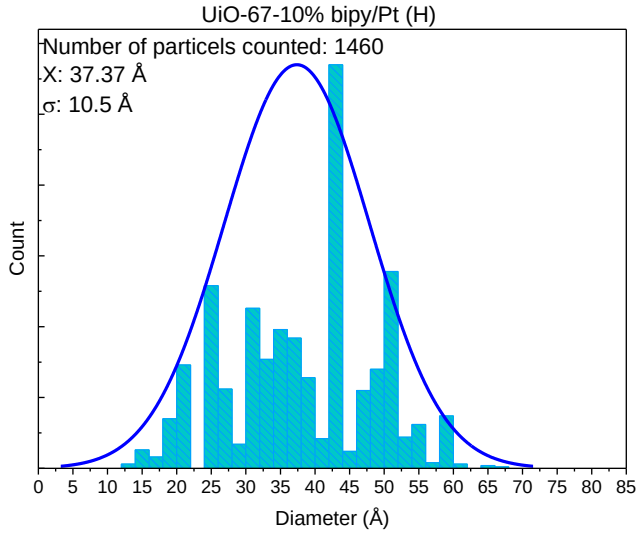

S5: *A histogram showing the nano particle size distribution for the UiO-67-10% bipy/Pt (H) sample.*

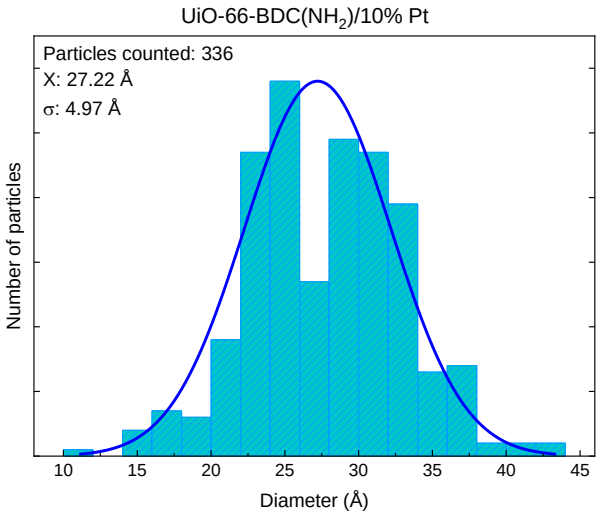

S6: *A histogram showing the nano particle size distribution for the UiO-66-BDC(NH_2)/10% Pt sample. Both the mean (X) and the standard deviation (σ) is given as Å.*

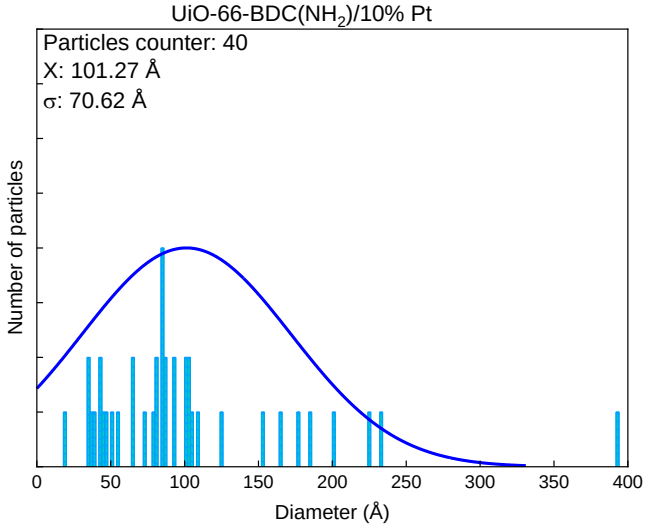

S7: *A histogram showing the nano particle size distribution for the UiO-66-BDC(10% NH_2/Pt) sample. The distribution is bad due to agglomeration of particles and a lack of number of particles. An example of the particles can be seen on* ***S6****. The Both the mean (X) and the standard deviation (σ) is given as Å.*

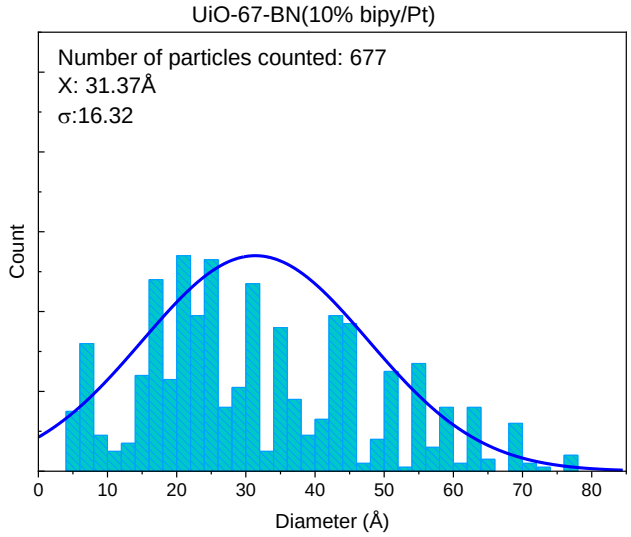

S8: *A histogram showing the nano particle size distribution for the UiO-67-BN(10% bipy/Pt) sample.*

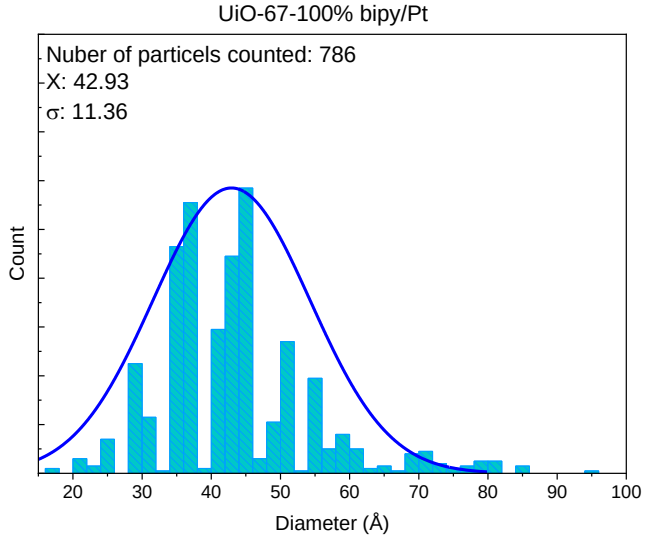

S9: *A histogram showing the nano particle size distribution for the UiO-67-100% bipy/Pt sample.*

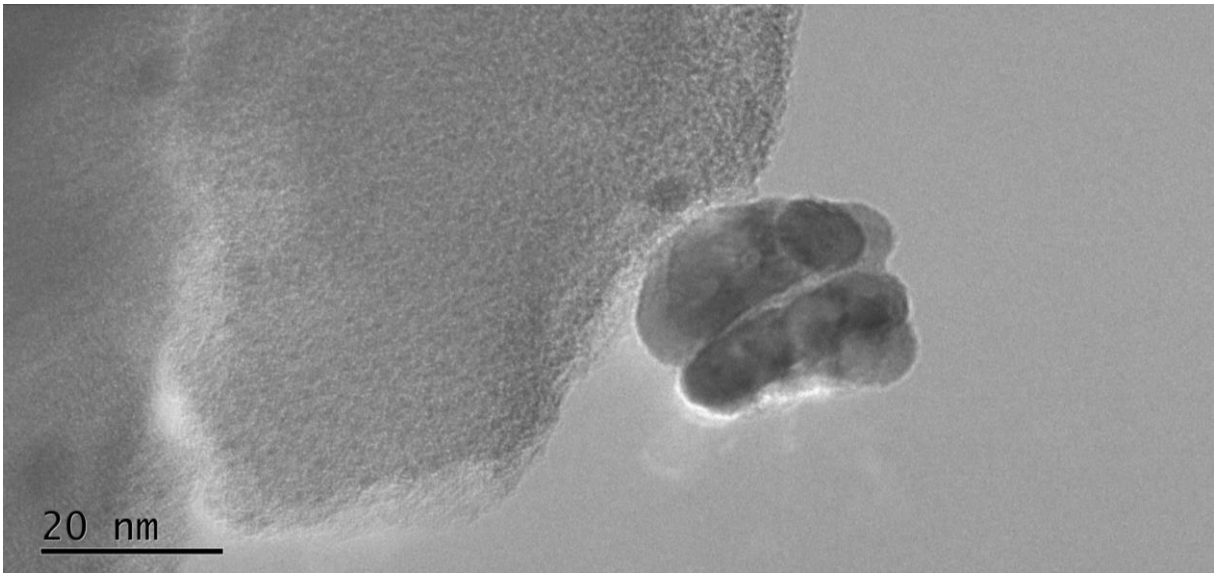

S10: *A TEM picture of the sample UiO-66-BDC(10% NH_2/Pt). As seen on the image, the particle had agglomerated into larger asymmetrical shapes. This proved difficult to analyze.*

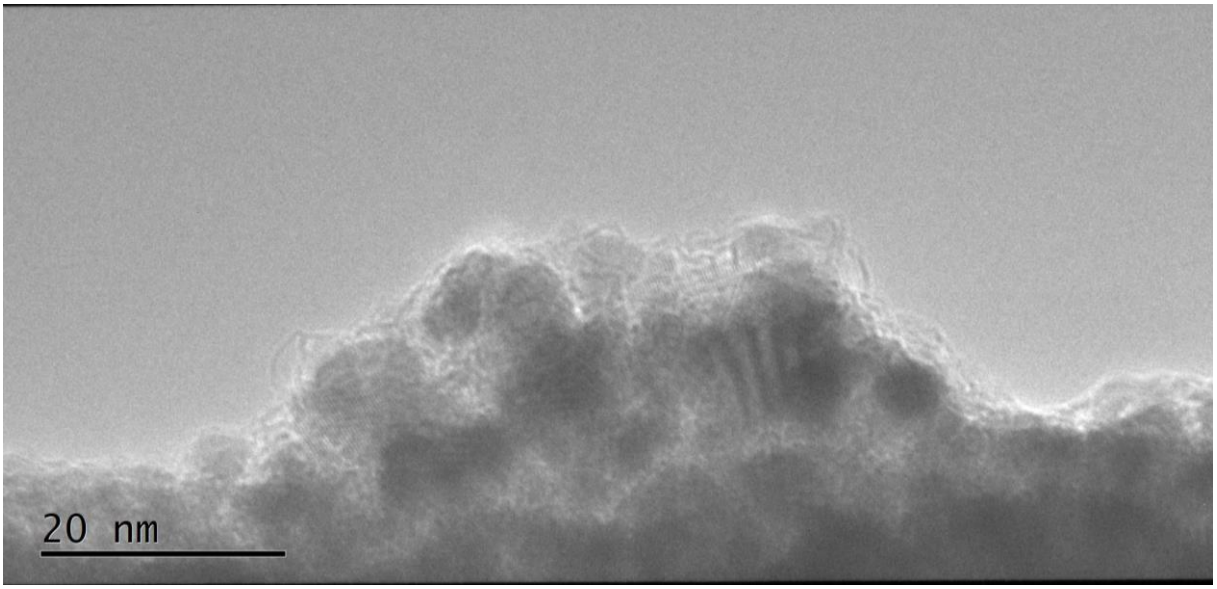

S11: *A TEM picture of the sample UiO-66-BDC(COOH)/Pt. As seen on the image, a coating of Pt nano particles have been formed around the MOF. Any counting and measuring of the particle size was therefore not attempted.*

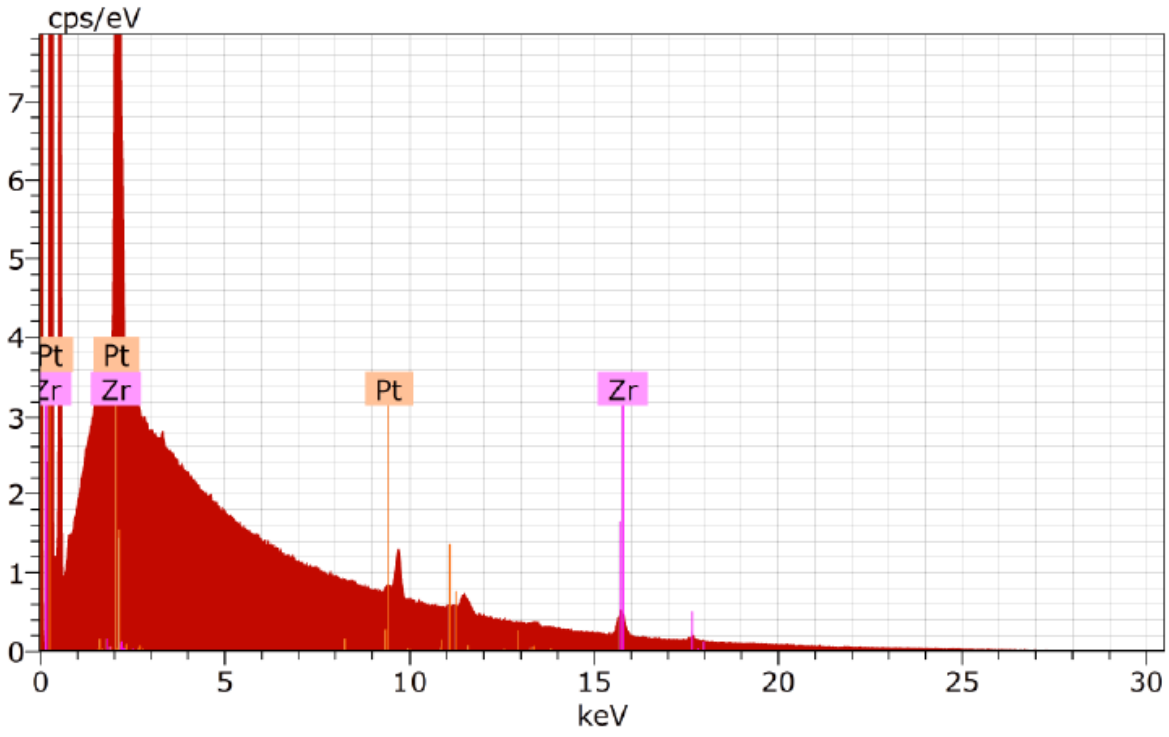

S12: *An energy dispersive X-ray spectra of the UiO-67-10% bipy/Pt (H). As can be seen in the spectra, the lower energy peaks (at >0 and ~2 keV) of Pt and Zr are overlapping, thus the Zr K-series and Pt L-series had to be used to quantify the composition of these elements.*

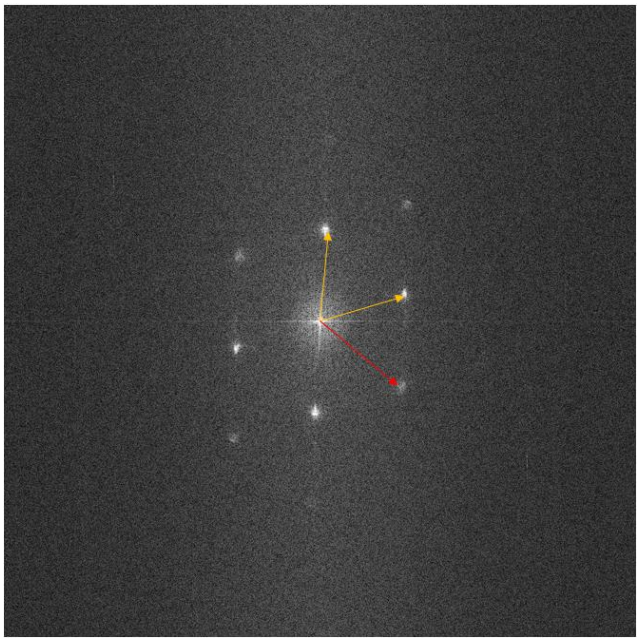

S13: *The Fourier transform of the BF STEM image in* ***Figure 7****. Two of the six reflexes are longer than the others. The yellow arrows show the [111] and [-111] reflexes while the red arrow show the [200] reflex.*

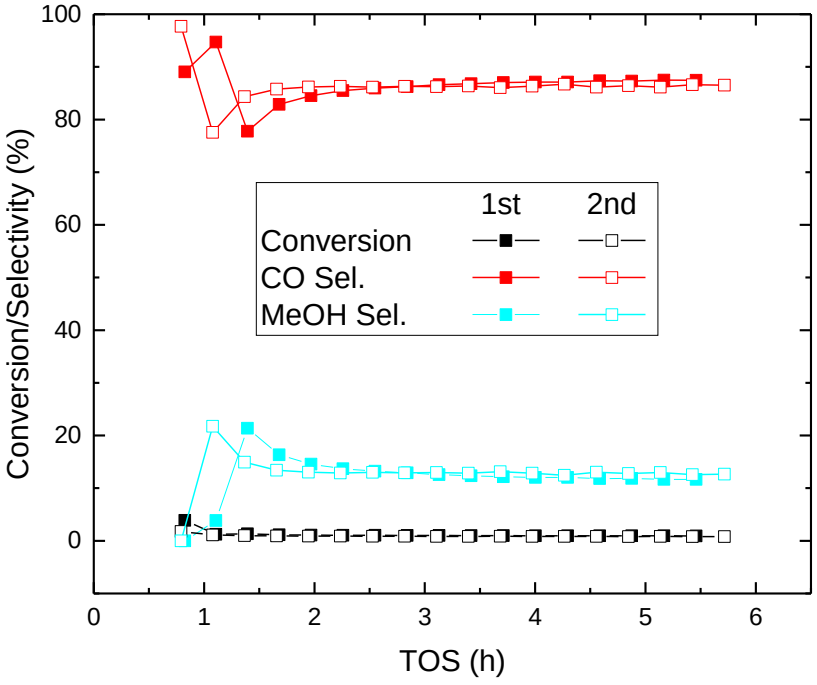

S13: *A plot showing the conversion, CO and MeOH selectivity of the UiO-67-10% bipy/less Pt sample tested two times. The two tests are separated and have used the same catalyst, loaded two separated times. The plot show that the results were real and reproducible.*

9 References

1. Gutterød, E. S.; Lazzarini, A.; Fjermestad, T.; Kaur, G.; Manzoli, M.; Bordiga, S.; Svelle, S.; Lillerud, K. P.; Skúlason, E.; Øien-Ødegaard, S.; Nova, A.; Olsbye, U., Hydrogenation of CO2 to Methanol by Pt Nanoparticles Encapsulated in UiO-67: Deciphering the Role of the Metal–Organic Framework. *Journal of the American Chemical Society* **2020,** *142* (2), 999-1009.
2. Smil, V., Global coal consumption, measured in terawatt-hours. In *Energy Transitions: Global and National Perspectives. & BP Statistical Review of World Energy.*, BP, Ed. 2019.
3. Smil, V., Global solar energy consumption, measured in terawatt-hours. In *Energy Transitions: Global and National Perspectives. & BP Statistical Review of World Energy.*, BP, Ed. 2019.
4. Smil, V., Global oil consumption, measured in terawatt-hours. In *Energy Transitions: Global and National Perspectives. & BP Statistical Review of World Energy.*, BP, Ed. 2019.
5. Smil, V., Global gas consumption, measured in terawatt-hours. In *Energy Transitions: Global and National Perspectives. & BP Statistical Review of World Energy.*, BP, Ed. 2019.
6. Smil, V., Global traditional biofuels consumption, measured in terawatt-hours. In *Energy Transitions: Global and National Perspectives. & BP Statistical Review of World Energy.*, BP, Ed. 2019.
7. Smil, V., Global other renewables consumption, measured in terawatt-hours. In *Energy Transitions: Global and National Perspectives. & BP Statistical Review of World Energy.*, BP, Ed. 2019.
8. Smil, V., Global hydropower consumption, measured in terawatt-hours. In *Energy Transitions: Global and National Perspectives. & BP Statistical Review of World Energy.*, BP, Ed. 2019.
9. Smil, V., Global nuclear consumption, measured in terawatt-hours. In *Energy Transitions: Global and National Perspectives. & BP Statistical Review of World Energy.*, BP, Ed. 2019.
10. Smil, V., Global wind consumption, measured in terawatt-hours. In *Energy Transitions: Global and National Perspectives. & BP Statistical Review of World Energy.*, BP, Ed. 2019.
11. IOGP *Report to the thirty second meeting of the European Gas Regulatory forum 5-6 June 2019*; 2019.
12. Chen, Z.; Dinh, H.; Miller, E., *Photoelectrochemical Water splirring - Standards, Experimental Methods, and Protocols* Springer: New York, 2013.
13. Chase, M. W., Jr., NIST-JANAF Thermochemical Tables Fourth Edition Part1, Al-Co. Technology, N. I. o. S. a., Ed. Gaithersburg, Maryland, United States of America, 1998.
14. Beenackers, A. A. C. M.; Swaaij, W. P. M. V., Methanol from Wood I. Process Principles and Technologies for Producing Methanol from Biomass. *International Journal of Solar Energy* **1984,** *2* (5), 349-367.
15. Molstad, M. C.; Dodge, B. F., Zinc Oxide–Chromium Oxide Catalysts for Methanol Synthesis. *Industrial & Engineering Chemistry* **1935,** *27* (2), 134-140.
16. Lesch, J., *The German Chemical Industry in the Twentieth Century*. Springer: 2000.
17. Lange, J.-P., Methanol synthesis: a short review of technology improvements. *Catalysis Today* **2001,** *64* (1), 3-8.
18. Niemantsverdriet, J. W.; Chorkendorff, I., *Concepts of Modern Catalysis and Kinetics*. 2 ed.; WILEY-VCH Verlag GmbH & Co. KGaA: Germany, 2007.
19. Anderson, J. R.; Boudart, M., *Catalysis - Science and Technology*. Springer: Berlin, 1984; Vol. 5.
20. Jalama, K., Carbon dioxide hydrogenation over nickel-, ruthenium-, and copper-based catalysts: Review of kinetics and mechanism. *Catalysis Reviews* **2017,** *59* (2), 95-164.
21. Ma, J.; Sun, N.; Zhang, X.; Zhao, N.; Xiao, F.; Wei, W.; Sun, Y., A short review of catalysis for CO2 conversion. *Catalysis Today* **2009,** *148* (3), 221-231.
22. Saeidi, S.; Amin, N. A. S.; Rahimpour, M. R., Hydrogenation of CO2 to value-added products—A review and potential future developments. *Journal of CO2 Utilization* **2014,** *5*, 66-81.
23. Román-Martínez, M. C.; Cazorla-Amorós, D.; Salinas-Martínez de Lecea, C.; Linares-Solano, A., Structure Sensitivity of CO2 Hydrogenation Reaction Catalyzed by Pt/Carbon Catalysts. *Langmuir* **1996,** *12* (2), 379-385.

24. Schöder, M., *Functioanal Metal-Organic Frameworks: Gas Storage, Sepration and Catalysis*. 1 ed.; Springer-Verlag Berlin Heidelberg: 2010; p XII, 264.
25. Yuan, S.; Feng, L.; Wang, K.; Pang, J.; Bosch, M.; Lollar, C.; Sun, Y.; Qin, J.; Yang, X.; Zhang, P.; Wang, Q.; Zou, L.; Zhang, Y.; Zhang, L.; Fang, Y.; Li, J.; Zhou, H.-C., Stable Metal–Organic Frameworks: Design, Synthesis, and Applications. *Advanced Materials* **2018,** *30* (37), 1704303.
26. Soni, S.; Bajpai, P.; Arora, C., A review on metal-organic framework: synthesis, properties and application. *Characterization and Application of Nanomaterials* **2018,** *2*.
27. Cavka, J. H.; Jakobsen, S.; Olsbye, U.; Guillou, N.; Lamberti, C.; Bordiga, S.; Lillerud, K. P., A new zirconium inorganic building brick forming metal organic frameworks with exceptional stability. *Journal of the American Chemical Society* **2008,** *130* (42), 13850-13851.
28. Gutov, O. V.; Hevia, M. G.; Escudero-Adan, E. C.; Shafir, A., Metal-Organic Framework (MOF) Defects under Control: Insights into the Missing Linker Sites and Their Implication in the Reactivity of Zirconium-Based Frameworks. *Inorganic Chemistry* **2015,** *54* (17), 8396-8400.
29. Ling, S. L.; Slater, B., Dynamic acidity in defective UiO-66. *Chemical Science* **2016,** *7* (7), 4706-4712.
30. Shearer, G. C.; Chavan, S.; Bordiga, S.; Svelle, S.; Olsbye, U.; Lillerud, K. P., Defect Engineering: Tuning the Porosity and Composition of the Metal-Organic Framework UiO-66 via Modulated Synthesis. *Chemistry of Materials* **2016,** *28* (11), 3749-3761.
31. Taddei, M., When defects turn into virtues: The curious case of zirconium-based metal-organic frameworks. *Coordination Chemistry Reviews* **2017,** *343*, 1-24.
32. Kaur, G.; Øien-Ødegaard, S.; Lazzarini, A.; Chavan, S. M.; Bordiga, S.; Lillerud, K. P.; Olsbye, U., Controlling the Synthesis of Metal–Organic Framework UiO-67 by Tuning Its Kinetic Driving Force. *Crystal Growth & Design* **2019,** *19* (8), 4246-4251.
33. Braglia, L.; Borfecchia, E.; Martini, A.; Bugaev, A. L.; Soldatov, A. V.; Øien-Ødegaard, S.; Lonstad-Bleken, B. T.; Olsbye, U.; Lillerud, K. P.; Lomachenko, K. A.; Agostini, G.; Manzoli, M.; Lamberti, C., The duality of UiO-67-Pt MOFs: connecting treatment conditions and encapsulated Pt species by operando XAS. *Physical Chemistry Chemical Physics* **2017,** *19* (40), 27489-27507.
34. Gutterød, E. S.; Øien-Ødegaard, S.; Bossers, K.; Nieuwelink, A. E.; Manzoli, M.; Braglia, L.; Lazzarini, A.; Borfecchia, E.; Ahmadigoltapeh, S.; Bouchevreau, B.; Lonstad-Bleken, B. T.; Henry, R.; Lamberti, C.; Bordiga, S.; Weckhuysen, B. M.; Lillerud, K. P.; Olsbye, U., CO2 Hydrogenation over Pt-Containing UiO-67 Zr-MOFs-The Base Case. *Industrial & Engineering Chemistry Research* **2017,** *56* (45), 13207-13219.
35. Liu, L.; Chen, Z.; Wang, J.; Zhang, D.; Zhu, Y.; Ling, S.; Huang, K.-W.; Belmabkhout, Y.; Adil, K.; Zhang, Y.; Slater, B.; Eddaoudi, M.; Han, Y., Imaging defects and their evolution in a metal–organic framework at sub-unit-cell resolution. *Nature Chemistry* **2019,** *11* (7), 622-628.
36. Fultz, B.; Howe, J., *Transmission Electrom Microscopy and Diffraction of Materials*. 4 ed.; Springer Heidelberg: New York, Dordrecht, London, 2013.
37. Ledesma, C.; Yang, J.; Chen, D.; Holmen, A., Recent Approaches in Mechanistic and Kinetic Studies of Catalytic Reactions Using SSITKA Technique. *ACS Catalysis* **2014,** *4* (12), 4527-4547.
38. Solemsli, B. G. Investigtion on the effect of different activation conditions on the catalytic activity of Pt-functionalized UiO-67 10% bpy. University of Oslo, 2018.
39. Robiche, N. *Comptage de partivuele version 2.0*, 2.0; University P. and M. Curie.
40. Formenti, D.; Ferretti, F.; Topf, C.; Surkus, A.-E.; Pohl, M.-M.; Radnik, J.; Schneider, M.; Junge, K.; Beller, M.; Ragaini, F., Co-based heterogeneous catalysts from well-defined α-diimine complexes: Discussing the role of nitrogen. *Journal of Catalysis* **2017,** *351*, 79-89.
41. Vilé, G.; Albani, D.; Nachtegaal, M.; Chen, Z.; Dontsova, D.; Antonietti, M.; López, N.; Pérez-Ramírez, J., A Stable Single-Site Palladium Catalyst for Hydrogenations. *Angewandte Chemie International Edition* **2015,** *54* (38), 11265-11269.
42. Gutterød, E. S. On the Hydrogenation of CO2 over Pt Functionalized UiO-67 Metal-Organic Frameworks. Univeristy of Olso, Oslo, 2020.
43. Persson, K., Materials Data on ZrO2 (SG:137) by Materials Project",

abstractNote = "Computed materials data using density functional theory calculations. These calculations determine the electronic structure of bulk materials by solving approximations to the Schrodinger equation. For more information, see https://materialsproject.org/docs/calculations. United States, 2014.
44. Persson, K., Materials Data on ZrO2 (SG:225) by Materials Project",

abstractNote = "Computed materials data using density functional theory calculations. These calculations determine the electronic structure of bulk materials by solving approximations to the Schrodinger equation. For more information, see https://materialsproject.org/docs/calculations. United States, 2014.
45. Shearer, G. C.; Forselv, S.; Chavan, S.; Bordiga, S.; Mathisen, K.; Bjorgen, M.; Svelle, S.; Lillerud, K. P., In Situ Infrared Spectroscopic and Gravimetric Characterisation of the Solvent Removal and Dehydroxylation of the Metal Organic Frameworks UiO-66 and UiO-67. *Topics in Catalysis* **2013,** *56* (9-10), 770-782.
46. Øien-Ødegaard, S.; Bouchevreau, B.; Hylland, K.; Wu, L.; Blom, R.; Grande, C.; Olsbye, U.; Tilset, M.; Lillerud, K. P., UiO-67-type Metal–Organic Frameworks with Enhanced Water Stability and Methane Adsorption Capacity. *Inorganic Chemistry* **2016,** *55* (5), 1986-1991.
47. Li, L.; Abild-Pedersen, F.; Greeley, J.; Nørskov, J. K., Surface Tension Effects on the Reactivity of Metal Nanoparticles. *The Journal of Physical Chemistry Letters* **2015,** *6* (19), 3797-3801.
48. Ahmad, K.; Upadhyayula, S., Greenhouse gas CO2 hydrogenation to fuels: A thermodynamic analysis. *Environmental Progress & Sustainable Energy* **2019,** *38* (1), 98-111.
49. Tran, R.; Xu, Z.; Radhakrishnan, B.; Winston, D.; Sun, W.; Persson, K. A.; Ong, S. P., Surface energies of elemental crystals. *Scientific Data* **2016,** *3* (1), 160080.
50. Tran, R.; Li, X.-G.; Montoya, J. H.; Winston, D.; Persson, K. A.; Ong, S. P., Anisotropic work function of elemental crystals. *Surface Science* **2019,** *687*, 48-55.
51. Zheng, H.; Li, X.-G.; Tran, R.; Chen, C.; Horton, M.; Persson, K. A.; Ong, S. P., Grain Boundary Properties of Elemental Metals. arXiv.org: 2019.
52. Chatzigoulas, A.; Karathanou, K.; Dellis, D.; Cournia, Z., NanoCrystal: A Web-Based Crystallographic Tool for the Construction of Nanoparticles Based on Their Crystal Habit. *Journal of Chemical Information and Modeling* **2018,** *58* (12), 2380-2386.
53. Jain, A.; Ong, S. P.; Hautier, G.; Chen, W.; Richards, W. D.; Dacek, S.; Cholia, S.; Gunter, D.; Skinner, D.; Ceder, G.; Persson, K. A., Commentary: The Materials Project: A materials genome approach to accelerating materials innovation. *APL Materials* **2013,** *1* (1), 011002.
54. Persson, K., Materials Data on Pt (SG:225) by Materials Project. United States, 2015.
55. Moliner, M.; Gabay, J. E.; Kliewer, C. E.; Carr, R. T.; Guzman, J.; Casty, G. L.; Serna, P.; Corma, A., Reversible Transformation of Pt Nanoparticles into Single Atoms inside High-Silica Chabazite Zeolite. *Journal of the American Chemical Society* **2016,** *138* (48), 15743-15750.
56. Braglia, L.; Borfecchia, E.; Lomachenko, K. A.; Bugaev, A. L.; Guda, A. A.; Soldatov, A. V.; Bleken, B. T. L.; Oien-Odegaard, S.; Olsbye, U.; Lillerud, K. P.; Bordiga, S.; Agostini, G.; Manzoli, M.; Lamberti, C., Tuning Pt and Cu sites population inside functionalized UiO-67 MOF by controlling activation conditions. *Faraday Discussions* **2017,** *201*, 265-286.
57. Mayrhofer, K.; Arenz, M.; Blizanac, B.; Stamenkovic, V.; Ross, P.; Marković, N., CO surface electrochemistry on Pt-nanoparticles: A selective review. *Electrochimica Acta* **2005,** *50*, 5144-5154.
58. Mayrhofer, K. J. J.; Blizanac, B. B.; Arenz, M.; Stamenkovic, V. R.; Ross, P. N.; Markovic, N. M., The Impact of Geometric and Surface Electronic Properties of Pt-Catalysts on the Particle Size Effect in Electrocatalysis. *The Journal of Physical Chemistry B* **2005,** *109* (30), 14433-14440.
59. Maillard, F.; Eikerling, M.; Cherstiouk, O. V.; Schreier, S.; Savinova, E.; Stimming, U., Size effects on reactivity of Pt nanoparticles in CO monolayer oxidation: The role of surface mobility. *Faraday Discussions* **2004,** *125* (0), 357-377.
60. Paulus, P. M.; Goossens, A.; Thiel, R. C.; van der Kraan, A. M.; Schmid, G.; de Jongh, L. J., Surface and quantum-size effects in Pt and Au nanoparticles probed by (167)Au Mössbauer spectroscopy. *Physical Review B* **2001,** *64* (20), 205418.

61. Wambach, J.; Baiker, A.; Wokaun, A., CO2 hydrogenation over metal/zirconia catalysts. *Physical Chemistry Chemical Physics* **1999,** *1* (22), 5071-5080.
62. Schilke, T. C.; Finsher, I. A.; Bell, A. T., In Situ Infrared Study of Methanol Synthesis from CO2/H2 on Titania and Zirconia Promoted Cu/SiO2. *Journal of Catalysis* **1999,** *184*.
63. Arena, F.; Mezzatesta, G.; Zafarana, G.; Trunfio, G.; Frusteri, F.; Spadaro, L., How oxide carriers control the catalytic functionality of the Cu–ZnO system in the hydrogenation of CO2 to methanol. *Catalysis Today* **2013,** *210*, 39–46.
64. Arena, F.; Mezzatesta, G.; Zafarana, G.; Trunfio, G.; Frusteri, F.; Spadaro, L., Effects of oxide carriers on surface functionality and process performance of the Cu–ZnO system in the synthesis of methanol via CO2 hydrogenation. *Journal of Catalysis* **2013,** *300*, 141–151.